Exchange Interactions and Induced Eu^{3+} Magnetic Order in $R\mathrm{MnO_3}$ Investigated Using Resonant X-ray Diffraction

Dissertation with the aim of achieving a doctoral degree at the
Faculty of Mathematics, Informatics and Natural Sciences
Department of Physics
of Universität Hamburg

submitted by Arvid Skaugen

2014 in Hamburg

Gutachter der Dissertation:	Prof. Dr. Ralf Röhlsberger Prof. Dr. Michael Rübhausen
Gutachter der Disputation:	Prof. Dr. Ralf Röhlsberger Prof. Dr. Markus Drescher
Datum der Disputation:	26.02.2015
Vorsitzender des Prüfungsausschusses:	Dr. Georg Steinbrück
Vorsitzender des Fachpromotionsausschusses:	Prof. Dr. Jan Louis
Dekan der Fachbereichs Physik:	Prof. Dr. Heinrich Graener

Abstract

The so-called multiferroics, materials that concomitantly exhibit more than one ferroic order, have in recent years attracted much attention owing to their possible applications in high density data storage, high sensitivity ac magnetic field sensors and novel spintronic devices. In particular, multiferroics with strong magnetoelectric coupling are more attractive. Among such multiferroics, an interesting special class is the orthorhombic manganites with perovskite structure. In these compounds, frustration serves to destabilize ordinary ferromagnetic or antiferromagnetic ordering, giving rise to rich phase diagrams due to several competing magnetic interactions. Interactions between strong rare earth magnetic moments and weaker transition metal moments add another level of complexity, as well as interest.

The current dissertation presents results obtained investigating the magnetic structure responsible for ferroelectricity in a few selected multiferroic compounds, using x-ray resonant magnetic scattering (XRMS). In particular, single crystals of $Eu_{1-x}Y_xMnO_3$ have been studied at low temperatures and in high magnetic fields. This series of compounds is similar in structure to the heavily studied RMnO$_3$ (R=Tb,Gd,Dy), only without rare earth magnetism. The novel technique of full polarization analysis has been used to determine the complicated cycloidal Mn magnetic ordering, and additional components due to the Dzyaloshinskii-Moriya interactions have been identified. In the compound $Eu_{0.8}Y_{0.2}MnO_3$, two coexisting multiferroic phases were observed, and a magnetoelectric coupling between the two was established. Moreover, magnetic order of the formally non-magnetic rare earth ion Eu^{3+} was observed in the same compound. It has been concluded to result from a Van Vleck type excitation of the $J = 0$ ground state due to the symmetry-breaking internal exchange field from the Mn magnetic moments.

In addition, this dissertation reports on high field investigations of the complex low-temperature phases of $GdMnO_3$ as well as high energy non-resonant scattering studies of $TbMnO_3$. In the case of $TbMnO_3$, the simple high energy magnetic cross section allowed for direct determination of spin components in the ferroelectric phase. In the case of $GdMnO_3$, the first high field XRMS investigation below the Gd ordering temperature was performed, revealing an important role of the symmetric exchange interaction between the Gd and Mn subsystems for stabilizing ferroelectricity in the compound.

Kurzdarstellung

In den letzten Jahren haben multiferroische Systeme, d. h. Materialien, in denen mindestens zwei ferroische Ordnungsphnomene zugleich auftreten, aufgrund ihrer Anwendungsmöglichkeiten in der Datenspeicherung, in hochsensiblen elektromagnetischen Feldsensoren und in neuartigen spintronischen Geräten viel Aufmerksamkeit auf sich gezogen. Insbesondere Multiferroika mit starken magnetoelektrischen Eigenschaften sind in dieser Hinsicht besonders Attraktiv. Innerhalb der Multiferroika stellen die orthorhombischen Manganiten mit Perowskit-Struktur eine besondere Untergruppierung dar. Bei diesen Verbindungen wird die üblichen ferromagnetischen oder antiferromagnetischen Ordnungen durch Frustration destablisiert, so dass durch konkurrierender magnetischer Interaktionen interessante Phasendiagramme entstehen. Die Wechselwirkungen zwischen den starken magnetischen Momenten der Seltenen Erden und den schwächeren der Übergangsmetallen erhöhen dabei sowohl die Komplexität als das wissenschaftliche Interesse.

Die vorliegende Arbeit stellt Ergebnisse von Untersuchungen der magnetischen Struktur, die für die Ferroelektrizität in einigen ausgewählten multiferroischen Verbindungen verantwortlich ist, mit resonanter magnetischer Röntgenstreuung vor. Im Einzelnen wurden $Eu_{1-x}Y_xMnO_3$ Einkristalle bei niedrigen Temperaturen in hohen Magnetfeldern erforscht. Diese Verbindungen sind strukturell den bereits eingehend erforschten RMnO$_3$ (R=Tb,Gd,Dy) ähnlich, jedoch ohne Seltenerdmagnetismus. Die neue Methode der vollständigen Polarisationsanalyse wurde eingesetzt, um die komplexe cycloide Mn-magnetischen Ordnungen zu bestimmen, was die Identifizierung weitere Komponenten, basierend auf den Dzyaloshinskii-Moriya-Wechselwirkungen, ermöglichte. In der Verbindung $Eu_{0.8}Y_{0.2}MnO_3$ konnten zwei koexistierende multiferroische Phasen und eine magnetoelektrische Kopplung zwischen den beiden beobachtet werden. Überdies konnte in der selben Verbindung eine magnetische Ordnung unter den zuvor nicht-magnetischen Seltenerdionen Eu^{3+} ermittelt werden. Diese wurde auf eine Van-Vleck-Erregung des J=0 Grundzustand in Folge des symmetrie-brechenden inneren Wechselfelds der Mn-magnetischen Momente zurück geführt.

Des Weiteren gibt diese Doktorarbeit die Ergebnisse von Untersuchungen der komplexen Niedrigtemperaturphasen von GdMnO$_3$ sowie von hochenergetischen, nicht-resonanten Streuungsstudien von TbMnO$_3$ wieder. Im Falle des TbMnO$_3$ erlaubte der einfache hochenergetische magnetische Querschnitt eine unmittelbare Bestimmung der Spinkomponenten in der ferroelektrischen Phase. Im Falle des GdMnO$_3$ wurde die erste XRMS Studie in hohen magnet-

feldern unterhalb der Gd-Ordungstemperatur durchgeführt, welche die hohe Bedeutung der symmetrischen Austauschwechselwirkung zwischen den Gd- und Mn-Untersystemen für die Stabilisierung der ferroelektrischen Eigenschaften der Verbindung verdeutlichte.

Contents

1 Introduction **1**

I Theory and Experimental Techniques **3**

2 Multiferroics **5**
2.1 Incompatibility between ferroelectricity and magnetism 6
2.2 Spiral spin order 7
2.2.1 Microscopic Mechanism 9
2.3 The $R\mathrm{MnO_3}$ system 13
2.3.1 Dzyaloshinskii-Moriya canting in $R\mathrm{MnO_3}$ 16
2.3.2 $R\mathrm{MnO_3}$ in electromagnetic fields 17
2.3.3 The effect of rare earth magnetism 18

3 Experimental Techniques **21**
3.1 Synchrotron Radiation 22
3.1.1 Polarized x-rays 24
3.2 Resonant Scattering 26
3.2.1 Non-resonant x-ray magnetic scattering 32
3.2.2 The Structure Factor 34
3.2.3 Magnetically induced charge scattering 35
3.3 Beamline P09 37
3.3.1 Storage ring and undulator 38
3.3.2 Beamline optics 39
3.3.3 First experimental hutch (EH1) 43
3.3.4 Second experimental hutch (EH2) 46
3.4 Beamline UE46-PGM1 48

II Experimental results **51**

4 Dzyaloshinskii-Moriya canting in $TbMnO_3$ **53**
4.1 Scientific Case . . . 53
4.2 Experiment . . . 54
4.3 Discussion . . . 57

5 *R*-Mn exchange interactions in $GdMnO_3$ **59**
5.1 Scientific Case . . . 59
5.2 Experiment . . . 60
5.3 Discussion . . . 62

6 Magnetic phases in $Eu_{1-x}Y_xMnO_3$ **63**
6.1 Scientific Case . . . 63
6.2 Zero field studies . . . 65
6.2.1 Full Polarization Analysis . . . 69
6.2.2 Soft x-ray studies . . . 72
6.3 High field studies . . . 76
6.4 Discussion . . . 81

7 Eu^{3+} magnetic order in $Eu_{1-x}Y_xMnO_3$ **85**
7.1 Scientific case . . . 85
7.2 Experiment . . . 86
7.3 Discussion . . . 94

8 Summary and outlook **97**

A Calculation of Stokes Parameters **99**

B REXS lineshape calculation **105**

List of Figures

2.1 Multiferroics and magnetoelectrics 6
2.2 Dzyaloshinskii-Moriya interaction 12
2.3 $R\mathrm{MnO_3}$ 14

3.1 Bragg's law 21
3.2 Discovery of X-rays 22
3.3 Brilliance of x-ray sources 23
3.4 Polarization ellipse 25
3.5 Resonant scattering process 27
3.6 P09 beamline 38
3.7 Phase retarder setup 40
3.8 Phase retarder deviation angles 41
3.9 Experimental Hutch 1 43
3.10 Detector arm 45
3.11 Scattering geometry 46
3.12 14 T magnet in Experimental Hutch 2 47
3.13 Helium vapor pressure 48
3.14 Beamline UE46-PGM1 49

4.1 A type order in $\mathrm{TbMnO_3}$ 54
4.2 A type temperature dependence 55
4.3 C type order in $\mathrm{TbMnO_3}$ 55
4.4 G type order in $\mathrm{TbMnO_3}$ 56
4.5 Tb magnetic order in $\mathrm{TbMnO_3}$ 56

5.1 Temperature dependence of Gd order in $\mathrm{GdMnO_3}$ 61
5.2 $\mathrm{GdMnO_3}$ phase diagram 62

6.1 $\mathrm{Eu_{0.8}Y_{0.2}MnO_3}$: History dependent magnetization and polarization 64
6.2 A, F, C and G type Mn magnetic order in $\mathrm{Eu_{0.8}Y_{0.2}MnO_3}$ . . 65
6.3 Mn K edge REXS spectra from $\mathrm{Eu_{0.8}Y_{0.2}MnO_3}$ 66

6.4 $Eu_{0.7}Y_{0.3}MnO_3$: Temperature dependence of A type order . . . 67
6.5 $Eu_{0.8}Y_{0.2}MnO_3$: Temperature dependence of A type order . . . 67
6.6 $Eu_{0.8}Y_{0.2}MnO_3$: Temperature dependence of F and C type order 68
6.7 Magnetically induced charge scattering in $Eu_{0.8}Y_{0.2}MnO_3$ . . . 69
6.8 Analyzer rocking curves for full polarization analysis 70
6.9 Full polarization analysis 72
6.10 Ewald sphere at the Mn L_2 edge 73
6.11 Mn $L_{2,3}$ REXS spectrum from $Eu_{0.7}Y_{0.3}MnO_3$ 74
6.12 $Eu_{0.7}Y_{0.3}MnO_3$: Soft x-ray temperature dependence of F type order 74
6.13 $Eu_{0.8}Y_{0.2}MnO_3$: Soft x-ray temperature dependence of F type order 75
6.14 $Eu_{0.8}Y_{0.2}MnO_3$: F type order behavior under applied magnetic field 76
6.15 Magnetic field dependence of G type order in $Eu_{0.8}Y_{0.2}MnO_3$. 77
6.16 $Eu_{0.8}Y_{0.2}MnO_3$: Temperature dependence under field of F type order 78
6.17 $Eu_{0.7}Y_{0.3}MnO_3$: Temperature dependence under field of F type order 79
6.18 $Eu_{0.7}Y_{0.3}MnO_3$: F type order behavior under applied magnetic field 80
6.19 $Eu_{0.7}Y_{0.3}MnO_3$: A type order behavior under applied magnetic field 81
6.20 Temperature dependence under field of magnetically induced charge scattering in $Eu_{0.8}Y_{0.2}MnO_3$ 83
6.21 H-T phase diagrams of $Eu_{1-x}Y_xMnO_3$ 84

7.1 Eu $M_{4,5}$ REXS and TEY spectra from $Eu_{0.8}Y_{0.2}MnO_3$ 88
7.2 C type Eu^{3+} magnetic order in $Eu_{0.8}Y_{0.2}MnO_3$measured at Eu M_5 resonance 91
7.3 Eu $L_{2,3}$ REXS spectrum from $Eu_{0.8}Y_{0.2}MnO_3$ 92
7.4 F type Eu^{3+} magnetic order in $Eu_{0.8}Y_{0.2}MnO_3$measured at Eu L_3 resonance 93
7.5 G type Eu^{3+} order in the FE phase of $Eu_{0.8}Y_{0.2}MnO_3$ 95
7.6 Ewald sphere at the Eu M_5 edge 96

List of Tables

2.1 DM canting in $R\mathrm{MnO_3}$ 17

3.1 Resonant enhancement 30

7.1 Relative energies of J levels in Eu $f^6\ {}^7F_J$ 89
7.2 Population distribution of different J levels in Eu $f^6\ {}^7F_J$ . . . 89

Chapter 1

Introduction

In just a few decades, computers have moved from being specialist devices used for heavy calculations in science, finance and cryptography, to becoming everyday objects permeating our modern society and used for entertainment, communication, graphics and much more in addition to their original uses. This rapid development has driven, and been driven by, an exponential increase in performance of processing power and data storage, as well as miniaturization of the different components. The drive towards even smaller, faster and more energy-efficient storage media has fueled a search for novel materials with exotic properties. Among these are the multiferroics, in particular the magnetoelectrics, which allow magnetization to be controlled by an electric field or electric polarization to be controlled by a magnetic field. Such materials could offer large improvements on current magnetic storage media with regards to speed and energy efficiency. Other potential applications include magnetic field sensors using multiferroics, components for spintronics, and materials with a negative index of refraction [1]. The presence of magnetization and electric polarization in the same sample could even allow for a new type of 4-state logic device, where the logic state is determined by both up and down polarization and up and down magnetization [2].

Apart from practical applications, the study of magnetoelectrics is interesting also from a fundamental science point of view. Many magnetoelectrics present complex magnetic structures that require new insight into magnetism to explain. The interplay between spin and orbital magnetic moments, electric polarization and crystal structure in a single material is intricate and depends on many factors. Novel effects are still being discovered in this type of compounds, such as hidden order [3], Bose-Einstein condensation of magnons [4, 5], control of spin domain helicity using the photoelectric effect [6], and toroidal moments [2].

For studying strongly correlated electron systems like multiferroics, Reso-

nant X-ray Magnetic Scattering (RXMS) has emerged as an important probe complementary to neutron scattering and bulk measurements. RXMS makes use of both the electric and magnetic properties of electromagnetic radiation to investigate the magnetic ordering in single crystals. The scattering cross-sections are both energy and polarization dependent. By tuning the photon energy close to an absorption edge, it is possible to promote core level electrons into higher level unoccupied orbitals, drastically enhancing the magnetic scattering cross section. This also allows for element specific investigation of magnetic sublattices. Charge and magnetic scattering happen in different polarization channels, which facilitates separation of the magnetic signals from the ordinary Thomson scattering.

The current thesis is laid out as follows: Part I deals with theory and experimental details. In chapter 2 we present an introduction to the field of multiferroics, and take a look at how the magnetoelectric effect can be realized through cycloidal magnetic order. Section 2.3 describes the multiferroic perovskites with chemical formula $R\mathrm{MnO_3}$(R being a rare earth ion), to which all the compounds studied in this thesis belong. Chapter 3 lays out the experimental techniques used, in particular the resonant x-ray scattering process, which is the main experimental method being employed in this thesis. The two synchrotron beamlines where most of the experiments were performed are presented in sections 3.3 and 3.4.

Part II of the thesis presents the experimental results. In chapter 4 we investigate details of the magnetic structure in the well known multiferroic $\mathrm{TbMnO_3}$ using high energy non-resonant x-ray magnetic scattering, allowing for precise moment direction determination and the discovery of additional components to the Mn magnetic structure. In chapter 5, the origin of ferroelectricity in $\mathrm{GdMnO_3}$ is found to be partly due to a symmetric exchange interaction between the Gd and Mn subsystems. Chapter 6 presents magnetic scattering studies in zero and high magnetic fields of two compounds of $\mathrm{Eu_{1-x}Y_xMnO_3}$ with different doping levels. As in $\mathrm{TbMnO_3}$, additional components to the magnetic structure due to the Dzyaloshinskii-Moriya interaction are identified. In the compound $\mathrm{Eu_{0.8}Y_{0.2}MnO_3}$, two coexisting multiferroic phases are observed, and a magnetoelectric coupling between the two is established. In chapter 7, magnetic order of the formally non-magnetic rare earth ion $\mathrm{Eu^{3+}}$ is observed in the same compound. It is concluded to result from a Van Vleck type excitation of the $J = 0$ ground state due to the symmetry-breaking internal exchange field from the Mn magnetic moments.

Finally, in chapter 8, we summarize the results and look forward to new possible experiments.

Part I

Theory and Experimental Techniques

Chapter 2

Multiferroics

Our modern world is filled with electronic devices. Common to many of them is that they utilize either the ferromagnetic or the ferroelectric properties of materials to perform their functions. For instance, magnetic storage media rely on ferromagnetic hysteresis and giant magnetoresistance to write, store and read data. Also, many sensors and actuators make use of ferroelectric materials, as these often are ferroelastics or piezoelectrics, allowing them to convert electric energy into elastic energy and vice versa [7]. The drive towards higher performance and high-density storage makes attractive the idea of integrating several of these ferroic orders into one material. These materials are named *multiferroics*. In the current thesis, the term is restricted to mean the coexistence of ferroelectricity and magnetism. Two hurdles immediately raise themselves. Firstly, it seems very difficult for ferroelectricity and magnetism to coexist in a single material and temperature range, not least because of symmetry arguments, which we will come back to later. Secondly, for applications not only the coexistence, but also an efficient cross-coupling between the two ferroic orders (hereafter referred to as the magnetoelectric (ME) coupling) is very important (see figure 2.1). We know from Maxwell's equations that magnetism and electricity are intrinsically coupled, but the realization of this coupling in a single material has, with a few exceptions, proved to be elusive so far. The aim of this chapter is to present the reasons for these two obstacles and to illuminate some possible solutions.

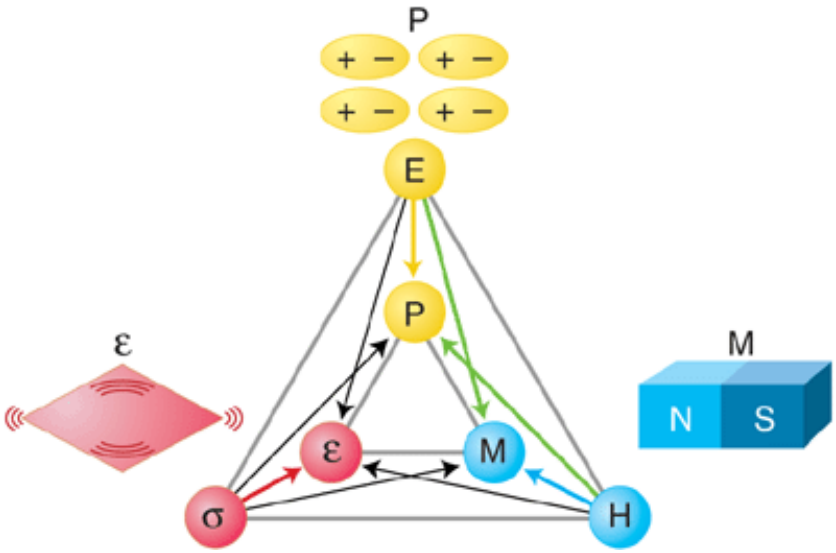

Figure 2.1: Multiferroics and magnetoelectrics: In a general solid state material, the material properties P (electric polarization), M (magnetization) and ϵ (strain) are controlled by the electric field E, magnetic field H, and stress σ, respectively. In a ferroic material,P,M, or ϵ are spontaneously formed to produce ferromagnetism, ferroelectricity, or ferroelasticity, respectively. Multiferroics is the name given to materials where the coexistence of at least two ferroic forms of ordering leads to additional interactions. In a magnetoelectric multiferroic, a magnetic field may control P or an electric field may control M (green arrows). [8]

2.1 Incompatibility between ferroelectricity and magnetism

The first limitation has to do with symmetry considerations. A condition for ferroelectricity is the breaking of spatial inversion symmetry of a high-symmetry paraelectric phase. In contrast, broken time inversion symmetry is a prerequisite for magnetism [1]. With this in mind, only 13 of the 233 Shubnikov magnetic point groups allow for the coexistence of ferroelectricity and magnetism. However, as some compounds belonging to these point groups do not show multiferroicity, more conditions, possibly different from symmetry considerations, seem to have to be fulfilled.

A large portion of the search for multiferroics have concentrated on the transition metal (TM) oxides with perovskite structure (ABO_3), since many technologically important ferroelectrics are found in this category, such as $BaTiO_3$ and $PbTiO_3$. At the same time a large number of magnetic oxides

with perovskite structure are known to exist. In spite of the existence of hundreds of magnetic oxides and ferroelectric oxides, there is practically no overlap between the two categories. A reason for this seeming mutual exclusion might be that the B-site cation appears to always require an empty d-shell as a prerequisite for ferroelectricity. Magnetism on the other hand requires partially filled $d-$ or $f-$shells, because in a filled shell the electron spins add up to zero and do not participate in magnetic ordering.

Several different approaches have been explored to circumvent this seeming incompatibility. The first breakthrough into applicable ME devices was the combination of ferroelastics and magnetoelastics into composite multilayers, where the ME coupling is manifested through a macroscopic mechanical transfer process. While the ME coupling in such composite systems is strong enough for certain applications, such as hard drive reading heads based on giant magnetoresistance [9, 10], it is somewhat unsatisfactory from a theoretical point of view.

One possible road to single phase multiferroics is to synthesize a compound with two distinct structural units. A well-known example of this are the borates, such as $GdFe_3(BO_3)_4$, where the BO_3 groups are ferroelectric and the Fe^{3+} ions are magnetic [11, 12]. Among the perovskites, one of the most studied compounds of this kind is $PbFe_{1/2}Nb_{1/2}O_3$, where the B-sites are occupied by a mix of ferroelectric Nb^{5+} and magnetic Fe^{3+} [13]. Careful studies have revealed that a magnetoelectric coupling between the two orders is present, albeit very weak [14]. The ferroelectricity in such compounds originates from some form of structural instability, either a polar shift to better facilitate electron pairing, or a more complex lattice distortion. The ME coupling in these systems is always weak because the two orders originate from different kinds of ions or subsystems, but some fascinating effects have been found, such as the magnetic phase control by an electric field in hexagonal $HoMnO_3$ [15].

2.2 Spiral spin order

All the examples in the previous section are usually referred to as Type I multiferroics. Judging from their properties, it seems that the key to a strong magnetoelectric coupling lies in finding a common origin of magnetic order and ferroelectricity. A possible solution to this problem would be if the ferrolectricity arose from the magnetic ordering itself. Materials with this property have been found and are known as Type II multiferroics, in which ferroelectricity exists only in a magnetically ordered state and is caused by a particular magnetic structure. For example, $TbMnO_3$ is magnetically ordered

below $T_N = 41$ K, but it is only below $T_C = 28$ K, where the magnetic structure changes, that a nonzero electric polarization appears. The ME coupling manifests itself strongly in $TbMnO_3$ through a 90° change of the electric polarization direction (a "flop") under the application of a magnetic field along a certain direction [16]. Similar behavior occurs in $TbMn_2O_5$, where the polarization changes sign with field [17]. The magnetic structure responsible for this behavior has been found to be the so-called spiral spin order (a more correct nomenclature would be helical or cycloidal spin order). In the following, we will take a closer look at this phenomenon.

As mentioned in the previous section, ferroelectricity and magnetism require different symmetry conditions. The requirement for ferroelectricity is the breaking of spatial inversion symmetry, such that the sign of the electric polarization $\mathbf{P}$ is switched upon the substitution $\mathbf{r} \to -\mathbf{r}$, but may remain unchanged upon the time reversal operation $t \to -t$. Magnetism, on the other hand, requires broken time-reversal symmetry, in which the magnetization $\mathbf{M}$ changes sign upon time reversal and may remain invariant upon spatial inversion. Given these constraints, let us try to construct a magnetoelectric coupling between $\mathbf{P}$ and $\mathbf{M}$ that is invariant upon both inversion and time reversal, following the calculation outlined in [18].

Firstly, since time reversal $t \to -t$ transforms $\mathbf{M} \to -\mathbf{M}$ and leaves $\mathbf{P}$ invariant, the magnetoelectric coupling has to be quadratic in $\mathbf{M}$. Secondly, spatial inversion symmetry is respected when the coupling between a homogeneous polarization and an inhomogeneous magnetization is linear in $\mathbf{P}$ and contains one gradient of $\mathbf{M}$. In the simplest case of cubic symmetry, this leads to the following magnetoelectric coupling term in the Landau free energy [18, 19, 20]:

$$\Phi_{\mathrm{ME}}(\mathbf{r}) = \mathbf{P} \cdot \left\{ \gamma \cdot \nabla(\mathbf{M}^2) + \gamma' \left[\mathbf{M}(\nabla \cdot \mathbf{M}) - (\mathbf{M} \cdot \nabla)\mathbf{M} \right] + \ldots \right\}, \tag{2.1}$$

where γ and γ' are the coupling coefficients. The first term in the free energy is proportional to the total derivative of the square of magnetization, and gives contribution only if $\mathbf{P}$ is assumed to be independent of $\mathbf{r}$ [18, 19, 20]. Since we've already established that spatial inversion invariance needs to be broken for ferroelectricity to take place, it is imperative *not* to make this assumption. However, since the ferroelectricity in this model arises from the magnetic ordering, we do assume that the system shows no instability towards ferroelectricity in the absence of magnetism. We therefore keep only the quadratic term in the electric part of the free energy:

$$\Phi_{\mathrm{E}}(\mathbf{r}) = \frac{\mathbf{P}^2}{2\chi_E}, \tag{2.2}$$

where χ_E is the dielectric susceptibility in absence of magnetism. A minimization of the total free energy $\Phi_{\mathrm{E}} + \Phi_{\mathrm{ME}}$ with respect to $\mathbf{P}$ then gives us [18]

$$\mathbf{P} = \gamma' \chi_E \left[(\mathbf{M} \cdot \nabla)\mathbf{M} - \mathbf{M}(\nabla \cdot \mathbf{M}) \right]. \tag{2.3}$$

To see how this electric polarization could manifest itself in a physical system, let us consider a spin density wave (SDW) with the wave vector $\mathbf{Q}$,

$$\mathbf{S} = S_1 \mathbf{e}_1 \cos \mathbf{Q} \cdot \mathbf{r} + S_2 \mathbf{e}_2 \sin \mathbf{Q} \cdot \mathbf{r} + S_3 \mathbf{e}_3 \tag{2.4}$$

where the unit vectors $\mathbf{e}_i$ $(i = 1, 2, 3)$ form an orthogonal basis. Such a spin structure could arise from a competition between a ferromagnetic nearest-neighbor interaction and an antiferromagnetic next-nearest-neighbor interaction, which frustrates the spin order [21].

If only S_1 or S_2 is non-zero, equation (2.4) describes a sinusoidally modulated SDW, which can not induce any ferroelectricity because it is invariant upon spatial inversion. This is reflected in equation (2.5) below. For $S_1, S_2 \neq 0$ equation (2.4) describes an (elliptical) helix with spin rotation axis $\mathbf{e}_3$. (If also S_3 is non-zero, the helix is conical.) For such helical order, like for any magnetic ordering, time reversal symmetry is spontaneously broken. Spatial inversion symmetry is also broken, because the translation $\mathbf{r} \to -\mathbf{r}$ inverts the helicity of the spin rotation. This allows for an average ferroelectric polarization transverse to both $\mathbf{e}_3$ and $\mathbf{Q}$ and independent of S_3, found by combining equations (2.3) and (2.4):

$$\bar{\mathbf{P}} = \frac{1}{V} \int d^3x \mathbf{P} = \gamma' \chi_E S_1 S_2 [\mathbf{e}_3 \times \mathbf{Q}] \tag{2.5}$$

This equation also holds for orthorhombic crystals, provided that $\mathbf{e}_3$ and $\mathbf{Q}$ are parallel to crystal axes [18].

2.2.1 Microscopic Mechanism

To summarize the last section, the ferroelectric order is established through two or more competing magnetic interactions inducing the spiral order, which breaks spatial-inversion and time-reversal symmetries simultaneously. However, the microscopic mechanism directly responsible for ferroelectricity in a magnetic spiral system is complex and not fully understood. Three theories on the subject have been proposed: the inverse Dzyaloshinskii-Moriya (DM) model [22], the spin current model [23], and the electric current cancellation model [24]. In the following, we will only consider the first model and give

an outline of how it can lead to ferroelectricity in the typical multiferroic $TbMnO_3$, as originally put forward by Sergienko and Dagotto [22].

The inverse DM model proposes ferroelectricity in spin spiral systems to be a result of displacement of oxygen ions driven by the antisymmetric Dzyaloshinskii-Moriya interaction. Between two localized magnetic moments S_i and S_j, the DM interaction takes the form [25]

$$H_{ij}^{\mathrm{DM}} = \mathbf{D}_{ij} \cdot (\mathbf{S}_i \times \mathbf{S}_j), \tag{2.6}$$

where the prefactor $\mathbf{D}_{ij}$ is called the DM factor, and is dependent on the spin-orbit coupling constant γ and the displacement of the interstitial oxygen ion (see figure 2.2). We will first consider the role of the normal symmetric superexchange interaction in $TbMnO_3$, before adding on the antisymmetric DM interaction and see how it is necessary for ferroelectricity to arise.

A helically ordered magnetic structure, such as the one observed below 28 K in $TbMnO_3$, can be described by equation (2.4), rewritten in crystal coordinates as $S_n^i = S_0^i \cos(n\theta + \alpha^i)$, where $i = (x, y, z)$. For $TbMnO_3$, $S_0^x = S_0^y = S_0^z = 1.4$, $\theta = 0.28\pi$ and α^i is a constant not critical to the physics. Since the presumption is that ferroelectricity is caused by the displacement of oxygen ions relative to the manganese, we assume that the position of Mn ions are fixed and oxygen may displace from their center positions. We will later see that this assumption is natural to make based on the crystal structure of $TbMnO_3$. The isotropic superexchange interaction of a Mn-O-Mn chain in the x direction can then be described as [22]

$$H_{ex} = -\sum_n \left[J_0 + \frac{1}{2} J'_{\parallel} x_n^2 + \frac{1}{2} J'_{\perp} (y_n^2 + z_n^2) \right] (\mathbf{S}_n \cdot \mathbf{S}_{n+1}), \tag{2.7}$$

where J_0, $J'_{\parallel}$ and $J'_{\perp}$ are the exchange constants, and $r_n = (x_n, y_n, z_n)$ is the displacement of oxygen ions located between the Mn spins S_n and S_{n+1}.

In an orthorhombically distorted structure, the displacement of the oxygen ions will have contributions from the crystal structure itself as well as the DM interaction, such that

$$\mathbf{r}_n = (-1)^n \mathbf{r}_0 + \delta \mathbf{r}_n, \tag{2.8}$$

where $\mathbf{r}_0$ is constant and $\delta \mathbf{r}_n$ is the additional displacement due to the spiral magnetic structure.

The oxygen displacement is in competition with the (isotropic) elastic energy, which can be expressed as $H_{\mathrm{el}} = \kappa \sum_n (\delta x_n^2 + \delta y_n^2 + \delta z_n^2)$. Taking this into account, it can be shown that the portion of the Hamiltonian depending

on $\delta\mathbf{r}_n$ is [22]

$$\delta H_{\text{ex}} = \sum_n (-1)^{n+1} \left[J'_{\parallel} x_0 \delta x_n + J'_{\perp} (y_0 \delta y_n + z_0 \delta z_n) \right] (\mathbf{S}_n \cdot \mathbf{S}_{n+1}) + H_{\text{el}}. \quad (2.9)$$

For the spin spiral structure, a minimization of δH_{ex} with respect to the displacements yields [22]

$$\delta z_n = (-1)^n \frac{J'_{\perp} z_0}{2\kappa} \sum_i {S_0^i}^2 \{\cos\theta + \cos[(2n+1)\theta + 2\alpha_i]\} \quad (2.10)$$

and similar expressions for δx_n and δy_n. This model can reproduce observed structural modulations [16], but no net ferroelectric polarization, since the sum of all displacements is exactly zero.

To explain how ferroelectricity arises from a helical magnetic structure we have to take into account the antisymmetric DM interaction in equation (2.6), which in the perovskite structure takes the form $\mathbf{D}^{\mathbf{a}}(\mathbf{r}_n) \cdot [\mathbf{S}_n \times \mathbf{S}_{n+1}]$, where

$$\mathbf{D}^{\mathbf{x}}(\mathbf{r}_n) = \gamma \begin{pmatrix} 0 \\ -z_n \\ y_n \end{pmatrix}, \quad \mathbf{D}^{\mathbf{y}}(\mathbf{r}_n) = \gamma \begin{pmatrix} z_n \\ 0 \\ -x_n \end{pmatrix} \quad (2.11)$$

for the Mn-O-Mn bonds along the x and y axes, respectively. If we consider a Mn chain in the x direction, the portion of the Hamiltonian depending on $\delta\mathbf{r}_n$ is

$$\delta H_{\text{DM}} = \sum_n \mathbf{D}^{\mathbf{x}}(\delta\mathbf{r}_n) \cdot [\mathbf{S}_n \times \mathbf{S}_{n+1}] + H_{\text{el}}. \quad (2.12)$$

Minimizing δH_{DM} with respect to the displacement now gives us [22]

$$\delta z_n = \frac{\gamma}{\kappa} S_0^x S_0^y \sin\theta \sin(\alpha_x - \alpha_z), \quad (2.13)$$

$$\delta x_n = \delta y_n = 0. \quad (2.14)$$

The same result is obtained for the Mn chain in the y direction. For a collinear magnetic structure such as the one found in the paramagnetic phase of $TbMnO_3$, either S_0^x or S_0^y is zero, leading to no net displacement according to equation (2.13). If however both S_0^x and S_0^y are non-zero, as is the case for a spin spiral, we get a net ferroelectric polarization along the z axis, since the oxygen displacement δz_n does not depend on n.

Thus we have a microscopic mechanism for ferroelectricity arising from a specific magnetic structure that is compatible with the symmetry arguments

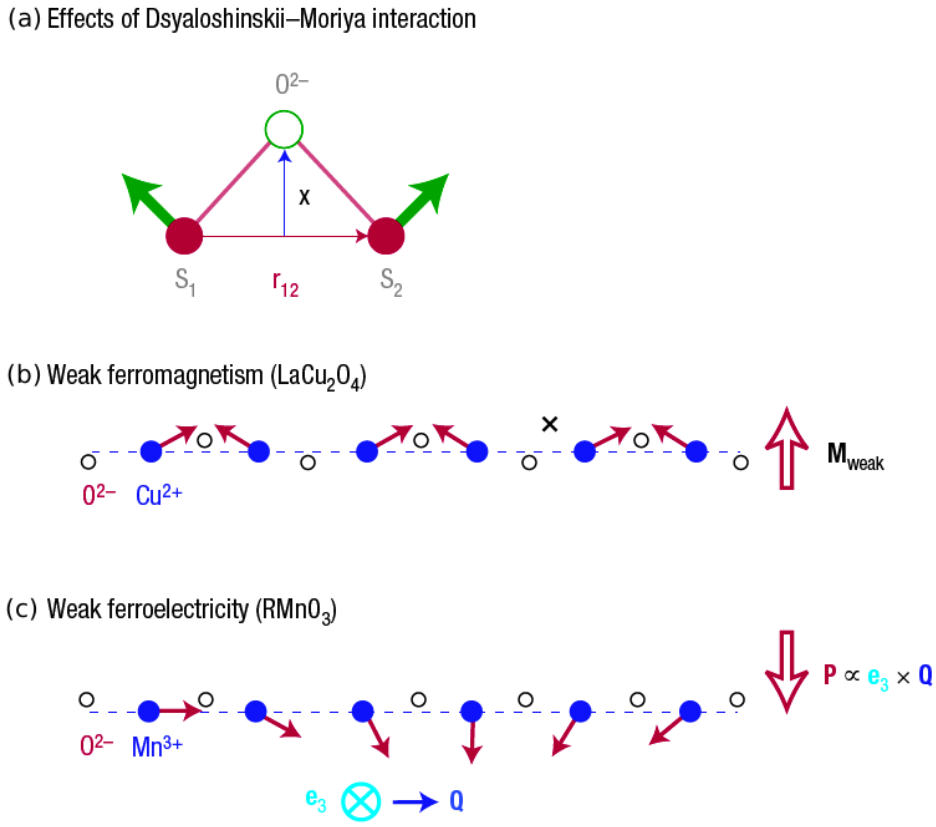

Figure 2.2: (a) The antisymmetric DM interaction is given by $H_{ij}^{\mathrm{DM}} = \mathbf{D}_{ij} \cdot (\mathbf{S}_i \times \mathbf{S}_j)$, where $\mathbf{D}_{ij}$ is dependent on the oxygen displacement $\mathbf{x}$: $\mathbf{D}_{12} = \gamma \mathbf{x} \times \mathbf{r_{12}}$ (b) With alternating DM vectors, such as in antiferromagnetic $LaCu_2O_4$ layers, the DM interaction causes spin canting leading to weak ferromagnetism. (c) In a spiral spin system such as $R\mathrm{MnO}_3$, the inverse DM interaction causes a displacement of oxygen ions that gives rise to an electric polarization perpendicular to the spin rotation axis $\mathbf{e}_3$ and the wave vector $\mathbf{Q}$ [26].

mentioned in the last section. Comparing equations (2.5) and (2.13), we see that they both result in an average ferroelectric polarization if the magnetic structure is not collinear. The inverse DM model as described here has produced a phase diagram for $TbMnO_3$ that is in excellent agreement with experiments [22]. In the next section, we will cast our net wider and take a look at the multiferroic properties of a range of heavily studied perovskites similar in structure to $TbMnO_3$.

2.3 The $R\mathrm{MnO}_3$ system

The compound that hurled perovskites into the limelight of multiferroics research was $TbMnO_3$, in a 2003 Nature article by Kimura *et al.* [16]. They showed that $TbMnO_3$ exhibits spontaneous electric polarization along c below 28 K coinciding with a commensurate AFM magnetic structure. Moreover, they demonstrated the existence of a polarization flop transition under application of magnetic field along the b axis, where the ferroelectric polarization changes direction from c to a. Since then, a variety of magnetic and electric phases have been discovered in the $R\mathrm{MnO}_3$ series of compounds, where R is a trivalent rare earth ion.

The common crystal structure of all these compounds is displayed in figure 2.3(a) and is characterized by Mn^{3+} ions centered in canted oxygen octahedra. The orthorhombic distortion of the structure, i.e. the canting of the MnO_6 octahedra, is governed by the ionic radius of the rare earth ion situated between the octahedra, with the strongest distortion occurring in compounds with the smaller-sized R ion. There is therefore a direct link between the size of the rare earth ion and the Mn-O-Mn bond angles, which in turn influence the relative magnitude of nearest-neighbor ferromagnetic (J_1) and next-nearest-neighbor antiferromagnetic (J_2) exchange interactions.

The weakly distorted materials with R=La,Pr,...,Eu,Gd exhibit A-type antiferromagnetic ground states [AFM(A)] (ferromagnetic sheets in the ab plane stacked antiferromagnetically along c)[1] which are also weakly ferromagnetic [WFM], while the strongly distorted materials with R=Ho,...,Yb,Lu exhibit E-type antiferromagnetic [AFM(E)] order, i.e. an up-up-down-down spin configuration, in the ground state (see figure 2.3(b)) [28, 29]. In the moderately distorted materials sandwiched between these two regions, with R=Tb and Dy, cycloidal spin order is observed. This spiral spin order is responsible for the ferroelectricity in $TbMnO_3$, as described in the previous section. But the phase diagram contains a richness beyond just a low-temperature FE phase.

In $TbMnO_3$, a sinusoidal collinear order of the Mn spins occurs at the Néel temperature $T_N^{\mathrm{Mn}} \sim 41$K [30, 31]. In this phase, the Mn spins are aligned along the b axis with an incommensurate propagation wave vector $\mathbf{q}^{\mathrm{Mn}} = (0, 0.28, 1)$, and the sample is paraelectric. Ferroelectricity along the c axis (P_c) shows up below $T_C \sim 28$K concomitantly with a magnetic transition into a cycloidal spin order with Mn spins rotating within the bc

[1] Different types of (anti)ferromagnetic order are usually designated with capital letters, with the most common being A: in-plane ferromagnetic and out-of-plane antiferromagnetic; C: in-plane antiferromagnetic and out-of-plane ferromagnetic; F: in-plane and out-of-plane ferromagnetic; and G: in-plane and out-of-plane antiferromagnetic.

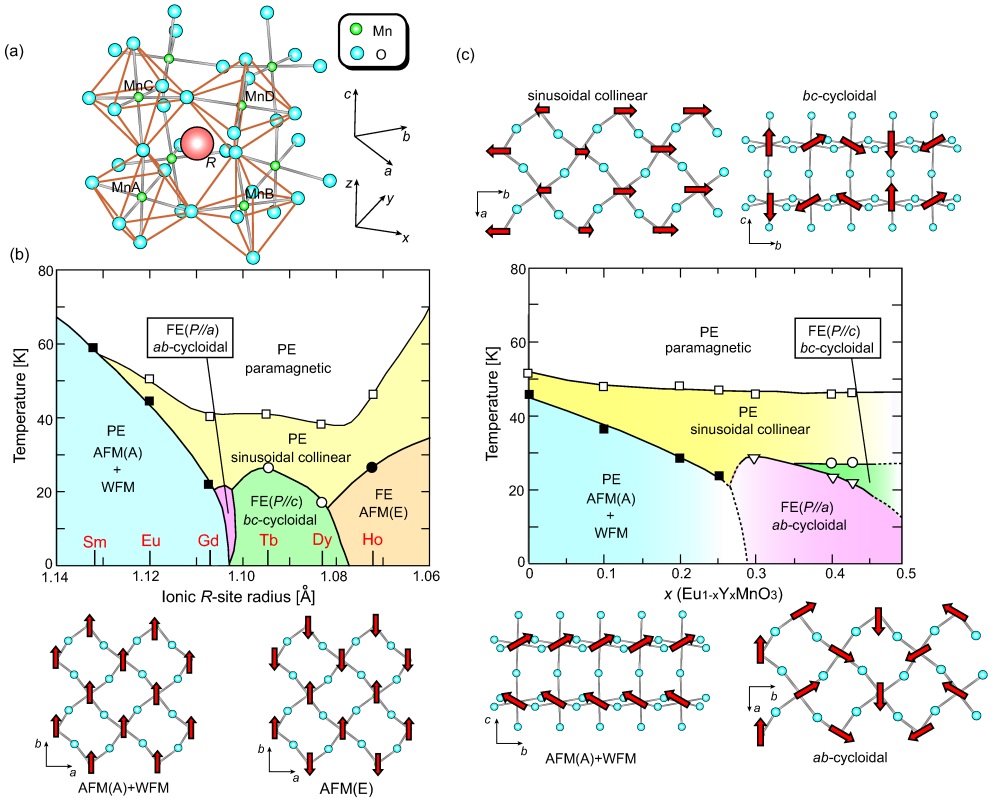

Figure 2.3: (a) Perovskite structure of $R\mathrm{MnO_3}$. (b) Experimentally obtained magnetoelectric phase diagram of $R\mathrm{MnO_3}$ as function of temperature and ionic R-site radius. Insets show spin configuration of the A-type and E-type antiferromagnetic states. Along the c axis, spins stack antiferromagnetically. (c) Experimentally obtained magnetoelectric phase diagram of $\mathrm{Eu}_{1-x}\mathrm{Y}_x\mathrm{MnO_3}$ as function of temperature and Y concentration x. Insets show spin configurations of the *ab*-cycloidal, *bc*-cycloidal, and sinusoidal collinear states [27].

plane [32]. At these temperatures, the Tb f-electron moments are clamped to the Mn moments, whereas below $T_N^{\mathrm{Tb}} \sim 7\mathrm{K}$ ordering of the Tb moments takes place with a different wave vector $\mathbf{q}^{\mathrm{Tb}} \sim (0, 0.42, 1)$. $\mathrm{DyMnO_3}$ shows similar orderings and transitions with $T_N^{\mathrm{Mn}} \sim 39\mathrm{K}$, $\mathbf{q}^{\mathrm{Mn}} \sim (0, 0.36, 1)$, $T_C \sim 19\mathrm{K}$, $T_N^{\mathrm{Dy}} \sim 5\mathrm{K}$ and $\mathbf{q}^{\mathrm{Dy}} \sim (0, 0.5, 1)$ [33].

In $\mathrm{TbMnO_3}$ and $\mathrm{DyMnO_3}$ in zero field, the only FE phase observed is the *bc*-cycloidal spin structure with P_c. However, by continuously decreasing the lattice distortion by substituting Tb with Gd in $\mathrm{Tb}_{1-x}\mathrm{Gd}_x\mathrm{MnO_3}$, the spin structure changes to an *ab* cycloid with FE polarization along a (P_a) at a critical Gd concentration x [34]. This is illustrated by the pink region in the

phase diagram in figure 2.3(b), and emphasizes again the importance of the orthorhombic distortion on the ME properties of these materials.

The above-mentioned multiferroic properties are primarily related to the Mn magnetism, although rare earth magnetism causes some interesting additional effects that we will go into later. In order to study the effect of distortion on an isolated Mn magnetic system in the perovskite structure without influence from rare earth magnetism, the solid solution system $Eu_{1-x}Y_xMnO_3$ has been experimentally studied for compositions $0 \leq x \lesssim 0.5$ as functions of temperature and Y concentration x [35, 36, 37]. This range of x covers approximately the region from Eu to Tb in figure 2.3(b) with rare earth magnetism removed, since Eu^{3+} ($4f^3$) and Y^{3+} ([Kr]) are non-magnetic. The corresponding phase diagram is shown in figure 2.3(c), and one immediately recognizes most of the multiferroic phases seen in other multiferroic perovskites. The ground state changes at approximately $x \sim 0.2 - 0.3$ from the canted WFM-AFM(A) state without ferroelectric order towards the presumably *ab*-cycloidal spin state with P_a. For higher Y concentrations $x \geq 0.4$, the ferroelectric polarization spontaneously changes from P_a at lower temperatures towards P_c at higher temperatures. The temperature range of this P_c phase is extended with increasing x, resembling the polarization flop going from Gd to Tb in $Tb_{1-x}Gd_xMnO_3$. Increasing x beyond 0.5 destabilizes the orthorhombic structure, and hexagonal impurities start to appear.

In summary, the manganite system with perovskite structure exhibits the WFM-AFM(A), *ab*-cycloidal (P_a), *bc*-cycloidal (P_c), and AFM(E) phases successively as the orthorhombic distortion increases. Of particular interest is the polarization flop transition from P_a to P_c, since such a property could be useful for applications. A microscopic mechanism responsible for this behavior has been proposed by M. Mochizuki and N. Furukawa [27]. In their work, as others before them [38, 39, 40, 28], they consider the fact that the increased tilting of the MnO_6 octahedra caused by decreasing R-site ionic radii enhances the next-nearest-neighbor antiferromagnetic exchange J_2, which competes with the nearest-neighbor ferromagnetic exchange J_1 in the *ab* plane. Spiral spin order can be attributed to this competition. The resulting relative weakening of the in-plane ferromagnetic interactions causes the observed reduction in the Néel temperature in the WFM-AFM(A) phase with decreasing R-site radius. Moreover, they explain the spin flop transition from an *ab* cycloid to a *bc* cycloid as a reduction of the energy gain due to the in-plane DM interaction as the spin spiral rotation angle increases with increasing J_2. At a certain point, the system favors a *bc* cycloid stabilized by the out-of-plane DM interaction, causing the observed flop of FE polarization from P_a to P_c. Their model is able to reproduce a majority of the features of the phase diagrams in figure 2.3.

2.3.1 Dzyaloshinskii-Moriya canting in $R\mathrm{MnO}_3$

We established in section 2.2.1 that the inverse DM interaction between neighboring Mn moments is primarily responsible for the oxygen shifts leading to ferroelectricity in $R\mathrm{MnO}_3$. But the DM interaction also has a direct influence on the moment directions, complicating the picture further. When the DM interaction was originally introduced, it was to explain the origin of weak ferromagnetism in antiferromagnetic materials. If the crystal structure has zigzag-type ligand shifts, the DM interaction would cause uniaxial F type spin canting, imparting an average weak magnetization to the compound [41, 25]. This weak ferromagnetism has been observed in the orthorhombic perovskites La_2CuO_4 and $LaMnO_3$, which have A type AFM magnetic structures [42, 43] (see figure 2.2).

The $R\mathrm{MnO}_3$ compounds also possess the zigzag-type shifts, so the DM interaction is expected to introduce F type canting of the Mn magnetic moments in $R\mathrm{MnO}_3$. The combination of the inverse and ordinary DM interactions could result in complex new magnetic structures. Let us study this effect more closely, following the derivation in [44].

Consider a Mn-O-Mn chain along the c axis with a transverse oxygen shift $\mathbf{x} = x\hat{\mathbf{b}}$, as a result of the canting of the oxygen octahedra. The magnetic structure is of the A type because the symmetric superexchange interaction $H_{\mathrm{SE}} = J\mathbf{S}_i \cdot \mathbf{S}_j$ $(J > 0)$ makes spins in neighboring crystallographic planes antiparallel. The DM interaction $H_{\mathrm{DM}} = \mathbf{D}_{ij} \cdot \mathbf{S}_i \times \mathbf{S}_j$ is induced by the shift $\mathbf{x}$ through the DM factor

$$\mathbf{D}_{ij} = \gamma \mathbf{x} \times \hat{\mathbf{r}}_{ij}, \tag{2.15}$$

where γ is the spin-orbit coupling constant and $\hat{\mathbf{r}}_{ij}$ is a unit vector from S_i to S_j [26, 41, 25, 22]. The wave vector of the spin structure can be written as $\boldsymbol{\tau} = \tau\mathbf{b}$. The spin direction of a single moment $\mathbf{m}_i^A$ in the A type b sinusoidal structure associated with the paraelectric phase $T_C < T < T_N$ can then be described by

$$\mathbf{m}_i^A = m_b^A \cos(\boldsymbol{\tau} \cdot \mathbf{r}_i)\hat{\mathbf{b}}. \tag{2.16}$$

Likewise, the spin directions in the A type ab cycloidal structure associated with the low temperature ferroelectric phase of $\mathrm{Eu}_{1-x}\mathrm{Y}_x\mathrm{MnO}_3$ can be written as

$$\mathbf{m}_i^A = m_b^A \cos(\boldsymbol{\tau} \cdot \mathbf{r}_i)\hat{\mathbf{b}} + m_a^A \sin(\boldsymbol{\tau} \cdot \mathbf{r}_i)\hat{\mathbf{a}}. \tag{2.17}$$

The A type bc cycloid associated with $P \| c$ can be expressed in a similar fashion. With the oxygen shifting in a zigzag-like pattern with $\mathbf{x} = \pm x\hat{\mathbf{b}}$,

Temperature	A type	F type	C type	G type
$T > T_C$	b sinusoid	c sinusoid	-	a sinusoid
$T < T_C$, $P \| c$	bc cycloid	bc cycloid	a sinusoid	a sinusoid
$T < T_C$, $P \| a$	ab cycloid	c sinusoid	c sinusoid	ab cycloid

Table 2.1: Magnetic structure components resulting from DM canting of A type Mn moments in $R\mathrm{MnO_3}$.

the DM factor (2.15) becomes $\mathbf{D}_{ij} = \pm D_{ij}\hat{\mathbf{a}}$. H_{DM} therefore acts only on m_b^A and m_c^A, and causes F type spin canting towards the c and b directions, respectively, i.e.

$$m_b^A \rightarrow m_c^F,\ m_c^A \rightarrow -m_b^F,\ m_a^A \rightarrow 0. \tag{2.18}$$

This spin canting would lead to an additional F type magnetic structure superposed on the A type structure. For the A type b sinusoid, the F type order is predicted to be the c sinusoid

$$\mathbf{m}_i^F = m_c^F \cos(\boldsymbol{\tau} \cdot \mathbf{r}_i)\hat{\mathbf{c}}. \tag{2.19}$$

The A type bc cycloid responsible for ferroelectricity in $\mathrm{TbMnO_3}$ and $\mathrm{DyMnO_3}$ would lead to an F type bc cycloid, while the F type structure due to spin canting of the A type ab cycloid in $\mathrm{Eu_{1-x}Y_xMnO_3}$ and $\mathrm{Tb_{1-x}Gd_xMnO_3}$ is predicted to be the c sinusoid, since $m_a^A \rightarrow 0$. These F type structures have been observed in $\mathrm{TbMnO_3}$ and $\mathrm{Eu_{3/4}Y_{1/4}MnO_3}$ [44].

Furthermore, just as F type canting is induced by a transverse oxygen shift in the b direction of the Mn-O-Mn bonding along c, oxygen ion shifts in the a direction will induce C type canting. Likewise, G type canting is induced by oxygen ion shifts in the $\mathrm{MnO_2}$ plane [45]. C type canting would transform a components into c components and vice versa, while G type canting would transform a to b and vice versa [44, 46], i.e.

- C type canting: $m_a^A \rightarrow m_c^C$, $m_b^A \rightarrow 0$, $m_c^A \rightarrow m_a^C$
- G type canting: $m_a^A \rightarrow m_b^G$, $m_b^A \rightarrow m_a^G$, $m_c^A \rightarrow 0$

The additional components of the magnetic structure that would result from all these transformations are listed in table 2.1. The resulting F, C and G type magnetic orders agree with magnetic symmetry arguments [44, 47].

2.3.2 $R\mathrm{MnO_3}$ in electromagnetic fields

A new level of complexity arises in the $R\mathrm{MnO_3}$ compounds when an external magnetic field is applied. As already mentioned in section 2.3, the polarization flop from P_c to P_a may also be induced in $\mathrm{TbMnO_3}$ by application of

an external magnetic field along b. This polarization flop is accompanied by a sudden change from an incommensurate to a commensurate wave vector modulation. A similar polarization flop from P_c to P_a is observed in $DyMnO_3$ in an applied magnetic field. In this case however, the wave vector of the magnetic structure varies continuously through the flop transition [48].

$Eu_{1-x}Y_xMnO_3$ with $x = 0.4$ also exhibits a field-induced polarization flop transition, but in the opposite direction. As seen from the phase diagram in figure 2.3(c), the polarization flop transition from P_a to P_c is induced by increasing the temperature, but the same transition is also observed by application of an external magnetic field along a [36].

In the crossover region from AFM(A) to FE(P_a) in $Eu_{1-x}Y_xMnO_3$, i.e. for $x \sim 0.2 - 0.3$, a strong competition between the two phases exist. Which phase a certain compound chooses may be influenced by the application of electric or magnetic fields, allowing for cross-control of magnetization and polarization. For example, $Eu_{0.8}Y_{0.2}MnO_3$ has been observed to have a history-dependent ground state, choosing the ferroelectric state after zero-field cooling and the weakly ferromagnetic state after cooling in a field of 5 T. Moreover, the ferroelectric state could be induced by applying an alternating magnetic field, suggesting the development of the ferroelectric phase during the magnetization reversal process [49]. It has been speculated that the coexistence of ferromagnetism and ferroelectricity in the same phase was possible for $x \sim 0.2$ samples [35], but more recent results [36] do not support the simultaneous coexistence. However, a magnetoelectric glass state with coexisting phases has been observed in the similar compound $Eu_{3/4}Y_{1/4}MnO_3$ [50].

2.3.3 The effect of rare earth magnetism

In the discussion above we have tried to explain the multiferroic properties as results of the interplay between Mn spins only, and rare earth magnetism has not come into consideration. However, several of the rare earths have rather large magnetic moments situated in the f shell, which should be expected to play a role as well. And indeed, a number of exotic effects that can be ascribed to the rare earth magnetism have been observed in the $RMnO_3$ system.

In $TbMnO_3$ a harmonic coupling between the ordering wave vectors τ^{Tb} and τ^{Mn} of Tb and Mn spins has been observed. In zero field the relation $3\tau^{Tb} \pm \tau^{Mn} = 1$ is obeyed as the Tb spins attempt to find the best possible ordering within a background of a Mn cycloid. The harmonic relation results from a quartic coupling between the Tb and Mn magnetic order parameters. In an applied magnetic field a homogeneous component is added to the coupling, and the quartic coupling effectively leads to the harmonic relation

$2\tau^{\mathrm{Tb}} \pm \tau^{\mathrm{Mn}} = 1$ instead [35]. This explains the sudden change of wave vector by application of an external magnetic field in the compound.

In $DyMnO_3$ the Dy orders *commensurately* below 6.5 K. This commensurate Dy order is accompanied by an *incommensurate* lattice modulation [33]. Above 6.5 K, or when applying a magnetic field along a, Dy exhibits a Mn-induced ordering. In this phase, where the Dy and the Mn order with the same wave vector, a threefold enhancement of the electric polarization is observed [51, 52]. On the other hand, the harmonic coupling between the Tb and Mn wave vectors in $TbMnO_3$ has only a minimal effect on the ferroelectricity.

In contrast to $TbMnO_3$ and $DyMnO_3$, $GdMnO_3$ shows no ferroelectricity in the ground state, and is only ferroelectric under application of an external magnetic field and in a narrow temperature range in zero field. The Gd spins order below 7 K, and a phase boundary within the Gd ordered state coincides with the paraelectric-to-ferroelectric transition, suggesting that the Gd ordering in magnetic field stabilizes ferroelectricity in this compound. It has been hypothesized that symmetric R-Mn exchange striction, similar to the one derived in equation (2.10), is responsible for the field induced ferroelectricity in $GdMnO_3$ as well as for the polarization enhancement and incommensurate lattice modulation in $DyMnO_3$ [53].

$DyMnO_3$ has also been the subject of a novel approach by Schierle *et al.* to control ferroelectric domain structures by photons that use the local charging of the sample surface by the photoelectric effect [6]. They were able to imprint two ferroelectric domains with opposite polarization by illuminating a spot on the sample during cooling.

Chapter 3

Experimental Techniques

X rays were discovered in November 1895 by Wilhelm Conrad Röntgen and famously led to big advances in the field of medicine, due to their ability to penetrate biological matter and record high contrast images of internal organs such as bone structure. The high contrast is a result of the x-ray absorption's strong dependence on the number of electrons per atom [54]. Incidentally, the wavelength of light in the x-ray energy range is of the same order as the interatomic distances in most solids (0.1-100 Å), which makes it the perfect tool for interference and diffraction studies of periodic structures such as crystals. A few years after their discovery, Max von Laue and co-workers found that x-rays scattered from periodic crystals produce characteristic patterns [55, 56]. This discovery, together with the early work by Paul Peter Ewald, William Henry Bragg and William Lawrence Bragg (the latter two being father and son) laid the foundation for the field of x-ray crystallography, and many terms in use today are named after them, such as Laue patterns, the Ewald sphere, and Bragg's law.

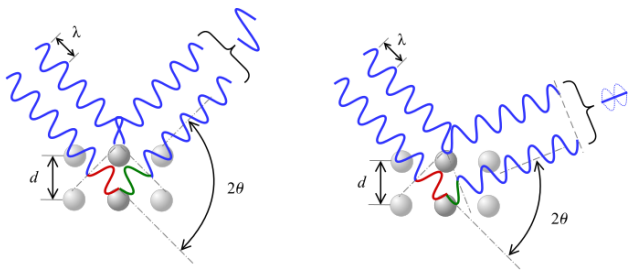

Figure 3.1: Classical picture of Bragg's principle for x-ray scattering from a solid. Constructive interference between two scattered waves with wavelength λ is realized if the reflection angle θ satisfies Bragg's law: $2d \sin\theta = n\lambda$. (Wikimedia Commons)

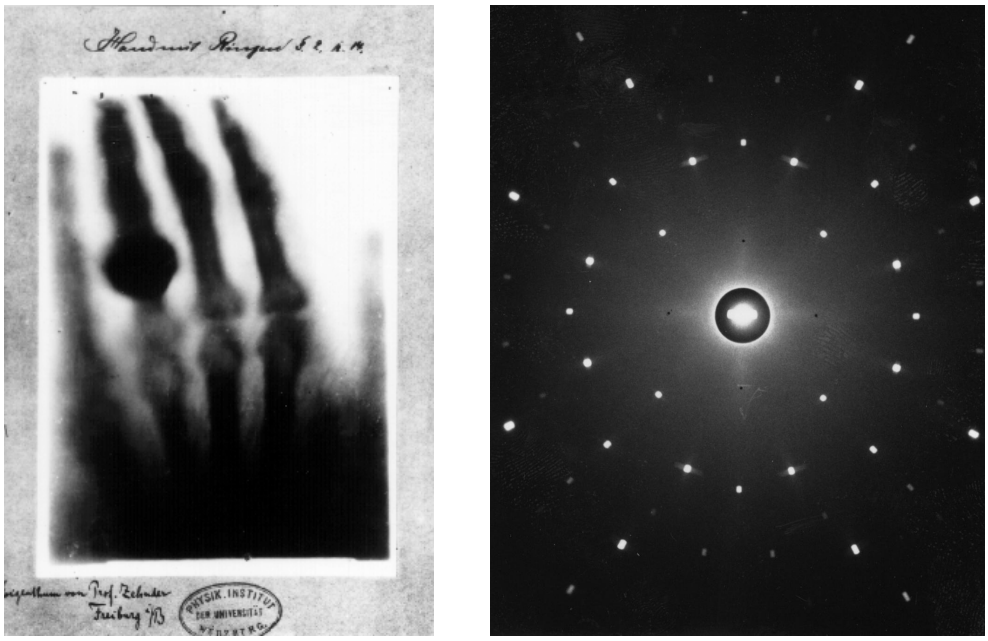

Figure 3.2: Left: First medical X-ray by Wilhelm Röntgen of his wife Anna Bertha Ludwig's hand. - (National Aeronautics and Space Administration) Licensed under Public domain via Wikimedia Commons. Right: Laue pattern of Si [57].

3.1 Synchrotron Radiation

From classical electrodynamics it is known that any accelerated charge will generate radiation. This was particularly evident in early particle accelerators. A typical particle accelerator consists of smaller pre-accelerators that feed into a so-called storage ring, where bunches of charged particles after being accelerated to relativistic speed are kept at constant energy ready to be used in collider experiments. The storage ring, or synchrotron, consists of several straigth sections that are arranged in a circle and connected with bending magnets for changing the path of the charged particles through the Lorentz force $\mathbf{F} = q\mathbf{v} \times \mathbf{B}$. This acceleration causes the particles to emit radiation tangential to the particle trajectory, from the visible to the x-ray photon energy range. In the early days of experimental particle physics, this bending magnet radiation was used parasitically for photon science research. Today, dedicated synchrotron radiation sources exist.

The synchrotron radiation for experiments at the first synchrotron radiation sources was generated by the bending magnets. At modern synchrotron radiation sources insertion devices such as wigglers and undulators placed in

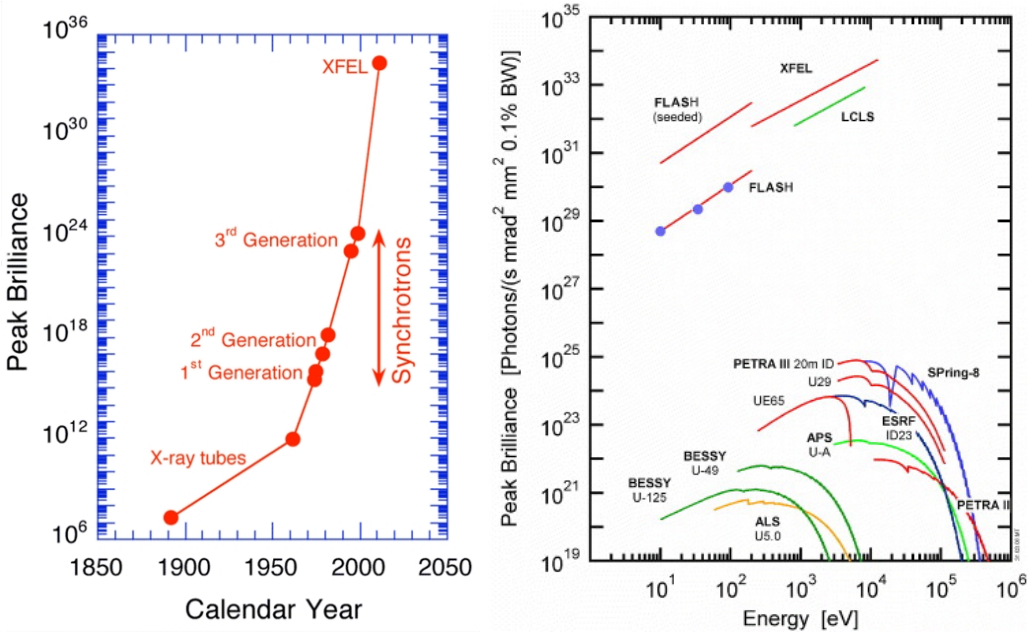

Figure 3.3: Left: History of the brilliance achieved at various x-ray sources [58]. Right: Peak brilliance as function of photon energy at various x-ray sources in operation today and in the near future [59].

the straigth sections are delivering highly collimated x-ray beams. Various optical devices and experiments can be put in the path of the radiation, in what is called a beamline. All experimental results in this thesis was obtained at beamlines using radiation generated by undulators.

In an undulator, the charged particle bunches pass a series of permanent magnets that are well aligned and shimmed, so that the particles see perfectly alternating fields. In the co-moving reference frame of the particle bunches, this causes the particles to oscillate transverse to the beam path, emitting radiation isotropically in all directions. Because of the relativistic Lorentz transformations, the radiation pattern in the lab frame becomes sharply peaked in the direction of motion of the radiating charge.

The major advantage of using synchrotron radiation for experiments is the high amount of collimated x-ray photons produced. This is usually quantified by the parameter brilliance, defined as [60]

$$\text{Brilliance} = \frac{\text{Photons/second}}{(\text{mrad})^2(\text{mm}^2\text{source area})(0.1\%\text{ bandwidth})} \tag{3.1}$$

Figure 3.3 shows the rapid development of achieved brilliance since the discovery of x-rays, as well as the peak brilliance of various x-ray sources in

operation today or in the near future. At modern 3rd generation synchrotron radiation sources the brilliance can be over ten orders of magnitude larger than at common lab sources. This allows for the detection of very weak signals such as the diffraction from magnetically ordered structures. Other advantages are energy tunability and polarization qualities. The radiation at a bending magnet or undulator beamline is highly polarized, as opposed to the unpolarized light produced by lab sources.

3.1.1 Polarized x-rays

For our purposes, the usual description of polarized light used in the visible regime is sufficient also for x-rays. We will here give a short presentation of the most important terms and conventions, following Detlefs et al. [61]. The x-rays are transverse electromagnetic waves, and an isolated wave with wave vector $\mathbf{k}$ and photon energy $\hbar\omega$ can be represented by the time- and space-dependent electric field vector

$$\mathbf{E}(t,\mathbf{r}) = \mathrm{Re}\left[(V_1\hat{\boldsymbol{\epsilon}}_1 + V_2\hat{\boldsymbol{\epsilon}}_2)\cdot e^{-i(\omega t-\mathbf{k}\cdot\mathbf{r})}\right], \tag{3.2}$$

where the unit vectors $\hat{\boldsymbol{\epsilon}}_{1,2}$ are orthonormal to the wave vector $\mathbf{k}$. The polarization state is completely described by the components of the Jones vector, $\mathbf{V} = (V_1, V_2)$. For linear polarization, the components $V_{1,2}$ are real, while for all other polarization states (for example circular polarization) they are complex. Considering now a fully polarized state, as the wave travels along its path, the electric field vector will span out an ellipse around the wave vector $\mathbf{k}$, shown in figure 3.4. Linear and circular polarization may be considered degenerate cases of this more general elliptical polarization state.

The parameters of the ellipse and the Jones vector are related [62]. The equations

$$a^2 + b^2 = |V_1|^2 + |V_2|^2 \tag{3.3}$$

$$ab = |V_1|\,|V_2|\,|\sin(\Delta\phi)|\,, \tag{3.4}$$

give the major (2a) and minor (2b) axes of the ellipse. Here, $\Delta\phi$ is the relative phase between V_1 and V_2. The equations

$$\tan(2\psi) = 2\frac{|V_1|\,|V_2|}{|V_1|^2 - |V_2|^2}\cos(\Delta\phi) \tag{3.5}$$

and

$$\sin(2\chi) = 2\frac{|V_1|\,|V_2|}{|V_1|^2 + |V_2|^2}\sin(\Delta\phi) \tag{3.6}$$

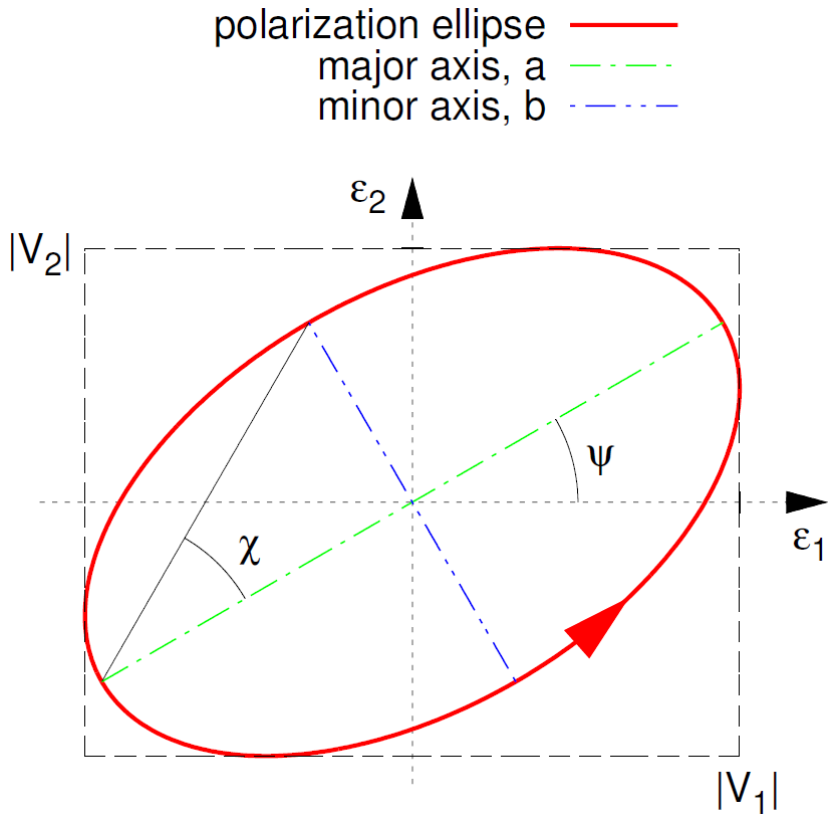

Figure 3.4: The Jones vector $\mathbf{V}$ of a polarized beam will in the most general case span out a polarization ellipse, here shown for $\psi = \chi = 30°$ [61].

define the angle ψ between the $\hat{\boldsymbol{\epsilon}}_1$ direction and the major axis and the angle of ellipticity χ respectively, where $0 \leq \psi \leq \pi$ and $-\frac{\pi}{4} \leq \chi \leq \frac{\pi}{4}$.

In the special case of a vanishing minor axis and angle of ellipticity, $b = 0$, $\chi = 0$, the beam is *linearly polarized*. The angle ψ then describes the angle of the linear polarization plane with a lab coordinate. The other interesting degenerate case is the case where the ellipse becomes a circle, i.e. $a = b$ and $|V_1| = |V_2|$. In this case the polarization angle ψ is undefined, and the beam is *circularly polarized*. By convention, the circular polarization is referred to as left-handed and right-handed when the electric field vectors rotate counterclockwise and clockwise, respectively, when looking into the source. However, this nomenclature for left- and right-handedness is not always consistent in the literature.

Poincaré-Stokes parameters

Rather than considering electric field vectors and their relative phases, for experiments it is usually more convenient to use the Poincaré-Stokes parameters, which completely describe the state of polarization of the beam. They are defined as

$$P_1 = \frac{|V_1|^2 - |V_1|^2}{|V_1|^2 + |V_1|^2} \tag{3.7}$$

$$P_2 = \frac{|V_1 + V_2|^2 - |V_1 - V_2|^2}{|V_1 + V_2|^2 + |V_1 - V_2|^2} = \frac{|V_1 + V_2|^2 - |V_1 - V_2|^2}{2\left(|V_1|^2 + |V_1|^2\right)} \tag{3.8}$$

$$P_3 = \frac{|V_1 - iV_2|^2 - |V_1 + iV_2|^2}{|V_1 + V_2|^2 + |V_1 - V_2|^2} = \frac{|V_1 - iV_2|^2 - |V_1 + iV_2|^2}{2\left(|V_1|^2 + |V_1|^2\right)}. \tag{3.9}$$

The state of linear polarization is fully described by P_1 and P_2, while P_3 quantifies the degree of circular polarization, where $P_3 = +1$ denotes left-handed circular polarization. The degree of linear polarization can be quantified as $P_{\text{lin}} = \sqrt{P_1^2 + P_2^2}$. For a fully polarized beam $\sqrt{P_1^2 + P_2^2 + P_3^2} = 1$. By comparing equations (3.5)-(3.6) and (3.7)-(3.9), one finds that $P_{1,2,3}$ are related to the polarization ellipse as follows (see figure 3.4):

$$P_1 = \cos(2\psi)\cos(2\chi) \tag{3.10}$$

$$P_2 = \sin(2\psi)\cos(2\chi) \tag{3.11}$$

$$P_3 = \sin(2\chi) \tag{3.12}$$

The physical interpretation of $P_{1,2,3}$ is that for a fully polarized beam, $P_1 = +1$ and $P_1 = -1$ refer to linear polarization along $\hat{\boldsymbol{\epsilon}}_1$ and $\hat{\boldsymbol{\epsilon}}_2$, respectively. P_2 likewise refers to polarization along unit vectors rotated 45° with respect to $\hat{\boldsymbol{\epsilon}}_{1,2}$. Any other values of the angle of linear polarization ψ will result in $P_{1,2}$ taking absolute values less than 1. Any nonzero value of the angle of ellipticity χ will introduce a nonzero P_3, and reduce the values of $P_{1,2}$ accordingly.

This formalism breaks down if the beam is only partially polarized, i.e. $\sqrt{P_1^2 + P_2^2 + P_3^2} < 1$, and one then has to describe the polarization state in terms of a density matrix [63, 64]. For the purposes of this thesis however, the above equations are sufficient.

3.2 Resonant Scattering

The absorption of x-rays by matter is highly dependent on photon energy. At the absorption edges of different elements, the absorption diverges as electrons are promoted from core levels into empty states above the Fermi level.

While performing x-ray scattering experiments, these absorbed photons are lost to fluorescence and incoherent scattering channels. However, close to the absorption edge the incident photon can induce virtual transitions between core levels and states above the Fermi level that relax back to the core states, emitting a photon with the same energy as the initial photon. Multipolar expansion of these virtual transitions yields additional terms in the x-ray scattering form factor that may enhance the signal [65]. For charge scattering, this is known as anomalous charge scattering and can be used to enhance the scattering contrast between elements. For magnetic scattering, the resonant enhancement of the signal is now known as x-ray resonant magnetic scattering (XRMS), resonant elastic x-ray scattering (REXS), or x-ray resonant diffraction (XRD).

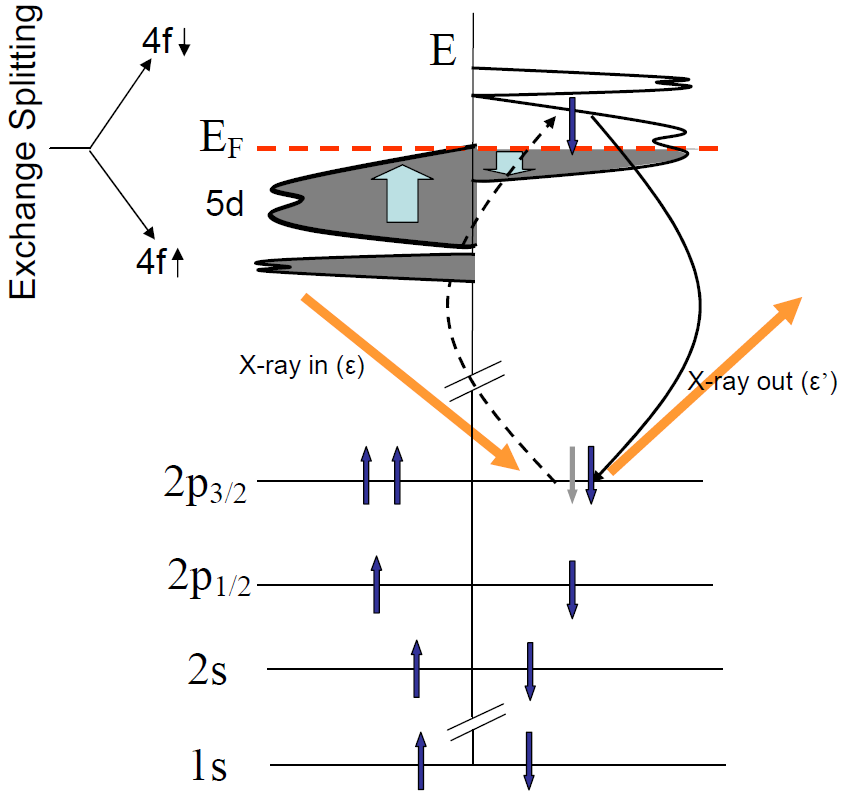

Figure 3.5: Schematic illustration of the second order perturbation process leading to XRMS as it occurs in lanthanide metals. $4f$ exchange splitting results in different transition matrix elements for the promotion of a core electron to empty states above the Fermi level, depending on the $4f$ spin polarization. The decay of the promoted electron back to the core level gives rise to an elastically scattered photon [66].

The x-ray scattering cross section for an electron in a quantized electromagnetic field was calculated using second order perturbation theory by Blume [67] and Blume and Gibbs [63], and was later simplified and expressed in the coordinate system relevant for XRMS experiments by Hill and McMorrow [64]. We will not go through the detailed derivations here, only present the final results.

For elastic scattering, the scattering cross-section can be written as

$$\frac{d\sigma}{d\omega} = r_0 \left| \sum_n e^{i\mathbf{Q}\cdot\mathbf{r_n}} f_n(\mathbf{k}, \mathbf{k}', \hbar\omega) \right|, \tag{3.13}$$

where $d\sigma$ is the differential cross-section of scattering into the solid angle $d\omega$, $r_0 = \frac{e^2}{mc^2}$ is the classical electron radius, $\mathbf{Q} = \mathbf{k}' - \mathbf{k}$ is the momentum transfer, $\mathbf{k}$ and $\mathbf{k}'$ are the incident and scattered wave-vectors of the photon and f_n is the scattering amplitude of the nth atom which is at the position $\mathbf{r_n}$. For coherent elastic scattering, the amplitude f can be written as a sum over the following terms [64]:

$$f = f_0 + f' + if'' + f_{\text{spin}}. \tag{3.14}$$

Here, f_0 is the Thomson charge scattering amplitude and f_{spin} is the non-resonant spin-dependent magnetic scattering amplitude. Far from resonance, f' and f'' contribute terms proportional to the orbital and spin angular momentum to the non-resonant scattering amplitude. At resonance both electric and magnetic multipole transitions contribute through the terms f' and f''. However, the electric dipole and quadrupole transitions are dominant with respect to magnetic multipole transitions by a factor of $\hbar\omega/mc^2$ (ca. 60 for typical x-ray absorption edges) [68]. Therefore, only electric multipole transitions will be considered here.

Considering only the electric 2^L-pole resonance in a magnetic ion, the resonant contribution to the coherent scattering amplitude can be written as [68]

$$f^e_{\text{EL}}(\omega) = \frac{4\pi}{k} f_D \sum_{M=-L}^{L} \left[\hat{\boldsymbol{\epsilon}}'^* \cdot Y^{(e)}_{LM}(\hat{\mathbf{k}}') Y^{(e)*}_{LM}(\hat{\mathbf{k}}) \cdot \hat{\boldsymbol{\epsilon}} \right] F^e_{\text{EL}}(\omega), \tag{3.15}$$

where $\hat{\boldsymbol{\epsilon}}$ and $\hat{\boldsymbol{\epsilon}}'$ are the incident and scattered polarization vectors, and $\hat{\mathbf{k}}$ and $\hat{\mathbf{k}}'$ are unit vectors along the incident and scattered wave vectors, respectively. $Y^{(e)}_{LM}(\hat{\mathbf{k}})$ are the vector spherical harmonics and f_D is the Debye-Waller factor. The strength of the resonance is determined by the factor $F^e_{\text{LM}}(\omega)$, which in

turn is determined by atomic properties:

$$F^e_{LM}(\omega) = \sum_{a,n} \frac{P_a P_a(n) \Gamma_x(\langle a|M|n\rangle; EL)}{2(E_n - E_a - \hbar\omega - i\Gamma/2)}. \tag{3.16}$$

Here, $|n\rangle$ is the excited state of the ion and $|a\rangle$ is the initial state. P_a is the probability of the ion existing in the initial state $|a\rangle$ and $P_a(n)$ is the probability for a transition from $|a\rangle$ to an excited state $|n\rangle$. Γ_x and Γ are the partial line widths of the excited state due to a pure 2^L-pole (EL) radiative decay and due to all processes, respectively. The transition from $|a\rangle$ to $|n\rangle$ is here an electric multipole (predominantly dipole (E1) and quadrupole (E2)) transition involving the virtual photo-excitation of an electron from a core level into an unoccupied state above the Fermi level. The subsequent de-excitation back to the core level results in the emittance of a photon with the same energy as the incident photon, which is seen in the experiments as an elastically scattered photon. The denominator of equation (3.16) ensures a resonant enhancement of the scattered intensity as the photon energy $\hbar\omega$ approaches the absorption edge ($E_n - E_a$).

Curiously enough, what we call resonant *magnetic* scattering results (in a large part) from *electric* multipole transitions. The sensitivity to the magnetic state in exchange split $4f$ and $5d$ bands comes about due to the difference in occupation of minority and majority spin states. This difference influences the strength of the resonant enhancement. In energy bands with high spin polarization, the resonant enhancement will in general be stronger. Also relevant for the resonant strength is the magnitude of the transition matrix element $\langle a|M|n\rangle$. For example, transitions from "s" core states to "p" or "d" excited states do not show large resonant enhancement because the overlap between their respective wave functions is small. The strength of the spin-orbit coupling in the ground and excited states, which is responsible for the electric multipole transitions, also influences the strength of the scattered signal [68, 69].

As a result of all these factors, the magnitude of the resonant enhancement will differ greatly between different elements and absorption edges. Table 3.1 categorizes the relevant edges and transitions in the materials with $3d$, $4f$ and $5f$ magnetism according to their resonant enhancement relative to the non-resonant magnetic scattering [66].

The electric dipole transitions (E1) usually dominate the resonant magnetic scattering cross section, and are also the simplest to calculate. Let us see what E1 contributes to the scattering amplitude in equation (3.15), following Hill and McMorrow [64]. For the electric dipole transition, the vector spherical harmonics in equation (3.15) can be written [70], for $L = 1$,

$M = \pm 1$:

$$\left[\hat{\boldsymbol{\epsilon}}'^{*} \cdot Y_{1\pm1}(\hat{\mathbf{k}}')Y_{1\pm1}(\hat{\mathbf{k}}) \cdot \hat{\boldsymbol{\epsilon}}\right] = \frac{3}{16\pi}\left[\hat{\boldsymbol{\epsilon}}' \cdot \hat{\boldsymbol{\epsilon}} \mp i(\hat{\boldsymbol{\epsilon}}' \times \hat{\boldsymbol{\epsilon}}) \cdot \hat{\mathbf{z}}_n - (\hat{\boldsymbol{\epsilon}}' \cdot \hat{\mathbf{z}}_n)(\hat{\boldsymbol{\epsilon}} \cdot \hat{\mathbf{z}}_n)\right]; \tag{3.17}$$

and, for $L = 1$, $M = 0$:

$$\left[\hat{\boldsymbol{\epsilon}}'^{*} \cdot Y_{10}(\hat{\mathbf{k}}')Y_{10}(\hat{\mathbf{k}}) \cdot \hat{\boldsymbol{\epsilon}}\right] = \frac{3}{8\pi}\left[(\hat{\boldsymbol{\epsilon}}' \cdot \hat{\mathbf{z}}_n)(\hat{\boldsymbol{\epsilon}} \cdot \hat{\mathbf{z}}_n)\right]; \tag{3.18}$$

$\hat{\mathbf{m}}_n$ is here a unit vector in the direction of the magnetic moment of the nth ion. We can therefore write the E1 contribution to the resonant scattering amplitude as

$$f_{nE1}^{\mathrm{XRES}} = \left[(\hat{\boldsymbol{\epsilon}}' \cdot \hat{\boldsymbol{\epsilon}})F^{(0)} - i(\hat{\boldsymbol{\epsilon}}' \times \hat{\boldsymbol{\epsilon}}) \cdot \hat{\mathbf{z}}_n F^{(1)} + (\hat{\boldsymbol{\epsilon}}' \cdot \hat{\mathbf{z}}_n)(\hat{\boldsymbol{\epsilon}} \cdot \hat{\mathbf{z}}_n)F^{(2)}\right] \tag{3.19}$$

where the $F^{(i)}$'s are linear combinations of the factor F_{LM} in equation (3.16)

Elements	Edge	Transition	Energy Range (keV)	Resonance Strength
$3d$	K	$1s \rightarrow 4p$ (E1) $1s \rightarrow 3d$ (E2)	$5 - 9$	Weak
$3d$	L_1	$2s \rightarrow 3d$ (E2)	$0.5 - 1.2$	Weak
$3d$	L_2,L_3	$2p \rightarrow 3d$ (E1)	$0.4 - 1.0$	Strong
$4d$	L_2,L_3	$2p \rightarrow 4d$ (E1)	$3.0 - 3.5$	Strong
$5d$	L_2,L_3	$2p \rightarrow 5d$ (E1)	$5.8 - 14.0$	Strong
$4f$	K	$1s \rightarrow 4p$ (E1)	$40 - 63$	Weak
$4f$	L_1	$2s \rightarrow 5d$ (E2)	$6.5 - 11.0$	Weak
$4f$	L_2,L_3	$2p \rightarrow 5d$ (E1) $2p \rightarrow 4f$ (E2)	$6.0 - 10.0$	Medium
$4f$	M_1	$3s \rightarrow 5p$ (E1)	$1.4 - 2.5$	Weak
$4f$	M_2,M_3	$3p \rightarrow 5d$ (E1) $3p \rightarrow 5f$ (E2)	$1.3 - 2.2$	Medium to strong
$4f$	M_4,M_5	$3d \rightarrow 4f$ (E1)	$0.9 - 1.6$	Strong
$5f$	M_4,M_2	$3d \rightarrow 5f$ (E1)	$3.3 - 3.9$	Strong

Table 3.1: Comparison of the magnitude of the resonant enhancement for the most common magnetic elements, where "weak" corresponds to a factor of about 10^0, "medium" to about 10^2 and "strong" to $> 10^3$ relative to the non-resonant magnetic scattering signal. After Ref. [66]

.

as follows:

$$F^{(0)} = \frac{3}{4k}(F_{11} + F_{1-1}) \tag{3.20}$$

$$F^{(1)} = \frac{3}{4k}(F_{11} - F_{1-1}) \tag{3.21}$$

$$F^{(2)} = \frac{3}{4k}(2F_{10} - F_{11} - F_{1-1}) \tag{3.22}$$

The magnitudes of these are determined by the atomic properties of the element in question, and have been evaluated for several rare earths and transition metals by Hamrick [71, 72]. The first term of equation (3.19) is not dependent on the magnetic moment and contributes only to the charge Bragg scattering, while the other two terms are sensitive to the magnetic structure.

For scattering experiments, it is useful to decompose the polarization and magnetic moment vectors into components relative to the scattering plane. The magnetic moment is decomposed into $z_{1,2,3}$ parallel to the unit vectors $u_{1,2,3}$ shown in figure 3.11. By convention, the polarization component parallel to the scattering plane is labeled π (for *parallel*) and the component perpendicular to the scattering plane is labeled σ (from German: *senkrecht*). Upon scattering, the polarization may be unchanged (σ-σ' or π-π' scattering) or swapped (σ-π' or π-σ' scattering). The most convenient way to express this is by way of a 2×2 matrix where the diagonal terms represent the scattering channels with unchanged polarization and the off-diagonal terms represent the corresponding polarization swapping channels, i.e.

$$f_{nE1}^{\mathrm{XRES}} = \begin{pmatrix} A_{\sigma\text{-}\sigma'} & A_{\pi\text{-}\sigma'} \\ A_{\sigma\text{-}\pi'} & A_{\pi\text{-}\pi'} \end{pmatrix}, \tag{3.23}$$

where $A_{\sigma\text{-}\sigma'}$ represents the scattering amplitude from incident σ polarized x-rays to scattered σ' polarized x-rays and so on.

A naïve inspection of equation (3.19) gives some hints on how the above matrix should look. Because of the dot product between the incident and scattered polarization state, the first term only couples scattered and incident photons with the same polarization, as expected for pure charge scattering. This produces a diagonal matrix. The second term involves a cross product projected onto the magnetic moment direction, and will therefore produce off-diagonal elements involving magnetic moment components in the scattering plane. The σ-σ' term will necessarily be zero, since the incident and scattered polarization states are parallel. Note that this is not the case for the π-π' term, since the incident and scattered polarization states here will differ by an angle 2θ, where θ is the Bragg angle. Since the cross product here produces a

vector perpendicular to the scattering plane, the projection onto the moment direction will probe the moment component perpendicular to the scattering plane. The third term is less intuitive as it is quadratic in the components of the magnetic moment, but it is straightforward to calculate. The end result is that the electric dipole contribution to the resonant scattering amplitude can be written, in components $z_{1,2,3}$ of the magnetic moment, as [64]

$$f_{nE1}^{\mathrm{XRES}} = F^{(0)} \begin{pmatrix} 1 & 0 \\ 0 & \cos 2\theta \end{pmatrix} - iF^{(1)} \begin{pmatrix} 0 & z_1 \cos\theta + z_3 \sin\theta \\ z_3 \sin\theta - z_1 \cos\theta & -z_2 \sin 2\theta \end{pmatrix} + F^{(2)} \begin{pmatrix} z_2^2 & -z_2(z_1 \sin\theta - z_3 \cos\theta) \\ z_2(z_1 \sin\theta + z_3 \cos\theta) & -\cos^2\theta(z_1^2 \tan^2\theta + z_3^2) \end{pmatrix}, \tag{3.24}$$

where z_3 is the moment direction antiparallel to the scattering vector, z_2 is the moment direction perpendicular to the scattering plane, and z_1 is perpendicular to the other two.

The first term of equation (3.24) contributes to the charge scattering, and allows for the polarization analysis by an analyzer crystal as described in section 3.3.3. The second term is linear in the components of the magnetic moment and therefore mainly responsible for producing first harmonic peaks at the magnetic wave vector $\boldsymbol{\tau}$. Measuring at such a magnetic peak allows for the determination of magnetic moment direction by comparing the different polarization channels. The σ-π' and π-σ' channels are sensitive to moment components in the scattering plane, and the π-π' channel measures the moment component perpendicular to the scattering plane. By measuring in several different scattering geometries, a comprehensive mapping of the moment direction is possible. The third term, which is quadratic in the components of the magnetic moment, produces second harmonic satellite peaks. However, the intensities of these are usually weak compared to the first harmonic satellites, and are in addition often obscured by the magnetically induced charge scattering described in section 3.2.3 [64]. The scattering amplitude also depends on the Bragg angle θ. Additional information may therefore be obtained by analyzing the magnetic peak intensities as a function of the scattering angle.

The resonant scattering amplitude for electric quadrupole transitions is much more complex and also not relevant for this thesis, so we will forgo a derivation here.

3.2.1 Non-resonant x-ray magnetic scattering

While the resonant scattering process offers some clear advantages for the study of magnetic materials, such as element specificity and larger scattering

amplitudes, XRMS experiments are not always possible, for example in the cases where the resonant process is not well understood or does not give a strong enough enhancement. In such cases, non-resonant x-ray magnetic scattering (NRXMS) may be of use. An additional advantage over XRMS is that NRXMS relies on the direct coupling of the x-ray photons to the magnetic moments, rather than an indirect resonant process. In contrast to XRMS, which is only sensitive to the direction **z** of the total magnetic moment, the scattering amplitude for NRXMS involves contributions from both spin **S** and orbital **L** angular momentum, and may as such in principle allow for determination of absolute magnetic moments or L/S ratios [73, 74]. Far from resonance, the three last terms of equation (3.14) all contribute to the total non-resonant magnetic scattering amplitude, which can be written as [67, 63]:

$$f_n^{NRXMS}(\mathbf{Q}) = -i\frac{\hbar\omega}{mc^2}\langle M_m\rangle \tag{3.25}$$

$$= -i\frac{\hbar\omega}{mc^2}\left[\frac{1}{2}\mathbf{L}_n(\mathbf{Q})\cdot\mathbf{A} + \mathbf{S}_n(\mathbf{Q})\cdot\mathbf{B}\right] \tag{3.26}$$

where $\mathbf{L}_n(\mathbf{Q})$ and $\mathbf{S}_n(\mathbf{Q})$ are Fourier transforms of the orbital and spin magnetization densities, respectively. The notation $\langle\ \rangle$ represents the ground state expectation value of the operators. **A** and **B** are vectors containing different polarization and **Q** dependencies, allowing for an NRXMS experiment to distinguish between the orbital and spin components of the magnetic moment, in contrast to both XRMS and neutron magnetic scattering. Expressing $\langle M_m\rangle$ in a polarization dependent basis like in equation (3.23), this becomes evident:

$$\langle M_m\rangle = \begin{pmatrix} S_2\sin 2\theta & -2(\sin^2\theta)\left[(L_1+S_1)\cos\theta - S_3\sin\theta\right] \\ 2(\sin^2\theta)\left[(L_1+S_1)\cos\theta + S_3\sin\theta\right] & (\sin 2\theta)\left[2L_2\sin^2\theta + S_2\right] \end{pmatrix} \tag{3.27}$$

It is worth noting that the σ-σ' channel is independent of orbital magnetization densities. Information about the spin and orbital magnetizations may therefore be obtained by comparing the intensities in the σ-σ' and π-π' channels. Like for resonant scattering, the different polarization channels are sensitive to different moment directions. Here, the diagonal elements are sensitive to the magnetization perpendicular to the scattering plane, while the off-diagonal polarization channels probe the magnetization within the scattering plane.

An interesting special case of the NRXMS scattering amplitude is when the scattering angle becomes very small, i.e. $\theta << 1$. For reflections with small $\mathbf{Q}$, this condition may be fulfilled by using very high photon energies, since Bragg's law tells us that the scattering angle is proportional to the photon wavelength. Because of the factor $\sin^2\theta$, the off-diagonal terms of equation (3.27) go towards zero much faster than the diagonal terms as θ approaches zero. For very high photon energies, $\langle M_m \rangle$ therefore takes the very simple form [75, 76]

$$\langle M_m \rangle = \sin 2\theta \begin{pmatrix} S_2 & 0 \\ 0 & S_2. \end{pmatrix} \tag{3.28}$$

In other words, the magnetic scattering cross section is in this case only sensitive to the spin component perpendicular to the scattering plane. Furthermore, polarization analysis is not required, since both diagonal terms are identical. Owing to this simple magnetic cross-section, high energy x-ray magnetic scattering (HEXMS) has been used successfully to determine spin directions in MnF_2 [75]. HEXMS also benefits from a volume enhancement of the signal since the beam penetrates the sample and scatters from the entire bulk. Despite this enhancement though, the NRXMS signal is still very weak, typically 6 orders of magnitude weaker than the charge scattering [67]. However, the high brilliance of modern synchrotron radiation sources allows for measurements of the very weak NRXMS signal within a reasonable experimental time frame.

3.2.2 The Structure Factor

The scattering amplitude in equation (3.24) gives us the probability of a dipole resonant process yielding a scattered photon from a single ion. However, when doing scattering experiments, we measure the scattered intensity from an ensemble of ions organized in a crystal structure. The intensity I_m of a magnetic reflection is then proportional to the squared modulus of the magnetic structure factor F_m:

$$I_m \propto |F_m|^2 \tag{3.29}$$

The magnetic structure factor F_m for a reflection at the (hkl) position in reciprocal space can be written as [66]

$$F_m = \sum_j f_j e^{2\pi i(hx_j + ky_j + lz_j)} \tag{3.30}$$

where the summation is over all the magnetic atoms in the magnetic unit cell and f_j is the magnetic scattering amplitude, which for resonant electric dipole scattering is given by equation (3.24), and for NRXMS by equation (3.27). The coordinates x_j, y_j, z_j gives the location of the jth ion inside the magnetic unit cell. While measuring a first harmonic resonant dipole reflection, $f_j \propto \mathbf{k}_i \cdot \boldsymbol{\mu}$, where $\mathbf{k}_i$ is the wave vector of the incoming photons and $\boldsymbol{\mu}$ is the magnetic moment, such that

$$I_m \propto \mu^2 \tag{3.31}$$

3.2.3 Magnetically induced charge scattering

While the resonant magnetic cross-section provides direct information about moment directions and magnitudes in the crystal, additional indirect information may sometimes be available by studying diffraction intensity from magnetically induced charge scattering. These reflections originate from magnetoelastic distortions of the crystal lattice. For example, a long-period magnetic modulation wave vector $\boldsymbol{\tau}$ will often induce a lattice modulation of $2\boldsymbol{\tau}$, due to the symmetric exchange interaction that we visited in equation (2.7).

Following Lovesey and Collins [77], we consider a one-dimensional string of atoms along the x direction of the crystal lattice. The position of the nth atom along the string may be written

$$x_n = na, \tag{3.32}$$

where a is the interatomic distance. If there is a weak long-period modulation to the atomic positions, the perturbed positions become

$$x_n = na + D(x) \tag{3.33}$$

where the period of the displacement wave $D(x)$ is much larger than a, and the amplitude is much smaller. If we assume that the string of atoms can be modeled as a classical spring with an atomic spring constant K, this displacement will induce a force on the nth atom which will compete with the symmetric exchange interaction between neighboring magnetic moments. The magnetic exchange constant $J(d)$ is highly dependent on the atomic separation d, so we can assume that the dominant contribution to this competing force arises from the variation in the exchange constant with d. The equilibrium condition balancing these two forces then becomes [77]

$$Ka^2 \frac{\partial^2 D(x)}{\partial x^2} = \frac{\partial J(d)}{\partial d}(\boldsymbol{\mu}_{n-1} \cdot \boldsymbol{\mu}_n - \boldsymbol{\mu}_n \cdot \boldsymbol{\mu}_{n+1}) \tag{3.34}$$

where $\boldsymbol{\mu}_n$ is the thermal average value of the magnetic moment on the nth atom.

Using this we may calculate the amplitude and period of the atomic displacement wave $D(x)$ for some simple magnetic structures. In a magnetic helix with wave vector $\boldsymbol{\tau}_m = \tau_m \hat{\mathbf{x}}$ the magnetic moment directions as function of x may be written

$$\boldsymbol{\mu}_n = \mu[\hat{\mathbf{y}} \sin(\tau_m x) + \hat{\mathbf{z}} \cos(\tau_m x)]. \tag{3.35}$$

Such a magnetic structure is found for instance in Ho metal. In this case,

$$\boldsymbol{\mu}_{n\pm1} = \boldsymbol{\mu}_n \cos(\tau_m a) \pm \mu \left[\hat{\mathbf{y}} \cos(\tau_m x) - \hat{\mathbf{z}} \sin(\tau_m x)\right] \sin(\tau_m a) \tag{3.36}$$

and

$$\boldsymbol{\mu}_{n-1} \cdot \boldsymbol{\mu}_n = \boldsymbol{\mu}_n \cdot \boldsymbol{\mu}_{n+1} = \mu^2 \cos(\tau_m a). \tag{3.37}$$

Inserting this into equation (3.34), we see that for the magnetic helix, $D''(x) = 0$ and there is no displacement modulation wave. This is because the angle and distance between adjacent moments in the helix are constant, so that the forces balance without a modulated deformation.

A more interesting example is the transverse magnetic modulation, such as the one found in the paraelectric phases of $R\mathrm{MnO_3}$, which may be expressed as

$$\boldsymbol{\mu}_n = \mu \hat{\mathbf{z}} \sin(\tau_m x). \tag{3.38}$$

The moments on adjacent atoms are then

$$\boldsymbol{\mu}_{n\pm1} = \boldsymbol{\mu}_n \cos(\tau_m x) \pm \mu \hat{\mathbf{z}} \cos(\tau_m x) \sin(\tau_m a) \tag{3.39}$$

and the equilibrium condition (3.34) becomes

$$KaD''(x) = -J'(d)\mu^2 \sin(\tau_m a) \sin(2\tau_m x). \tag{3.40}$$

A solution of this solved for $D(x)$, apart from constant and linear terms, is

$$D(x) = \frac{J'(d)\mu^2 \sin(\tau_m a)}{4K\tau_m^2 a^2} \sin(2\tau_m x). \tag{3.41}$$

For long-period modulations ($\tau_m a << 1$), this reduces to

$$D(x) = \frac{J'(d)\mu^2}{4K\tau_m a} \sin(2\tau_m x). \tag{3.42}$$

The symmetric exchange interaction therefore induces a displacement wave with half the period of the magnetic structure, or twice the wave vector, i.e. $\tau_d = 2\tau_m$. The amplitude is determined by $J'(d)$, a and the square of the magnetic moment μ.

The scattered intensity from such a modulated structure is proportional to the square of the unit cell structure factor, $I \propto |F_c(Q)|^2$, where

$$F_c(Q) = \sum_j f_j^c e^{i\mathbf{Q}\cdot\mathbf{R}_j} = \sum_j f_j^c e^{-iQx_j} \tag{3.43}$$

is the structure factor for charge scattering. f_j^c is here the atomic scattering length of the jth atom in the unit cell, whose value can be looked up in the International Tables for Crystallography [78]. If the atomic positions projected along $\hat{\mathbf{x}}$ are periodic ($x_n = an$), the diffraction intensities are zero unless $\mathbf{Q}$ is a normal Bragg reflection. If we now add on the displacement wave (3.42), ($x_n = an + D(x)$), it can be shown that a pair of satellite peaks surrounding each main reflection will arise, $\mathbf{Q} = \mathbf{Q}_{\text{Bragg}} \pm \boldsymbol{\tau}_d$, whose intensities will scale with the square of the displacement wave amplitude [77]. Since the amplitude scales with the square of the magnetic moment (cf. equation (3.42)), this gives

$$I_{\boldsymbol{\tau}_d} \propto \mu^4 \tag{3.44}$$

This is in contrast to the resonant magnetic diffraction intensities, which scale with μ^2. The magnetically induced charge scattering is thus much more sensitive to rapid changes in the magnetic moment, for example close to phase transitions. It can therefore provide additional insight into the magnetic behavior of materials, especially if the magnetic diffraction peaks are very weak.

3.3 Beamline P09

The majority of the experimental results in this thesis were obtained at the Resonant Scattering and Diffraction Beamline P09 at the PETRA III storage ring at Deutsches Elektronen-Synchrotron DESY [79]. P09 was one of the very first beamlines being commissioned after the completion of the PETRA III synchrotron source. It is optimized for resonant and non-resonant scattering and diffraction studies on hard condensed matter in the tender to hard x-ray range (2.7 to 24 keV). These experiments are performed on two diffractometers located in two different experimental hutches (P09-EH1 and P09-EH2), dedicated to different sample environments (see Figure 3.6). The beamline is shared with a hard x-ray photoelectron spectroscopy station (HAXPES) located in a third experimental hutch (P09-EH3).

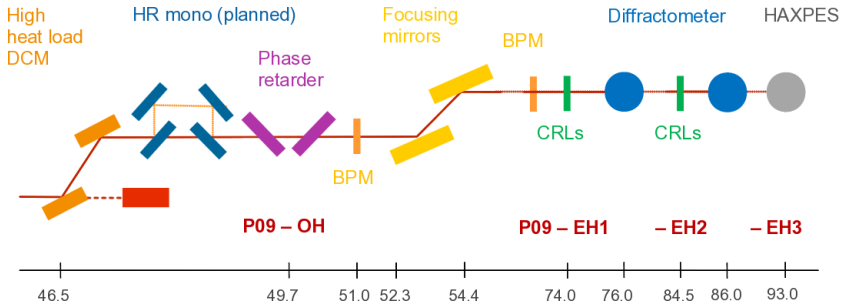

Figure 3.6: Schematic of the P09 beamline, as viewed from the side. The scale on the bottom denotes the distance in meters from the undulator source. The monochromatic beam is selected by the monochromator (DCM) on the left, while the white beam passes through to the beamstop (BS). There is space available for installing an additional high-resolution monochromator. The double phase retarder setup and focusing mirrors are also located in the optics hutch (P09-OH) [79].

3.3.1 Storage ring and undulator

PETRA III is a third generation synchrotron radiation source with a long history behind it. It was originally built as the electron-positron collider PETRA (or Positron-Electron Tandem Ring Accelerator) and was in operation as such from 1978 to 1986. It was here that the first direct evidence for gluons in three jet events was observed by the TASSO and JADE collaborations [80, 81]. Later, as PETRA II, it was used as a pre-accelerator for the HERA lepton-proton collider, and also parasitically as an x-ray source. Since 2009, it has been in operation as a dedicated 3rd generation synchrotron radiation source under the name PETRA III.

PETRA III being a refurbished particle collider is the reason for the very large circumference (2.3 km) compared to other third generation synchrotron radiation sources. This large circumference facilitates a very low horizontal emittance[1] of 1 nm rad, which translates directly into reduced divergence and horizontal photon source size in addition to a high brilliance. The large circumference and radius of curvature also means that there is no room for bending magnet beamlines at PETRA III. All beamlines are hence outfitted with undulators located in nine straight sections corresponding to nine sectors in the experimental hall covering one-eighth of the ring circumference.

P09 shares sector 6 of the experimental hall with beamline P08, the High-

[1]The emittance of a particle beam is a measure of the average spread of particle coordinates in position and momentum phase space. In a low emittance beam, the particles are confined to a small distance and have nearly the same momentum.

Resolution Diffraction beamline [82]. P09 uses its own 2 m U32 spectroscopy undulator, which can generate a continuous photon energy spectrum by scanning the undulator gap. The lowest gap size of 9.8 mm allows for a minimum energy of 2.7 keV.

3.3.2 Beamline optics

Monochromator

The x-ray radiation from the undulator is distributed across a certain energy bandwidth. In addition, there is a low energy halo around the central radiation cone. This halo is cut off by water-cooled slit before the beam passes into the optics hutch. In order to reduce the bandwidth and hence increase the energy resolution, the beam is passed through a high-heat-load double-crystal fixed-exit monochromator located in the optics hutch. The monochromator operates by scattering from Silicon crystals according to Bragg's law for selecting a narrow energy range. Two pairs of crystals, Si(111) and Si(311) are available, and may be interchanged by translating the whole monochromator tank perpendicular to the beam path. The Si(311) crystal pair has a higher energy resolution compared to the Si(111) at the expense of a factor of five in photon flux. The crystals are cooled with liquid N_2 to counteract the beam heating due to the high photon flux from the undulator. LN_2 suits itself well to this purpose, since the temperature dependent linear thermal expansion coefficient of Si is flat around LN_2 temperatures.

The photon energy of the beam is chosen by setting the correct undulator gap and adjusting the diffraction angle of the monochromator crystals to satisfy the Bragg condition for the desired energy. To ensure that the beam exits the monochromator at the same height for all photon energies, the second crystal is translated horizontally according to the diffraction angle. This procedure can be done automatically by the beamline operating software. After diffracting off both crystals, the beam exits the monochromator tank with a vertical offset of 21 mm.

Phase retarder

The beam produced by the undulator is highly linearly polarized in the horizontal direction. This is desirable for many experiments, but some experiments also require linearly polarized light in other directions and also circularly polarized light. For the purpose of changing the polarization state of the beam, a double phase retarder setup is available in the optics hutch downstream from the monochromator.

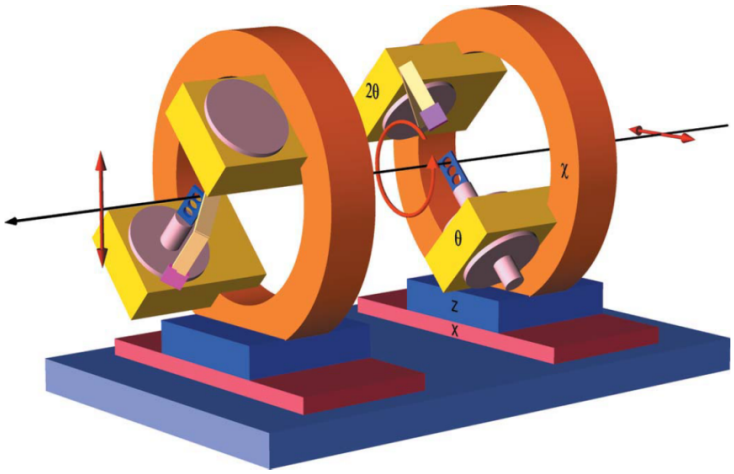

Figure 3.7: Schematic drawing of the phase retarder setup with the phase plates set up in the 90° geometry. The beam coming from the left with horizontal linear polarization is transformed into a circularly polarized beam by the first phase plate. The second phase plate then changes the circular polarization state to vertical linear polarization [79].

In classical optics, linearly polarized light is transformed into circularly polarized and rotated linearly polarized light by quarter-wave plates (QWP) and half-wave plates (HWP), respectively. They act by shifting, or *retarding*, the relative phase $\Delta\phi$ between the Jones vector components $V_{1,2}$, cf. equations (3.4)-(3.6). In the hard x-ray regime, QWP and HWP conditions can be realized using perfect crystals [83]. By slightly detuning the crystals from the ideal Bragg condition in transmission geometry, a phase shift is introduced which depends on the deviation angle from the Bragg angle. Figure 3.8 shows the measured and calculated deviation angles for the QWP condition for a 400 μm phase-plate as a function of photon energy.

A half-wave plate can be realized by using two quarter-wave plates in series, i.e. transforming linear polarization into circular polarization and then transforming it back to linear polarization with the desired polarization angle. Although the overall intensity is reduced using two plates instead of one, this has a couple of advantages over using just a single HWP. For one, the amount of unpolarized x-rays is reduced because the deviation angle required for QWP condition is further away from the Bragg angle of the crystal than that for HWP condition. Furthermore, the phase-shift changes more slowly at QWP condition than at HWP condition, with the result that the phase-shift spread due to beam divergence is reduced and depolarization effects are minimized.

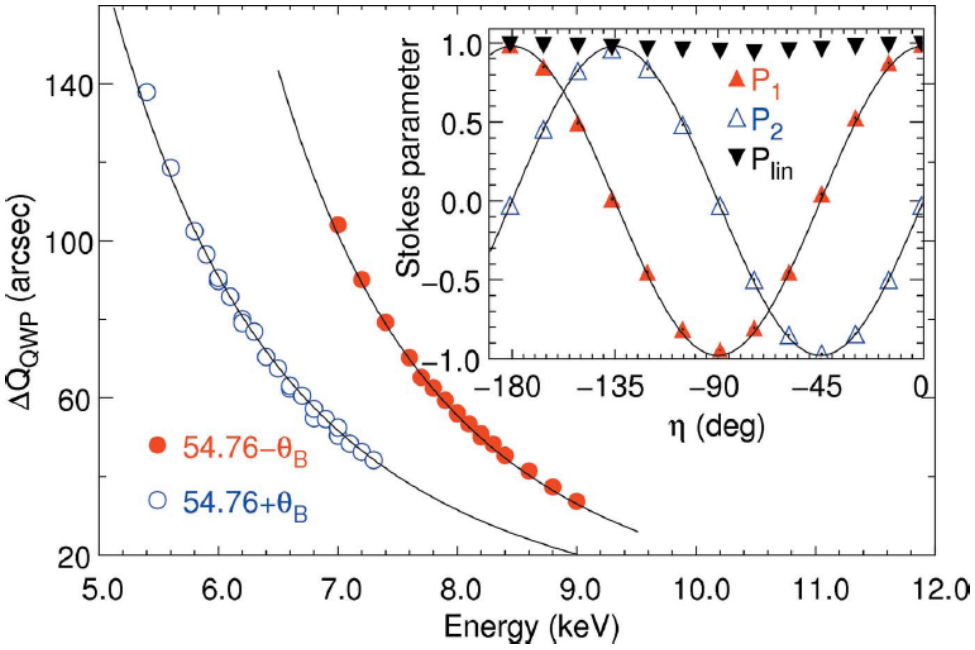

Figure 3.8: Calculated (curves) and measured (circles) deviation angles in both directions from the perfect Bragg condition required for setting a 400μm diamond phase plate in the QWP condition, as function of photon energy. The inset shows measured and calculated values of $P_{1,2}$ as function of the linear polarization angle η, as well as the degree of linear polarization P_{lin} [79, 84].

Figure 3.7 shows a schematic drawing of the double phase retarder setup at P09. The two phase plates are mounted in separate Eulerian cradles with x- and z-translations to align them in the beam. The QWP and HWP conditions are obtained by aligning the angles θ close to the Bragg condition. The beam polarization angle η is chosen by rotating the phase plate with an angle χ. A full rotation of η from 0 to -180° is possible by either rotating one phase plate in HWP condition, keeping both phase plate in QWP condition and rotating one of them, or by rotating both QWPs such that $\chi_2 = \chi_1 - 90°$. Tests have shown that the last configuration produces the highest degree of linear polarization at P09. This is because it allows compensation for depolarizing effects due to the energy spread, which is non-negligible at P09 [85]. Depolarizing effects due to beam divergence are however negligible, due to the low emittance of the PETRA III storage ring. The resulting polarization angle is $\eta = 2(\chi_1 - 90°) = 2\chi_2$. The red arrows in figure 3.7 shows an example of how the polarization changes going through the phase retarder setup from right to left with the first QWP at $\chi_1 = 45°$ and the second QWP

at $\chi_2 = -45°$. The inset of figure 3.8 shows the measured variation of the Stokes parameters of the polarized beam during one such polarization scan. The degree of linear polarization P_{lin} is $96.8 \pm 1.7\%$ on average [79].

Mirrors

For the purposes of focusing the beam and the suppression of higher harmonics, the beam is next vertically reflected off two SiO_2 mirrors. The first mirror (Pilz-Optics) is divided into four parts: two carved cylinders for horizontal focusing with a flat section in between, where half of the flat section and one cylinder are coated with 40 nm palladium. The second mirror (SESO) has one cylinder in the the middle and two flat sections on the sides, where one flat section is palladium coated. In addition, to enable vertical beam focusing, the second mirror is equipped with a bender. By combining different combinations of mirrors it is possible to efficiently suppress higher harmonics in the energy range from 6 to 24 keV in EH1 and 7 to 32 keV in EH2. At the sample position in EH1, the beam size after mirror-focusing is $150 \times 30\mu$m (FWHM).

Compound refractive lenses and absorber

If a smaller beam size is desirable, a movable lens changer (transfocator) is available. It can be mounted on the experimental table in either EH1 or EH2 at approximately 1.9 m in front of the sample position. The lens changer contains eight assemblies of compound refractive lenses (CRLs) varying in number and radius of curvature, which can be inserted into the beam using pneumatic actuators. After aligning it parallel to the beam, it can be translated by ± 150 mm along the beam for fine-tuning of the focal point. The mirrors are used to pre-focus the beam so that it fits through the 0.9 mm aperture of the CRLs. After refocusing using the CRLs, focal sizes at the sample position of $50 \times 4\mu$m (FWHM) have been achieved.

While the high photon flux at PETRA III is desirable, it can sometimes be damaging for detectors placed directly in the beam path or at strong Bragg reflections. In addition, for experiments at low temperature, beam heating may affect the sample temperature considerably. For these situations, the beam can be attenuated by inserting a combination 12 different foil assemblies into the beam using a device similar to the one used for the CRLs. Like this, the beam can be controllably attenuated up to at least ten orders of magnitude in the entire energy range of 2.7-30 keV. In addition, in-beam components such as phase retarders and CRLs will also attenuate the beam by different amounts depending on the photon energy.

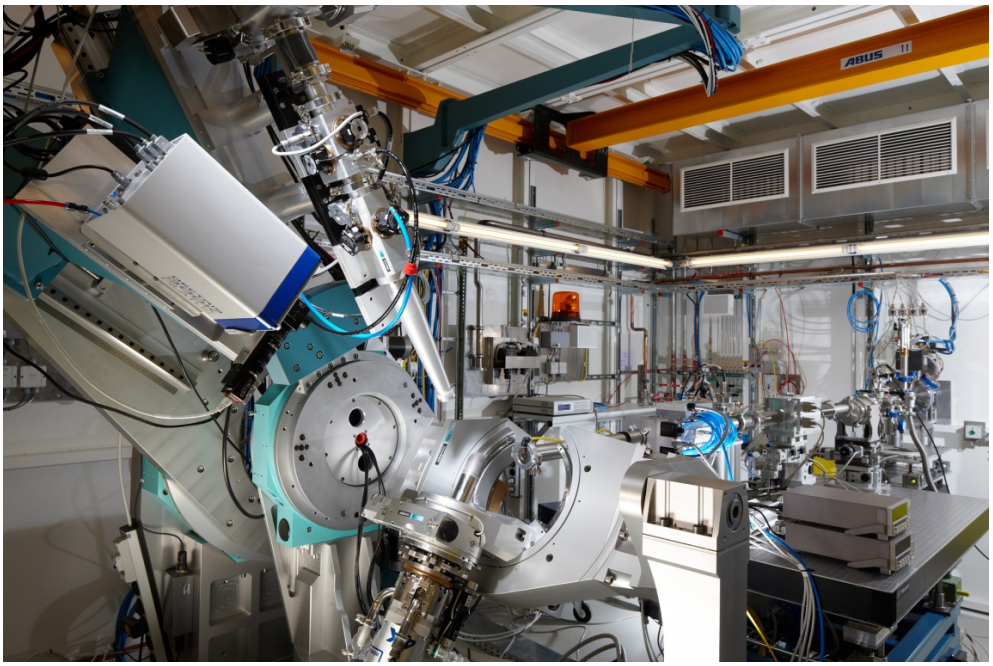

Figure 3.9: Experimental Hutch 1 at P09, with the 6-circle diffractometer. The ARS DE-202SG cryostat is mounted at the sample position. On the experimental table one can see the absorber and CRL exchanger boxes [79].

3.3.3 First experimental hutch (EH1)

All the optical components in the optics hutch are mounted in vacuum tanks sharing the vacuum with the synchrotron ring. At the entrance to the first experimental hutch, mounted on a granite table, is the first window separating the ring vacuum from the beamline vacuum. It consists of a 20 μm diamond plate with an opening of 3 mm. Before reaching this window, the beam passes through a slit system used to define the beam, also mounted on the granite table. Downstream from this, an experimental table is located, where various optical elements may be mounted, such as the attenuator and CRL transfocators and an out-of-vacuum phase retarder setup for use at higher photon energies.

The main instrument in EH1 is the six-circle diffractometer pictured in figure 3.9 (Huber Diffraktionstechnik). It is equipped with four motorized circles for the sample (θ (vertical), χ, ϕ, μ (horizontal θ)) and two for the detector arm (δ (vertical 2θ), γ (horizontal 2θ)), following the conventions laid out by Busing and Levy [86]. The χ-circle has an opening at the top to allow for large scattering angles. The diffractometer may be operated in both vertical and horizontal scattering geometry. It is operated via the diffractometer

Tango device that calculates motor positions from reciprocal space positions and vice versa, using a **UB** matrix [86]. In addition to the six motorized circles, several virtual motors are available for more complex movements, such as ψ rotations (rotations of the sample around the scattering vector) and reciprocal space scans (scans along h, k, l or another arbitrary direction in reciprocal space).

The sample stage is equipped with x-, y- and z-translation motors for aligning the sample in the beam. At the sample position, different sample environments may be mounted, such as cryostats, ovens or small electromagnets. All experiments in this thesis were performed using two different cryostats for cooling the sample: a 4 to 450 K ARS DE-202SG cryocooler which has a base temperature at the sample position of 8 K; and a 1.7 to 300 K ARS DE-302 cryocooler. The latter is equipped with a Joule-Thomson stage for lowering the temperature at the cold head to 1.7 K from the boiling point of helium, resulting in a 3 K base temperature at the sample position. In practice, the actual temperature where the beam hits the sample will be a bit higher due to beam heating, unless the beam is attenuated by some orders of magnitude.

On the detector arm, two in-vacuum slit systems are situated in front of the detector for collimation of the diffracted beam. The APD point detector may either be mounted directly behind these slits, or behind the polarization analyzer stage also mounted on the detector arm. The analyzer stage is connected to the slit system using a double O-ring coupling to allow an in-vacuum rotation of the entire analyzer stage around the scattered beam axis (η' rotation). In sum, the entire beam path, starting at the diamond window at the entrance to EH1 going via the sample position to the detector, is completely in vacuum, apart from a few centimeters of air around the Be dome of the cryostat.

The polarization analysis is performed using an analyzer crystal mounted with the analyzer Bragg angle of $\theta_{\mathrm{pol}} = 45 \pm 5^\circ$ towards the diffracted beam. For charge Bragg scattering, if the beam is polarized parallel to the analyzer scattering plane, the intensity is modified by a factor $\cos^2 2\theta_{\mathrm{pol}}$ (cf. equation (3.24)). Therefore, by choosing a crystal that scatters at the scattering angle $2\theta_{\mathrm{pol}} = 90^\circ$, the crystal will act as a polarization filter that only scatters photons with polarization perpendicular to the analyzer scattering plane. In practice, this condition is hard to fulfill except at very specific photon energies. Nevertheless, by choosing a crystal facet with the appropriate lattice spacing for the current photon energy, scattering very close to 90° is achievable. In this case, there will be a small contamination from other polarization components, which is called leakage. At P09, a selection of exchangeable analyzer crystals covering the energy range from 2.7 keV up to 13 keV are

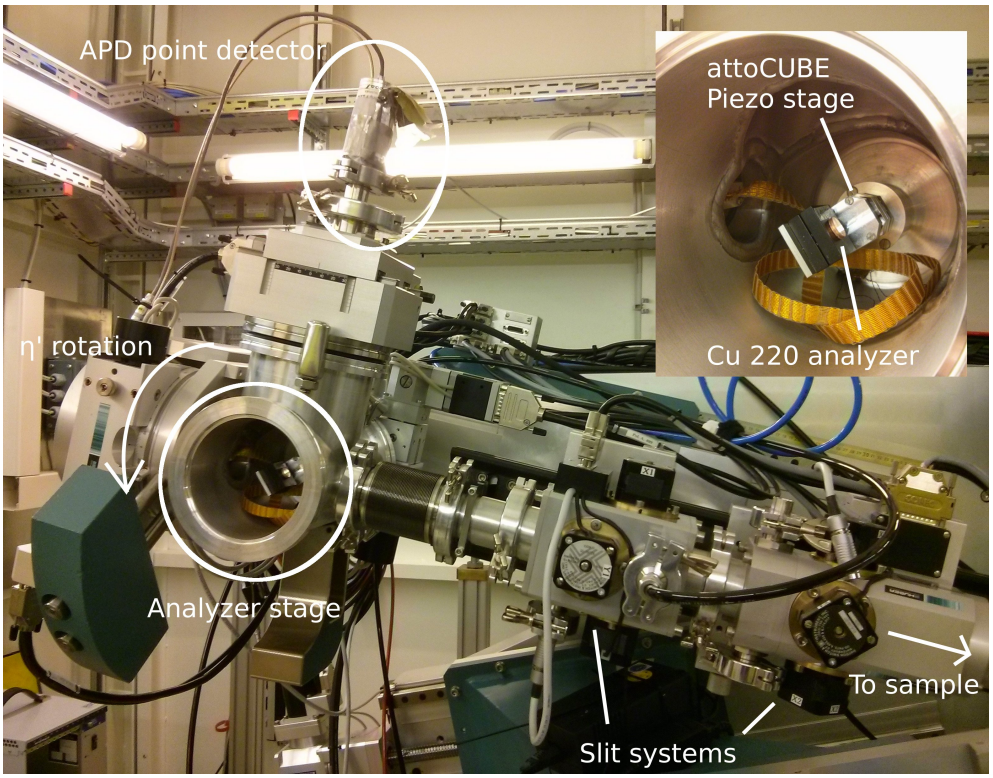

Figure 3.10: Closeup view of the detector arm in EH1. The scattered beam from the sample passes through two in-vacuum slit systems for beam collimation, before being scattered at close to 90° towards the detector by the crystal polarization analyzer. Precise positioning and alignment of the analyzer is done using piezo actuators, pictured in the inset. For measurements at the Mn K edge, the (220) reflection from Cu was used for polarization analysis.

available. In the experiments presented here, a Cu (220) analyzer was used for measurements at the Mn K and Eu L_3 edges, and the (006) reflection from pyrolithic graphite was used for polarization analysis at the Eu L_2 edge.

Figure 3.11 shows a schematic view of the vertical scattering geometry thus achieved for a typical magnetic scattering experiment. The beam coming from the undulator is highly polarized in the horizontal plane, and may be rotated by an arbitrary angle η by the phase retarder. Upon scattering from a magnetic moment with direction $\mathbf{z}$, the polarization state of an x-ray photon will be modified as described in the next section. The polarization state of the scattered beam may then be analyzed by scanning the analyzer angle η' and using equation (6.1).

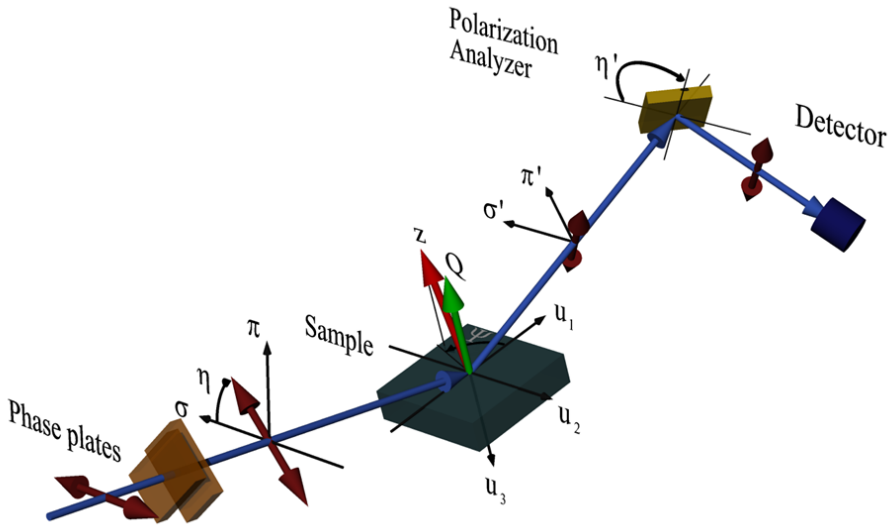

Figure 3.11: Schematic view of the vertical scattering geometry. For vertical scattering geometry, the x-ray radiation exits the undulator with σ polarization, where σ (σ') and π (π') denote polarization directions of the incident (scattered) beam perpendicular and parallel to the scattering plane, respectively [64]. After passing through the phase plates, the polarization direction is rotated by an angle η. At the sample is shown the uniaxial vector $\mathbf{z}$, which during azimuthal scans rotates around the scattering vector $\mathbf{Q}$ by an angle Ψ. The reference vectors $\mathbf{u}_{1,2,3}$ define a coordinate system for the sample. Polarization analysis is performed by rotating the polarization analyzer by an angle η' about the scattered beam [79].

3.3.4 Second experimental hutch (EH2)

In the second experimental hutch, the main instrument is a non-magnetic heavy-load six-circle diffractometer (Huber Diffraktionstechnik). It is more limited in range than the diffractometer in EH1, but is in turn capable of carrying a load of up to 650 kg. The detector arm is outfitted with two slit systems and an analyzer stage identical to the setup in EH1.

Most of the hard x-ray experiments in magnetic field presented in this thesis were performed in EH2, using the vertical-field 14 T split-coil superconducting magnet (Cryogenic Ltd.) available at P09. Figure 3.12 shows the 14 T magnet mounted on the heavy-load diffractometer, with an inset showing the window distribution. In horizontal scattering geometry, by combining the θ and ϕ angles together with the rotation of the sample rod within the cryostat, scattering angles up to 170° can be reached, with no dark angles.

The magnet is equipped with a variable-temperature insert (VTI) providing temperatures in the range 1.8 to 300 K in normal operation. The lowest temperatures are achieved by evaporative cooling with liquid ^{4}He let into the sample space trough a needle valve from the reservoir used to cool the superconducting coils. Using a pump to stabilize the vapor pressure at 5 - 10 mBar, 1.8 K is reached at the sample position (see figure 3.13). Even lower temperatures are attainable using a ^{3}He insert. Because the latent heat of ^{3}He is lower than that of ^{4}He, it is possible, through the method of evaporative cooling, to bring the temperature down further compared to evaporative

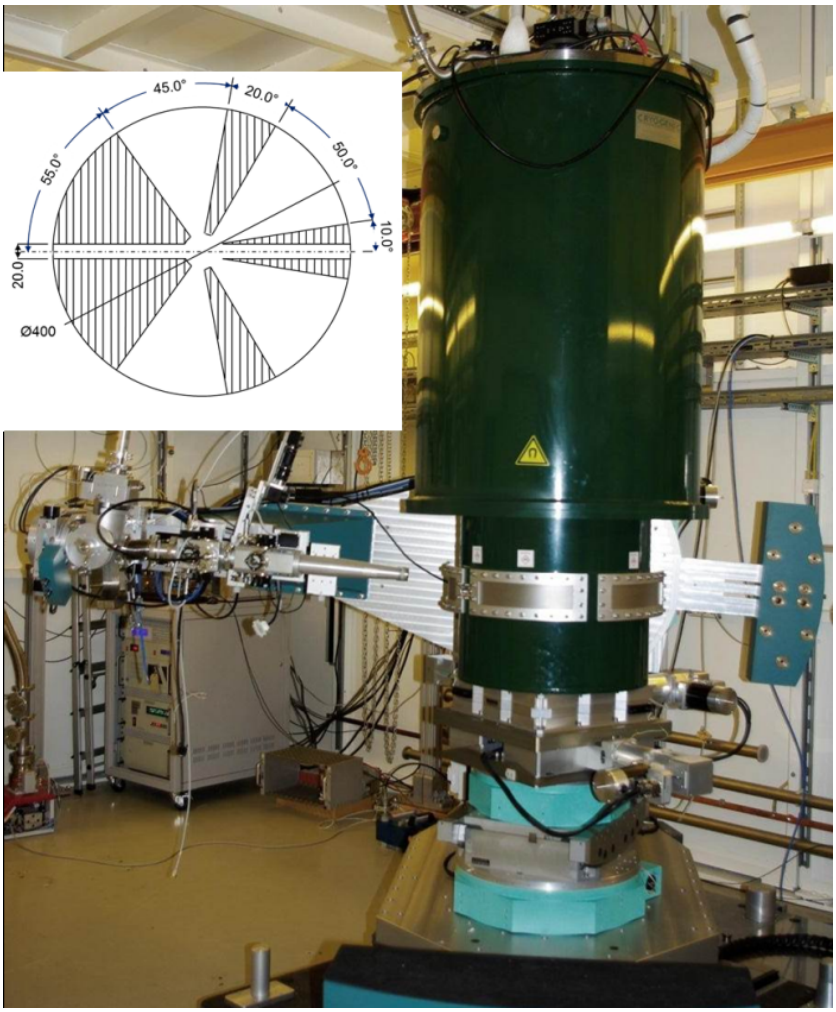

Figure 3.12: 14 T magnet mounted on the heavy-load diffractometer in EH2. The inset shows a top view of the window distribution around the magnet [79].

cooling of ^{4}He. Figure 3.13 shows how the vapor pressure of ^{3}He and ^{4}He decreases exponentially with temperature. By pumping, it is in principle possible to achieve temperatures of about 260 mK for ^{3}He compared to 1 K for ^{4}He. In reality, thermal contact with the surroundings, such as the temperature sensor and the heater wiring, will increase the measured base temperature to 360 mK. With the additional heat load from the x-ray beam, it is possible to stabilize the temperature with good accuracy at < 800 mK, but it is nonetheless imperative to attenuate the beam at least 3 orders of magnitude to ensure stable measuring conditions over an extended period of time.

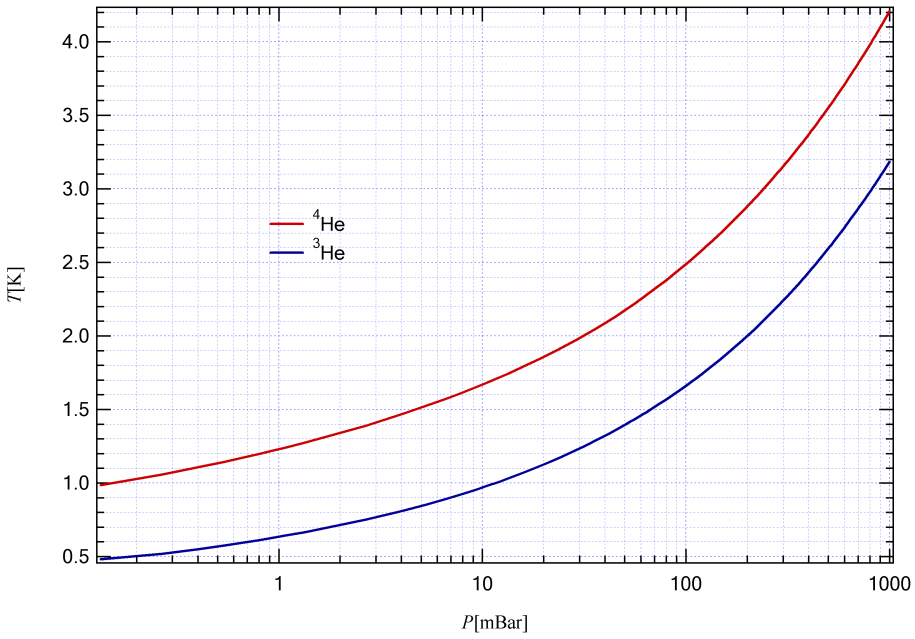

Figure 3.13: The vapor pressure of ^{3}He and ^{4}He decreases exponentially with temperature [87].

3.4 Beamline UE46-PGM1

The experiments using soft x-rays in this thesis were carried out at the beamline UE46-PGM1 at the BESSY II storage ring [88, 89]. The x-ray beam at this beamline is produced by an elliptical undulator of the APPLE-II type, which provides photons in the energy range 123.1 to 1897.5 eV. Because of the longer wave length of soft x-rays, a plane grating monochromator is used instead of a crystal monochromator for selecting the photon energy. The high

x-ray absorption at this low photon energy also means that phase plates are not usable. Instead, variable beam polarization is provided by changing the relative phase of the magnetic field components provided by the four rows of permanent magnets in the elliptical undulator [88].

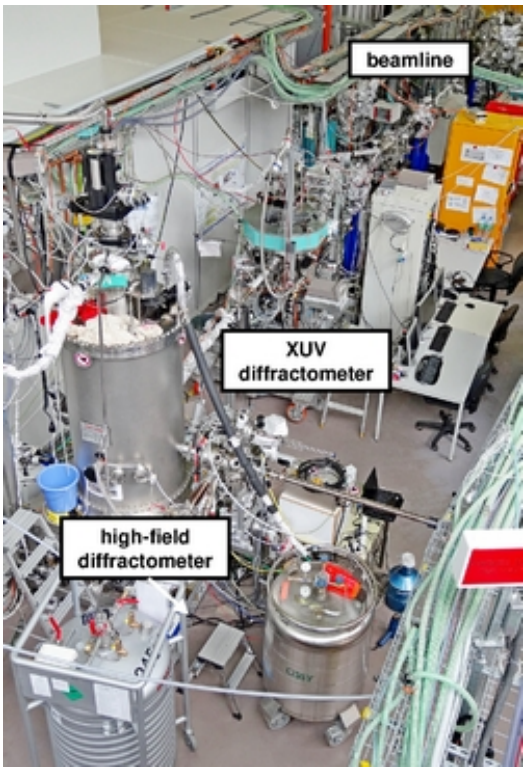

Figure 3.14: Beamline UE46-PGM1 at the BESSY II synchrotron radiation source. Two endstations are available for experiments: An XUV diffractometer and a high-field diffractometer. The beam comes from the beamline front end to the right and can pass through the XUV diffractometer to reach the second endstation [90].

Figure 3.14 shows an overview of the beamline. Two experimental endstations are available. The results using soft x-rays presented in this dissertation were obtained using the 2-circle XUV diffractometer pictured on the right, which is equipped for resonant soft x-ray scattering experiments in UHV conditions. The θ and 2θ circles are inside the UHV chamber in horizontal scattering geometry. The scattered x-rays are detected by a AXUV100 photo diode point detector mounted on the 2θ circle. The sample stage is cooled by a liquid He flow cryostat, which can cool the sample down to 4 K.

Part II

Experimental results

Chapter 4

Dzyaloshinskii-Moriya canting in $TbMnO_3$

4.1 Scientific Case

$TbMnO_3$, as we saw in chapter 2, is a multiferroic perovskite with rich phenomenology that has been studied extensively in recent years. To recapitulate, below $T_N = 41$K, the Mn moments in $TbMnO_3$ order as an A type sinusoidally modulated structure, with moments pointing along the b axis. The wave vector of the structure changes with temperature and locks into the incommensurate value $\boldsymbol{\tau}_{\mathrm{Mn}} = 0.28\mathbf{b}^*$ at $T_C = 27$K, where the Mn magnetic structure changes to an A type bc cycloid, and the sample becomes ferroelectric with $P \| c$. In this FE phase, the Tb orders sinusoidally with the same wave vector as that of the Mn, whereas below $T_N^{\mathrm{Tb}} = 7$K, the Tb moments also order incommensurately among themselves with $\boldsymbol{\tau}_{\mathrm{Tb}} = {}^3\!/_7\mathbf{b}^*$ [30, 31, 32, 91]. At the same transition, the wave vector of Mn changes slightly to the fractional value $\tau_{\mathrm{Mn}} = {}^2\!/_7$. The wave vectors of the two magnetic orders thus obey the harmonic relation $3\tau_{\mathrm{Tb}} - \tau_{\mathrm{Mn}} = 1$ as a result of Tb-Mn exchange interaction [51, 92, 93]. Below T_N^{Tb}, the exact magnetic structure of the Tb moments is not known.

We saw in section 2.3.1 that DM canting is predicted to induce both F, C and G type order of the Mn moments. F type DM canting of the Mn A type structure has been confirmed in $TbMnO_3$ and $Eu_{3/4}Y_{1/4}MnO_3$ in both the paraelectric and the ferroelectric phase [44], but evidence of C and G type canting is still missing. The different magnetic modes manifest themselves in scattering experiments as reflected intensity in different Brillouin zones with different extinction conditions as follows: A type: $h + k =$ even, $l =$ odd; C type: $h + k =$ odd, $l =$ even; F type: $h + k =$ even, $l =$ even; and

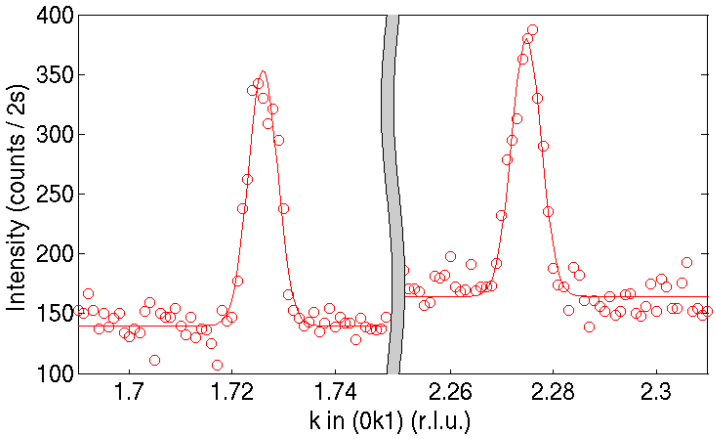

Figure 4.1: A type reflections (0 2$\pm\tau_{\mathrm{Mn}}$ 1), measured at 5.9 K with c perpendicular to the scattering plane.

G type: $h + k$ = odd, l = odd [94, 47]. We have looked for C and G type Mn structures in $TbMnO_3$ using High energy non-resonant x-ray magnetic scattering (HEXMS). Because of the simple cross-section of HEXMS, reliable determination of moment directions is possible using this method. Using this fact, we have also probed the Tb moment direction below T_N^{Tb}.

4.2 Experiment

The HEXMS experiments were performed in EH2 of the P07 Beamline at the PETRA III storage ring at Deutsches Elektronen-Synchrotron (DESY) [95]. The photon energy was tuned to 80 keV. Because of the low x-ray absorption at this energy, the experiment could be performed in horizontal transmissive Laue geometry. The samples were cut into 200μm thick slices, in order to allow the x-ray beam to interact with as much of the sample bulk as possible while still keeping the total absorption below 50%. The samples were cooled in a Displex cryostat. Two $TbMnO_3$ samples were investigated in the ferroelectric phase, mounted in two different scattering geometries; Sample 1 with c perpendicular to the scattering plane, and Sample 2 with a perpendicular to the scattering plane.

In Sample 1, the A type (0 2$\pm\tau_{\mathrm{Mn}}$ 1) reflections were located, with a peak-to-background ratio of $\sim$ 2.5 (figure 4.1). This confirms the existence of the bc cycloidal A type magnetic structure, since in this sample geometry, we probe the c component of the magnetic moment. Figure 4.2 shows the integrated intensity of the (0 2+τ_{Mn} 1) reflection as function of temperature. The commensurate Mn magnetic structure disappears at $\sim$ 27 K as observed

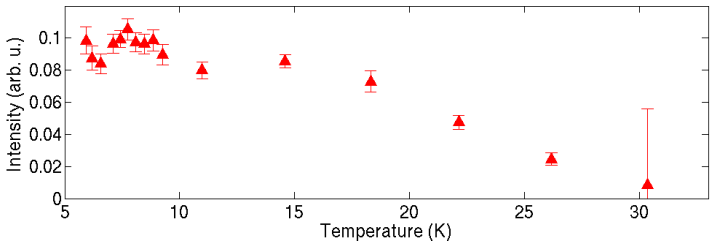

Figure 4.2: Integrated intensity of the A type (0 2+τ_{Mn} 1) reflection as function of temperature.

previously [93, 92]. This further confirms the magnetic origin of the reflection. The HEXMS signal was too weak to resolve the incommensurate magnetic structure associated with the paraelectric phase for $T_C < T < T_N$.

As expected, C and G type reflections were not found in the same scattering geometry as the A type, since the C and G type Mn magnetic structures due to DM canting are both predicted to be the a sinusoidal structure (cf. table 2.1). However, in Sample 2, with a perpendicular to the scattering plane, both C and G type reflections were located. Figure 4.3 displays a reciprocal space scan of the C type reflection (0 1+τ_{Mn} 0), which has a peak-to-background ratio of ~ 1.1. As expected, this is weaker than the A type reflection, since the C type reflection originates from a canting of the A type ordered moments. The same is true for the G type reflections (0 1$\pm\tau_{\mathrm{Mn}}$ 1), which are displayed in figure 4.4. Here, the peak-to-background ratio is also ~ 1.1.

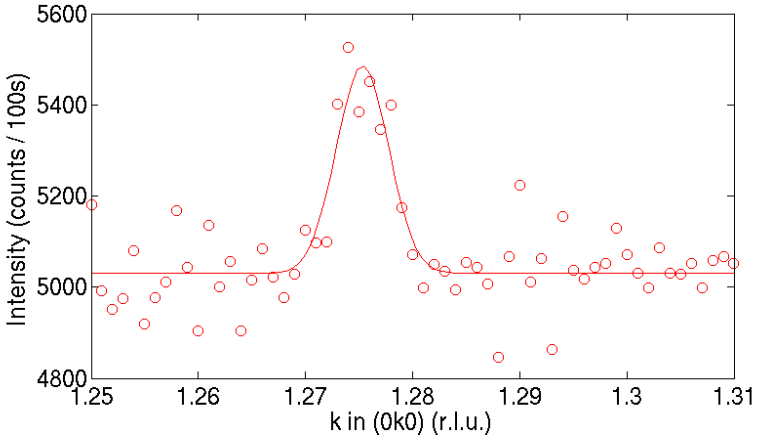

Figure 4.3: C type reflection (0 1+τ_{Mn} 0), measured at 7.1 K with a perpendicular to the scattering plane.

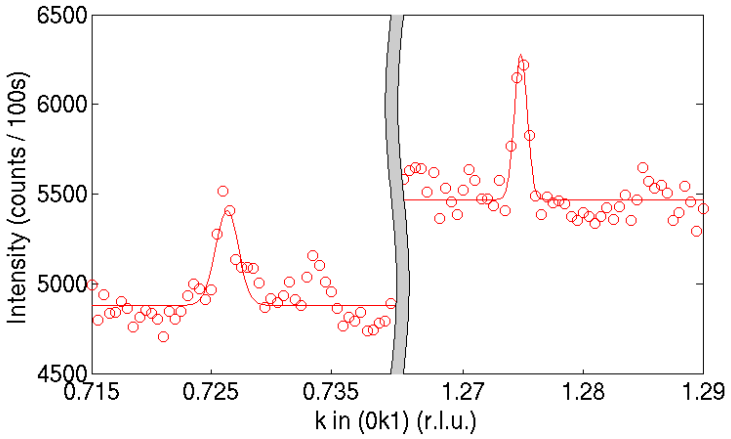

Figure 4.4: G type reflections (0 1$\pm\tau_{\mathrm{Mn}}$ 1), measured at 7.1 K with a perpendicular to the scattering plane.

Below T_N^{Tb}, a reflection with the wave vector of Tb was located at the (0 2+τ_{Tb} 1) position in Sample 1. Figure 4.5 displays reciprocal space scans of the reflection at three different sample temperatures below and above T_N^{Tb}. The transition temperature appears to be around 6.4 K instead of the expected 7 K because of heat load on the sample from the intense x-ray beam. Scattered intensity in this scattering geometry indicates a magnetic moment component along the c direction at the Tb site.

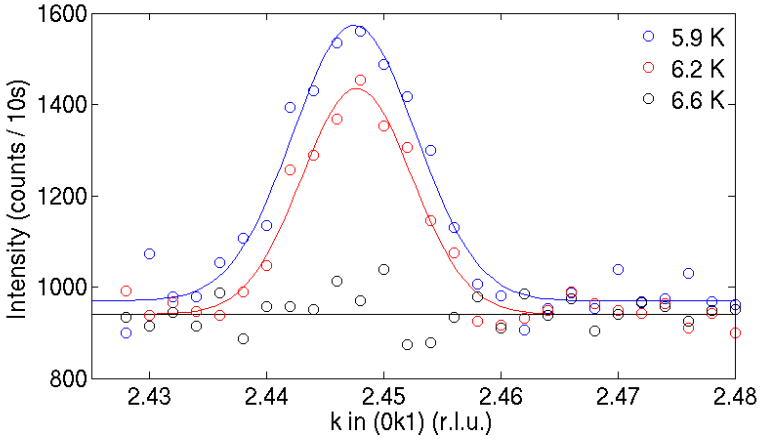

Figure 4.5: Tb reflection (0 2 +τ_{Tb} 1), measured at 5.9 K, 6.2 K and 6.6 K with c perpendicular to the scattering plane.

4.3 Discussion

The existence of C and G type magnetic structures with moments along a in $TbMnO_3$ confirms the predicted DM canting of the A type Mn magnetic ordering. The true spin structure of $TbMnO_3$ is thus a multifaceted structure which may have to be taken into account when trying to explain multiferroicity in this compound, since the additional moment directions associated with the C and G type order may facilitate additional exchange interactions between the Mn spins. Furthermore, we have established the Tb to have a magnetic moment component along c below T_N^{Tb}.

Chapter 5

Symmetric exchange interaction in $GdMnO_3$

5.1 Scientific Case

Strong magneto-electric coupling has been observed in orthorhombic rare-earth manganites $R\mathrm{MnO_3}$ [9, 16, 96, 97]. As we saw in chapter 2, possible microscopic mechanisms for multiferroicity are still being explored, and in these compounds the rare-earth moments have been observed to play a complex role. For example, in $DyMnO_3$ a threefold enhancement of the electric polarization is seen above 6.5 K, or when applying a magnetic field parallel to the a axis below 6.5 K, where Dy exhibits Mn-induced ordering [51, 52]. On the other hand, ferroelectricity in $GdMnO_3$ is almost entirely dependent on an applied magnetic field. As described in section 2.2.1, the basic mechanism for ferroelectricity in $DyMnO_3$ is *antisymmetric* exchange striction of the form $\mathbf{D_{ij}} \cdot [\mathbf{S_i} \times \mathbf{S_j}]$ between neighboring Mn moments, which breaks inversion symmetry and displaces oxygen ions perpendicular to the ordering wave vector [23, 22, 18]. In contrast, the *symmetric* exchange striction of the form $J\mathbf{S_i} \cdot \mathbf{S_j}$ between Dy and Mn is hypothesized to be responsible for the polarization enhancement in $DyMnO_3$, and also for the magnetic-field induced ferroelectricity in $GdMnO_3$ [53].

In $GdMnO_3$, the Mn moments order incommensurately below $T_N^{Mn} = 43$ K [16, 98]. Below the lock-in temperature, $T' = 23$ K, the Mn order undergoes a transition to commensurate A-type AF ordering associated with weak ferromagnetism [52]. This ordering breaks spatial inversion symmetry, as required for ferroelectricity. In spite of this, $GdMnO_3$ is not ferroelectric in this phase, and it is necessary to look for additional mechanisms.

Below $T_N^{Gd} = 8.2$ K, both the Gd moments and the Mn moments order

with propagation vector $\boldsymbol{\tau}^{Gd} = \boldsymbol{\tau}^{Mn} = \frac{1}{4}\mathbf{b}^*$. This can, through the symmetric exchange interaction, cause a lattice modulation with period $q = \tau^{Gd} - \tau^{Mn} = 0$, i.e. a homogeneous lattice contraction or expansion that under certain conditions may be polar, thus leading to ferroelectricity [52]. An overview of possible modulations arising from various types of spiral magnetic ordering has been listed by Arima *et al.* [99, 100]. However, in zero field $GdMnO_3$ is only ferroelectric in a small temperature range around 5 K, even though both Mn and Gd moments are ordered with $\tau = 1/4$ down to base temperature. Ferroelectricity is induced in a larger temperature range by application of a magnetic field along the b axis. Here, one paraelectric-to-ferroelectric transition coincides with a phase boundary within the Gd ordered state [52]. We have studied the Gd ordering as a function of temperature and magnetic field in order to shed some more light on the interplay between magnetism at the Gd site and ferroelectricity in $GdMnO_3$ [101].

5.2 Experiment

The experiments have been conducted at beamlines P09 at the PETRA III storage ring at Deutsches Elektronen-Synchrotron (DESY) [79] and 6-ID-B at the Advanced Photon-Source (APS) at Argonne National Laboratory. In both cases, the sample was mounted and cooled in a cryomagnet with vertical field direction along the crystallographic b direction. The scattering plane was tilted slightly away from the ac plane in order to access reflections with a small k value.

The magnetic (0 1/4 6) reflection was investigated as function of temperature and magnetic field. At the Gd L_2 edge a strong resonant signal was measured in the π-σ' channel, confirming the magnetic origin of the reflection (see inset of figure 5.1). Measurements were also performed with a perpendicular to the scattering plane. In this scattering geometry, at $T \sim 5.7$ K (not shown here), there is no intensity in the π-π' channel at resonance, excluding any a component of the Gd moments. This is in accordance with previous studies indicating Gd ordering predominantly along c [52].

Figure 5.1 shows the dependence upon temperature of the magnetic scattering intensity in the π-σ' channel with b perpendicular to the scattering plane, for different field strengths. In zero field, a maximum around $T^* \sim 6$ K is seen. Previous measurements have shown that this is related to an increase of the b component of the Gd spins [52] and corresponds to the narrow ferroelectric range in the absence of magnetic field, ranging from about 5.5 K to 8.5 K [97]. Application of a small field of 4 kOe results in a slight enhancement of the intensity in this region, while leaving the overall field dependence

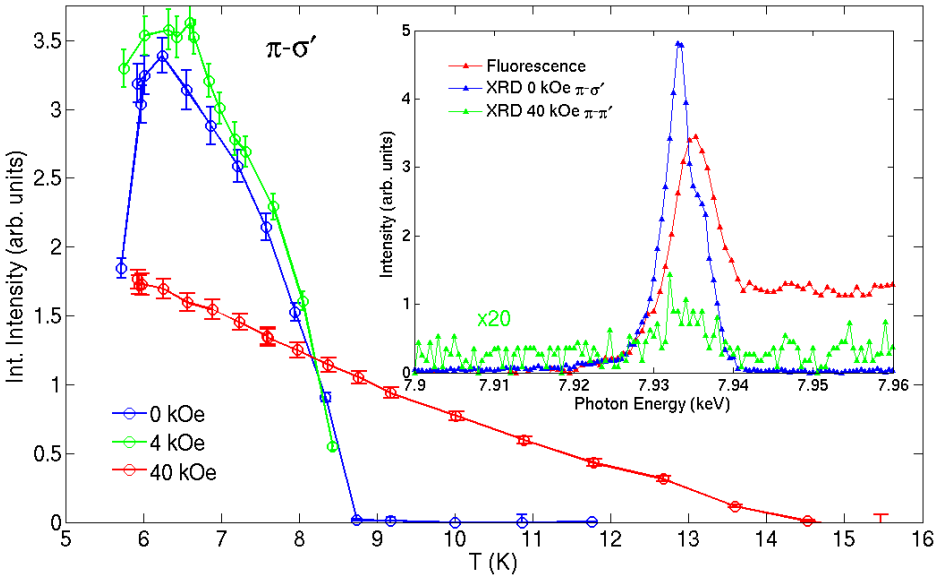

Figure 5.1: Temperature dependence of the (0 ¼ 6) integrated intensity at different field values, measured in the π-σ' channel with a photon energy of 7.9325 keV. The inset shows the absorption corrected energy dependence across the Gd L_2 edge at T = 5.7 K, in zero field in π-σ' as well as under application of a magnetic field in π-π', along with a fluorescence measurement of the sample [101].

intact. Increasing the field strength to 40 kOe suppresses the intensity again, but in turn extends the ordered phase to 15 K. This new transition temperature changes with field strength and does not correspond to any transition in the Mn order, indicating an onset of Gd self-ordering. With the magnetic field strength set to 40 kOe there is a weak XRD signal (which is clearly above the intensity level expected from cross-talk between the polarization channels) also in the π-π' channel, indicating a small Gd spin component also in the b direction.

In order to understand the effect of an applied magnetic field, we recorded field dependencies at several different values of constant temperature. The results are shown in Figure 5.2. The measurements map out the H-T phase diagram of the Gd order. Comparison with the phase diagram from Ref. [97] shows that the Gd ordered phase corresponds to the ferroelectric phase in all regions.

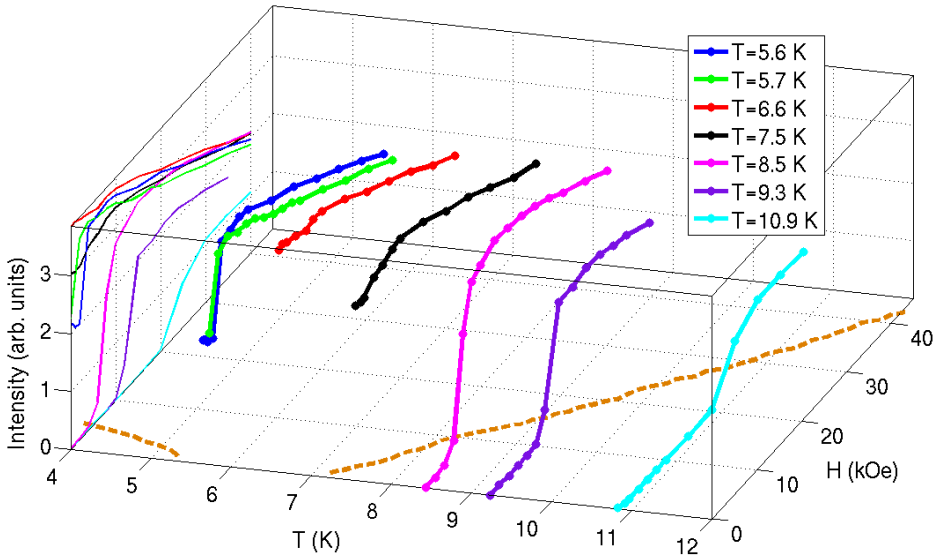

Figure 5.2: Field dependencies of the (0 ¼ 6) integrated intensity as function of **H** ∥ **b** at fixed temperatures, with projections [101]. The orange dashed curves represent the boundaries of the ferroelectric phase from the phase diagram in [97].

5.3 Discussion

The existence of a *b* component of the Gd moments in the high-field region is suggestive of an important role for the symmetric magnetic exchange interaction in stabilizing the ferroelectric phase. The symmetric exchange interaction between Gd and Mn moments is proportional to $\mathbf{S}_{Gd,i} \cdot \mathbf{S}_{Mn,j}$ which is zero when the Gd moments are oriented along *c*, perpendicular to the Mn moments in the *ab*-plane. Appearance of the *b* component at the Gd site makes the exchange interaction non-zero, capable of causing a shift of the Gd ions towards the Mn ions. Our results therefore point to an important role of the rare earth moments for the ferroelectricity in orthomanganites, and may open up a simple route to enhance the ferroelectricity in multiferroics where the rare earth and transition metal ions order with the same wave vector.

Chapter 6

Magnetic phases in $\mathbf{Eu_{1-x}Y_xMnO_3}$

6.1 Scientific Case

We already looked at the system $Eu_{1-x}Y_xMnO_3$ in chapter 2 and saw that in addition to acting as a model system for other multiferroic perovskites, it has several fascinating multiferroic properties of its own. Of particular interest is the range of compounds with $x \sim 0.2 - 0.3$, in the crossover region from the paraelectric and weakly ferromagnetic phase to the ferroelectric phase (cf. Fig. 2.3), since these offer the possibility of multiple phases coexisting.

The magnetic structure of a compound in the center of this narrow x range, $Eu_{3/4}Y_{1/4}MnO_3$, has been studied in the past [50, 44]. This composition is particularly interesting because it allows for the coexistence of the weakly ferromagnetic AFM(A) and the paraelectric phases in a magnetic glass state [50]. This coexistence is strongly dependent on the T-H history of the sample.

It was concluded that after cooling in zero field, the ground state of this sample is the paraelectric phase accompanied by an A type cycloidal structure in the ab plane, with a commensurate ordering wave vector $\boldsymbol{\tau} = 1/4\mathbf{b}$. In the paraelectric phase above T_C, the wave vector becomes incommensurate, and the Mn moments order as an A type b axis sinusoid.

The Dzyaloshinskii-Moriya interaction plays an important role in the multiferroicity of this type of compounds. In addition to being responsible for the ferroelectricity in spin spiral systems, it may also effectuate spin canting due to the oxygen shift in the perovskite structure. Just as in $TbMnO_3$, the DM interaction is predicted to induce F, C and G type canting of the Mn magnetic structure in $Eu_{1-x}Y_xMnO_3$ (cf. section 2.3.1 and chapter 4). We

have performed REXS studies on $Eu_{0.8}Y_{0.2}MnO_3$ and $Eu_{0.7}Y_{0.3}MnO_3$ to look for evidence of this DM canting.

It has been suggested that the coexistence of ferromagnetism and ferroelectricity can occur also in $Eu_{0.8}Y_{0.2}MnO_3$ [35], but more recent results do not support such a coexistence [36, 102]. It has however been observed that $Eu_{0.8}Y_{0.2}MnO_3$ can choose either phase after cooling, depending on the cooling conditions. Danjoh *et al.* [49] observed that after cooling in zero field (ZFC), the compound settles in the ferroelectric phase without any magnetization below $T_C = 30K$. On the other hand, cooling the sample in a magnetic field of 5 T along c (FC(5T)) resulted in a remanent magnetization below 20 K, concurrent with a suppression of the electric polarization and a change in the lattice parameters due to magnetostriction (see figure 6.1).

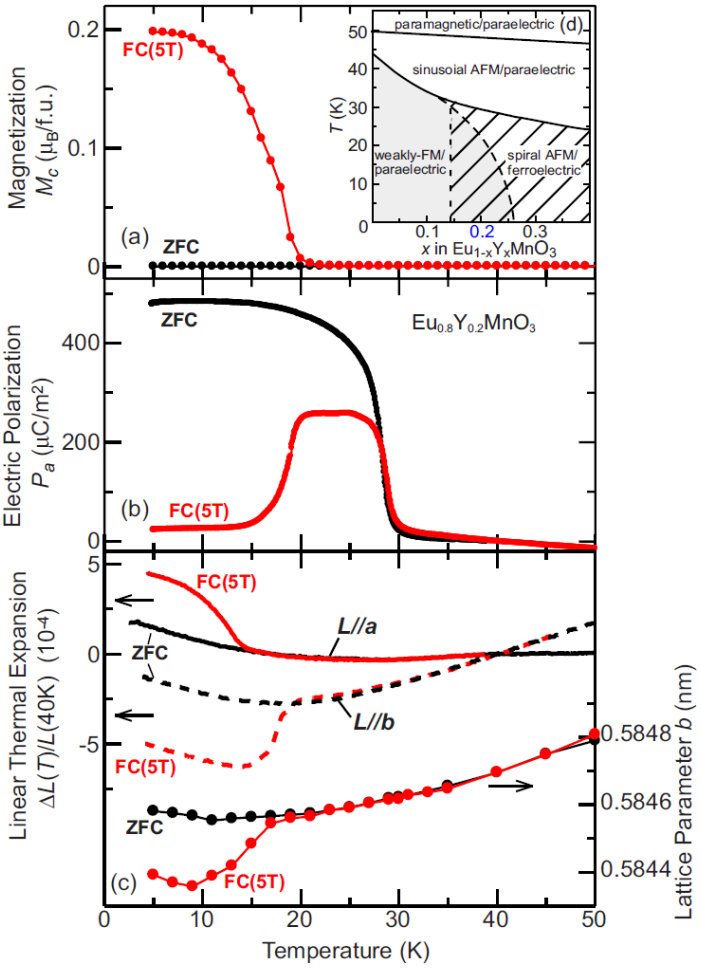

Figure 6.1: Temperature profiles of (a) magnetization along c, (b) electric polarization along a, (c) linear thermal expansion along a and b, and lattice parameter b for $Eu_{0.8}Y_{0.2}MnO_3$. The inset shows a part of the phase diagram from figure 2.3 (c) [49].

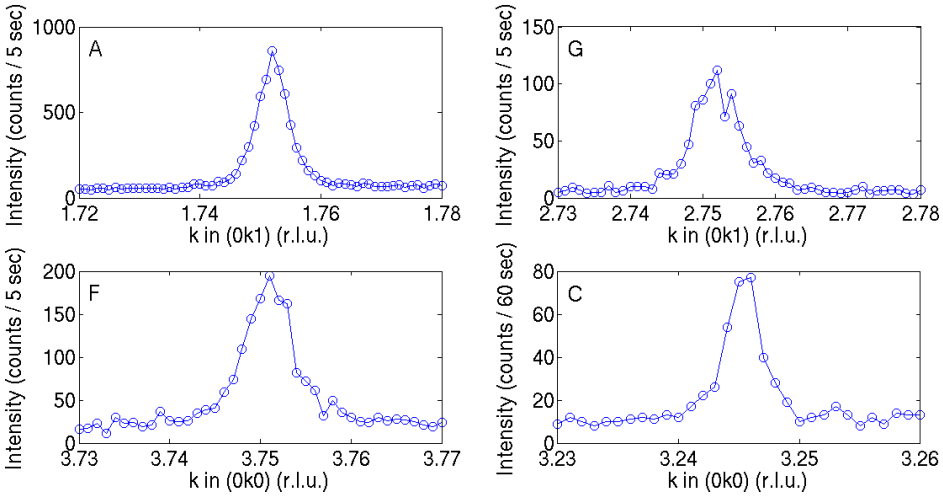

Figure 6.2: Magnetic reflections from four different magnetic modes in $Eu_{0.8}Y_{0.2}MnO_3$; A type (0 2-τ 1), F type (0 4-τ 0), G type (0 3-τ 1) and C type (0 3+τ 0).

6.2 Zero field studies

The experiments using hard x-rays were conducted at the P09 beamline at the PETRA III storage ring at Deutsches Elektronen-Synchrotron (DESY) [79]. We have studied two samples with different doping levels, $x = 0.2$ and $x = 0.3$. For temperature studies and polarization analysis, the samples were mounted in a 6-circle diffractometer in the first experimental hutch, with the crystallographic c direction perpendicular to the vertical scattering plane. The samples were cooled with a Displex cryostat. For measurements in magnetic field, the samples were mounted and cooled in the 14 T Cryogenic cryomagnet in the second experimental hutch, with field direction along a, perpendicular to the horizontal scattering plane. The photon energy was tuned close to the Mn K edge.

Resonant magnetic reflections of all four expected types (A, C, F and G) were found in both samples at $T = 10$K. Reciprocal space scans along k for these in the compound with $x = 0.2$ are shown in figure 6.2. The magnitude of τ is very close to the commensurate value $1/4$. Figure 6.3 shows how the signals resonate at the Mn K edge. The lineshapes are typical for a Mn K edge resonant signal originating from a magnetic structure, and look the same in both samples. The A type reflection (0 2-τ 1) shows a strong dipole resonance around 6554 eV along with a weaker quadrupole resonance at 6541 eV. The other magnetic modes show the same features, although the quadrupole in the G type spectrum is strongly reduced, and almost fully

suppressed for the F and C type spectrum. This is to be expected, since the F and C type structures are predicted to be collinear, and most of the terms in the quadrupolar scattering amplitude involve a product between two magnetic moment components [64].

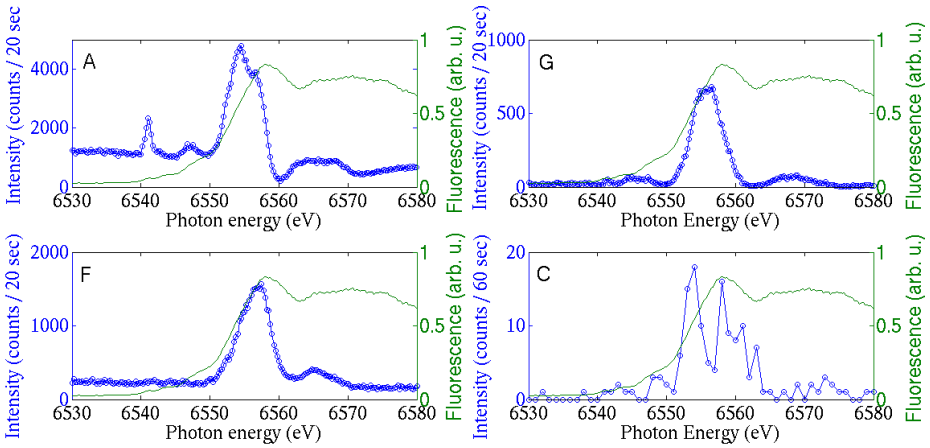

Figure 6.3: REXS spectra across the Mn K absorption edge from four different magnetic modes in $Eu_{0.8}Y_{0.2}MnO_3$; A type (0 2-τ 1), F type (0 4-τ 0) and G type (0 3-τ 1) and C type (0 3+τ 0). A fluorescence spectrum from the sample is superposed.

The reflected intensities at the dipole resonance were investigated as function of temperature and photon polarization. The temperature dependence of the A type (0 4-τ 1) reflection in $Eu_{0.7}Y_{0.3}MnO_3$ is shown in figure 6.4. In the ferroelectric phase below $\sim$ 25 K, we see a commensurate magnetic structure with wave vector $\boldsymbol{\tau} = 1/4$. The signal is present in both polarization channels, in concordance with the moments aligning in the ab plane. In the paraelectric phase 25K $< T <$ 45K, the magnetic structure is incommensurate. With decreasing temperature, the wave vector is decreasing linearly before locking into the commensurate value at the phase transition. The A type structure in this phase is expected to form a collinear b-axis sinusoidal structure [44], which is confirmed by the incommensurate signal only being present in the π-σ' and σ-π' channels.

For $Eu_{0.8}Y_{0.2}MnO_3$ two remarkable differences are seen. Whereas in $Eu_{0.7}Y_{0.3}MnO_3$ the wave vector in the paraelectric phase locks into the commensurate value at the phase transition into the ferroelectric phase, the wave vector of the incommensurate phase in $Eu_{0.8}Y_{0.2}MnO_3$ moves *away* from the commensurate value going down in temperature. Also, in the crossover region between the two phases an additional incommensurate magnetic structure can be discerned existing in parallel to the commensurate structure.

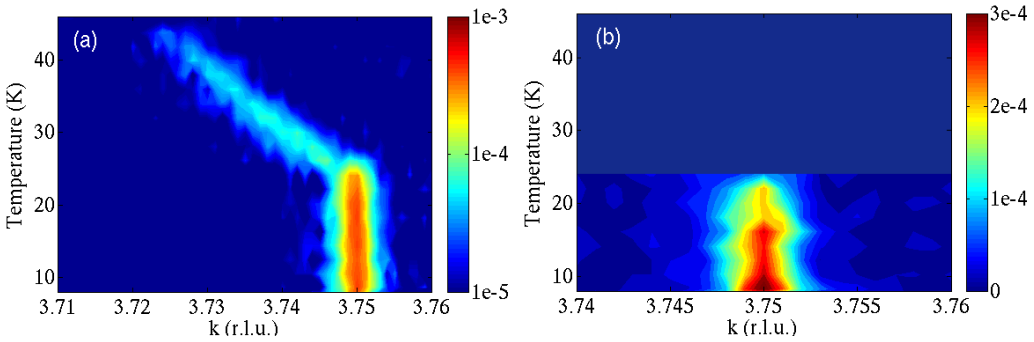

Figure 6.4: Temperature dependence of the A type (0 4-τ 1) reflected intensity from $Eu_{0.7}Y_{0.3}MnO_3$ in (a) π-σ' and (b) π-π' geometry.

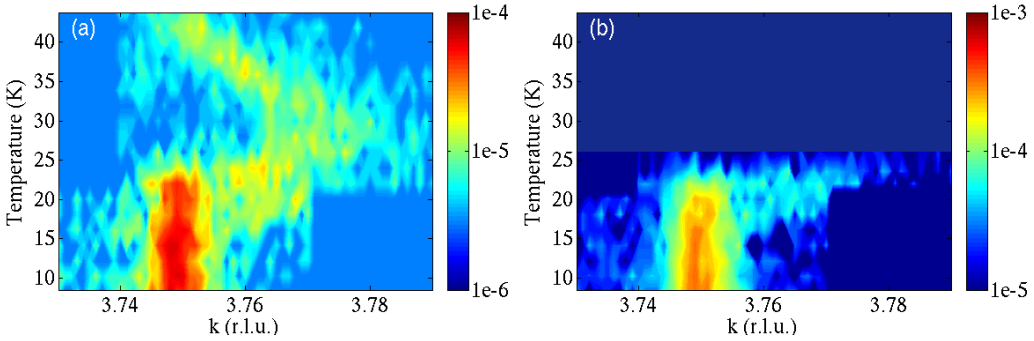

Figure 6.5: Temperature dependence of the A type (0 4-τ 1) reflected intensity from $Eu_{0.8}Y_{0.2}MnO_3$ in (a) π-σ' and (b) π-π' geometry.

This incommensurate signal is present in both π-σ' and π-π', hinting at a similar moment direction as the commensurate structure. We can associate this additional magnetic order with an anomaly in the dielectric constant at T $\sim$ 22 K as observed by Hemberger et al. [35].

The above-mentioned phases are also evident in the other magnetic modes, albeit with different polarization dependencies according to their magnetic structures. In the following we will only consider the measurements on $Eu_{0.8}Y_{0.2}MnO_3$. The measurements for $x = 0.3$ all look similar to the ones for $x = 0.2$, except for the offset of the incommensurate wave vector and the presence of an additional incommensurate phase close to the phase transition in $Eu_{0.8}Y_{0.2}MnO_3$.

Figure 6.6 shows the temperature dependencies of the F type (0 4-τ 0) and the C type (0 3+τ 0) reflections, both in π-σ' geometry. DM canting is

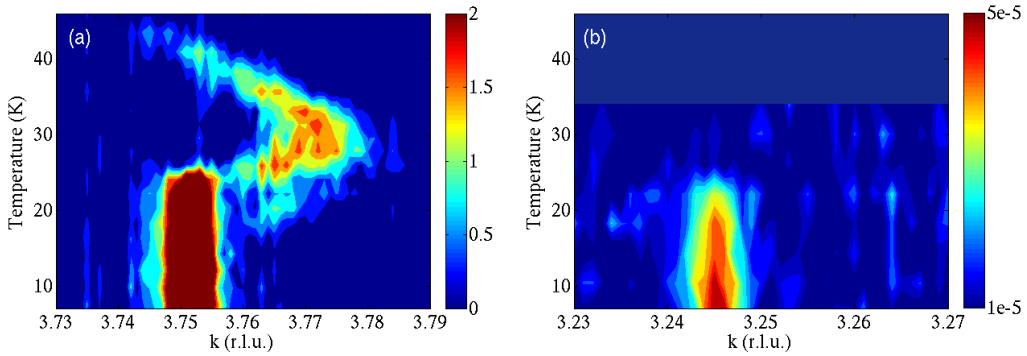

Figure 6.6: Temperature dependence of (a) the F type (0 4-τ 0) and (b) the C type (0 3+τ 0) reflected intensities in π-σ' geometry.

expected to induce an F type c axis sinusoidal structure in both the ferroelectric and paraelectric phase, which is confirmed by the F type reflection having zero intensity in the π-π' channel. Likewise, the expected C type c axis sinusoidal structure in the ferroelectric phase is confirmed. DM canting is not expected to induce any C type structure in the paraelectric phase, which reflects itself in the lack of a signal in all polarization channels above $\sim$ 25 K. It is also worth noting that the intermediate incommensurate phase observed at other magnetic reflections is not seen in the C type reflection, although we will see in the next section that this is a result of the very weak signal rather than an actual absence of the structure.

Due to the weakness of the resonant signal, especially in the incommensurate phases, it is difficult to extract precise values for the scattered intensities and wave vectors. It is therefore helpful to also measure the magnetically induced charge scattering, as described in section 3.2.3. As the scattered intensity is not magnetic in origin, it is most strongly visible in the σ-σ' and π-π' polarization channels, but some intensity is also seen in the σ-π' and π-σ' channels due to leakage. The high intensity compared to the magnetic REXS signal allows for more precise measurements of relative intensities and the wave vector τ. It also has the added benefit of allowing for a much higher attenuation of the incident beam, eliminating the problem of beam heating.

Figure 6.7 shows the temperature dependence of the integrated intensity (a) and reciprocal space position (b) of one such structural reflection. The reflection can be indexed as (0 4-2τ 1) and is related to the structural distortion due to the A type magnetic structure. Some details about the different magnetic phases are easier to make out here. The order parameter-like onset of the low temperature ferroelectric phase is clearly seen at $\sim$ 27 K, which

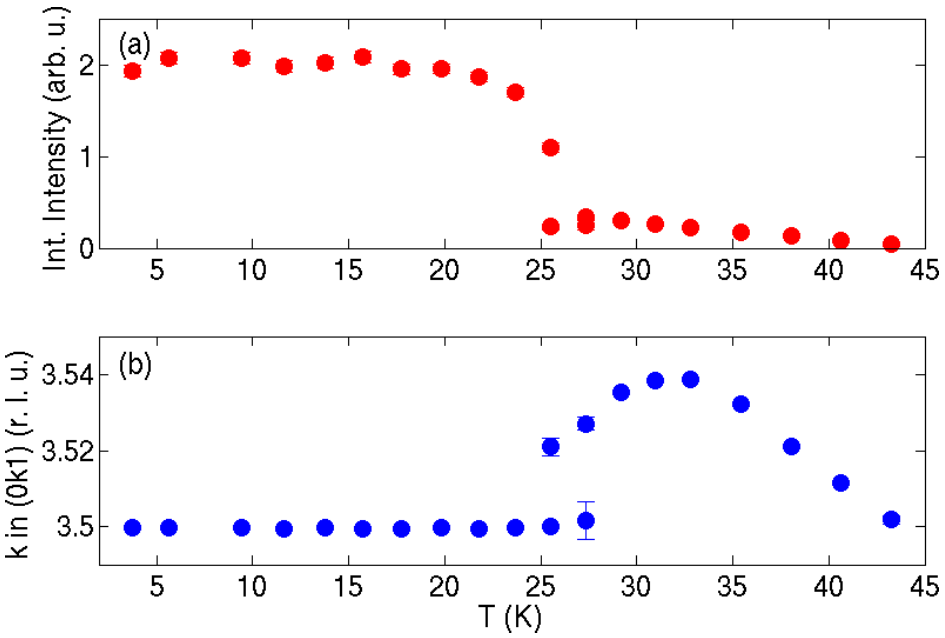

Figure 6.7: Temperature dependence of (a) the integrated intensity and (b) the reciprocal space position of the structural (0 3.5 1) reflection.

is similar to the value observed in bulk measurements [35]. Likewise, the linear dependence of the wave vector in the paraelectric phase up to ~ 45 K is recognized. The competing incommensurate phase in the crossover range close to the transition temperature is also visible in this measurement and shows the same behavior as at the magnetic reflections.

6.2.1 Full Polarization Analysis

Solving the exact magnetic structure of compounds such as $R\mathrm{MnO_3}$ can be done by continuously probing different linear combinations of the scattering channels in equation 3.24. This can be achieved by rotating the sample around the scattering vector (an azimuthal, or Ψ scan) to bring different magnetic moment components into the scattering plane and analyzing the polarization of the reflected beam using a crystal analyzer. However, this technique suffers from several experimental difficulties, both from the sample and from the experimental environment. For example, if the sample has high mosaicity or twinning, the movement of the sample during the Ψ rotation may make the beam fall off the magnetic reflection condition. Complex sample environments such as cryostats and cryomagnets may also heavily restrict the movement of the sample.

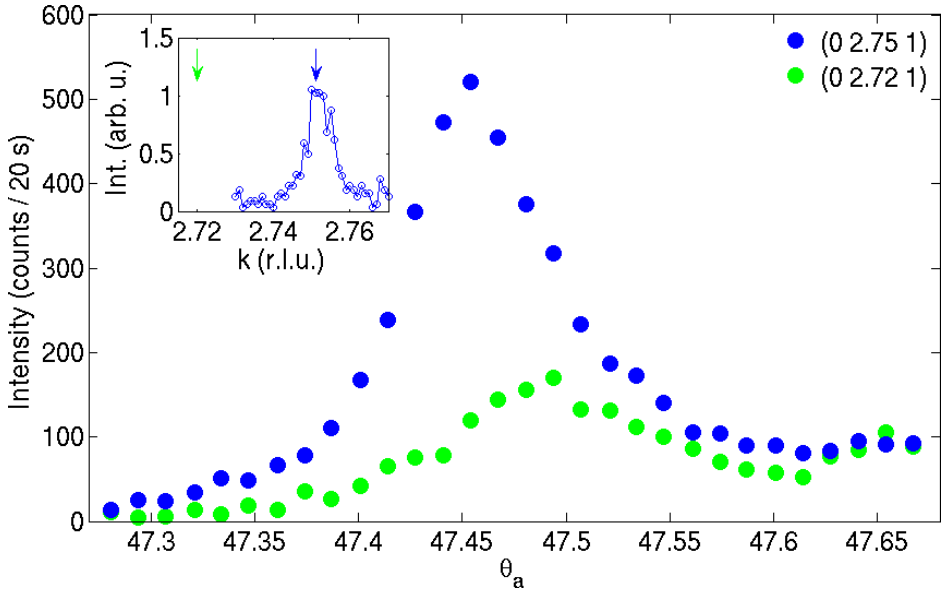

Figure 6.8: An example of analyzer rocking curves measured during the full polarization analysis of the G type magnetic structure, for $\eta = -45°$ and $\eta' = 0°$. To measure only the polarization of the magnetic scattered intensity, the charge scattering background (green) is subtracted from the total signal (blue). The arrows in the inset shows the positions in reciprocal space where the two different rocking curves were measured.

An alternative method is to keep the sample fixed and rotate instead the polarization of the incident beam using a phase retarder setup, while at the same time analyzing the polarization of the reflected beam. This is known as Full Polarization Analysis and allows for stable measuring conditions over an indefinite amount of time, while still probing all the relevant scattering channels [103].

In order to solve the exact magnetic structure of the G and F modes, we used the method of full polarization analysis, as outlined by Mazzoli *et al.* [103]. The full polarization analysis was performed by keeping the sample fixed in the Bragg condition for the given reflection, while rotating the angle η of incident photon polarization using the phase retarders. For each value of incident polarization angle, the polarization of the diffracted beam was analyzed by rotating the crystal analyzer about the scattered beam while measuring the reflected intensity for several values of the analyzer rotation angle η'. The Stokes' parameters of the scattered beam were then extracted

by fitting to the integrated intensities $I(\eta')$ the function

$$I(\eta') = \frac{P'_0}{2}\left(1 + P'_1 \cos 2\eta' + P'_2 \sin 2\eta'\right). \tag{6.1}$$

A value for P'_3, which quantifies the circular polarization, is not obtainable with this method. However, an upper limit on P_3^2 can be found using the equation $P_1'^2 + P_2'^2 + P_3'^2 \leq 1$, where the equality holds for a fully polarized beam.

The integrated intensities were collected using rocking scans of the crystal analyzer. Care had to be taken to avoid contamination of the signal by the strong structural Bragg reflections, since these reflect light of different polarization than the magnetic reflections. In our case, due to the relatively small wave vector $\tau = 1/4$, the magnetic reflections were located on the tail of the neighboring structural reflections. In order to collect only the magnetic signal, each rocking scan was performed twice; once in the center of the magnetic reflection, and once to the side of the magnetic peak in reciprocal space, in order to measure the charge scattering background (cf. figure 6.8). The second scan was then subtracted from the first in the analysis to filter out the charge scattering and only consider the scattered intensity due to the magnetic order.

Thus we were able to collect data about the polarization of the scattered magnetic intensity as a function of incident photon polarization. Different moment orientations in the sample will influence the polarization of the scattered beam according to equation (3.24). Using this, we can calculate the expected Stokes' parameters $P'_1(\eta)$, $P'_2(\eta)$ and $P'_3(\eta)$ of the diffracted beam as functions of the angle of incident polarization η for different magnetic structures. These calculations are derived in Appendix A.

Figure 6.9(a) shows the Stokes' parameters obtained from our full polarization analysis of the F type reflection (0 4-τ 0) in $Eu_{0.8}Y_{0.2}MnO_3$. The results confirm that the F type reflection is due to a collinear c axis sinusoidal magnetic structure, consistent with DM canting of the A type ab cycloid. The same mechanism is also predicted to lead to a G type cycloidal structure where the spins rotate in the ab plane. This is also confirmed by our full polarization analysis of the G type (0 3-τ 1) reflection, shown in figure 6.9(b), with $P'_3(\eta)$ assuming a fully polarized beam. A notable difference from the F type reflection is that $P'_3(\eta)$ is not zero, meaning that the cycloidal magnetic structure introduces a circularly polarized component to the diffracted beam. This is confirmed by our calculations in Appendix A.

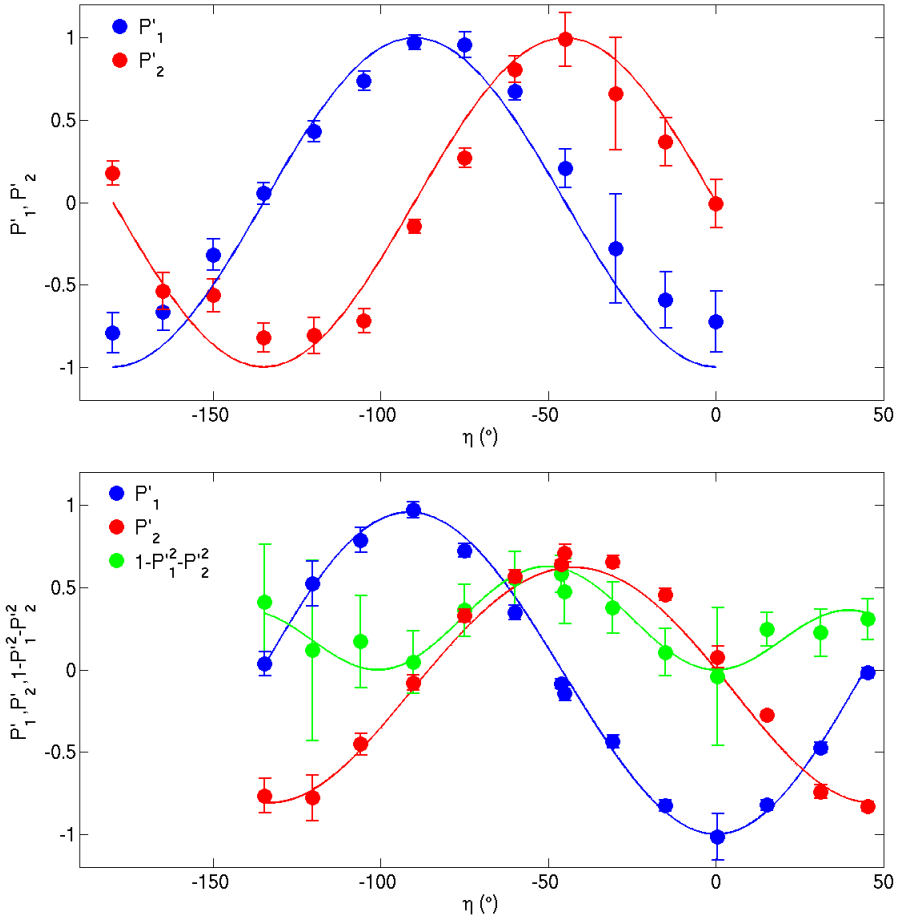

Figure 6.9: (a) Full polarization analysis of the F type reflection (0 4-τ 0). Curves are calculated Stokes parameters of the diffracted beam for a collinear c axis sinusoidal structure. (b) Full polarization analysis of the G type reflection (0 3-τ 1). Curves are calculated Stokes parameters for a circular ab cycloid.

6.2.2 Soft x-ray studies

The soft x-ray experiments were carried out using the XUV diffractometer and the High-field diffractometer at beamline UE46-PGM1 at the BESSY II storage ring [88, 89]. Horizontal scattering geometry was used by scattering from the polished b surface of the sample with c perpendicular to the scattering plane. The beam could be switched between σ and π incident polarization using different undulator settings. The setup did not use a polarization analyzer, so the total reflected beam was measured.

The experiment was carried out at the Mn $L_{2,3}$ absorption edges. Com-

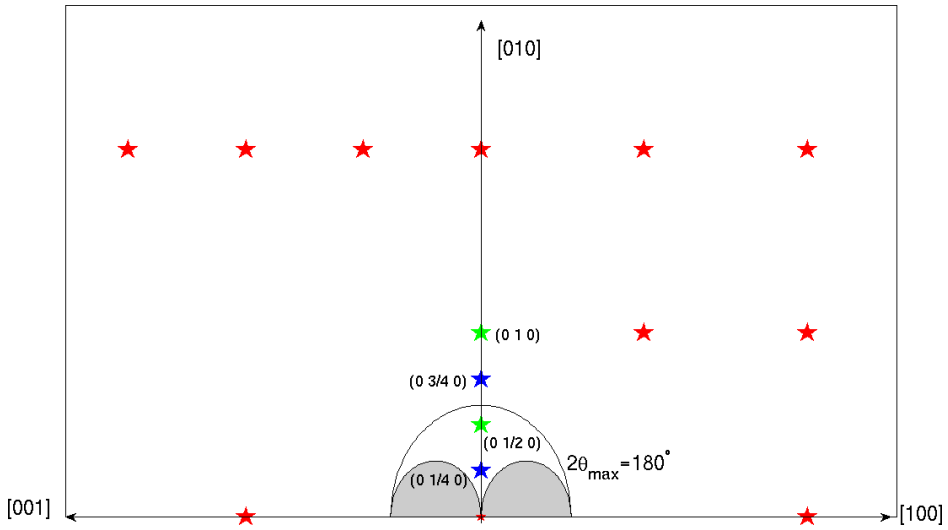

Figure 6.10: Reciprocal lattice of $Eu_{1-x}Y_xMnO_3$ with Ewald sphere at the Mn L_2 edge. Red stars denote structural Bragg reflections, blue stars magnetic reflections, and green stars selected forbidden reflections.

pared to the Mn K edge, the resonant scattering here probes directly the relevant $3d$ states, resulting in a much stronger signal. However, due to the low photon energy, the experiment had to be performed in UHV conditions to avoid absorption from air. The penetration depth into the sample is also very short at these energies, leading to very broad rocking curve widths. It also means that the experiment is more sensitive to surface effects. Another point to consider is that the Ewald sphere at these energies is very small. Figure 6.10 shows the intersection of the Ewald sphere with the reciprocal lattice of $Eu_{1-x}Y_xMnO_3$ at the Mn L_2 edge, $h\nu = 652.4$eV. We see that the only available reflections for measurement are the F type magnetic $(0\ \tau\ 0)$ and the structural $(0\ 2\tau\ 0)$ reflections.

At 10 K, the magnetic reflection $(0\ \tau\ 0)$ showed intensity in the π channel only, meaning that the observed Mn moments are oriented perpendicular to the scattering plane, i.e. along c. This is in accordance with our hard x-ray measurements and with the predicted F type sinusoidal magnetic structure. Figure 6.11 shows the energy dependence of the integrated intensity of this magnetic reflection from $Eu_{0.7}Y_{0.3}MnO_3$ across the Mn $L_{2,3}$ edges. The lineshape is similar to the one observed in other compounds of RMnO$_3$ [104, 44]. The following measurements were all performed at the Mn L_2 edge resonance, with the photon energy tuned to 654.2eV.

Figure 6.12 displays a collection of q-scans across the F type $(0\ \tau\ 0)$ reflection from $Eu_{0.7}Y_{0.3}MnO_3$ in a temperature series from 12 K to 52 K.

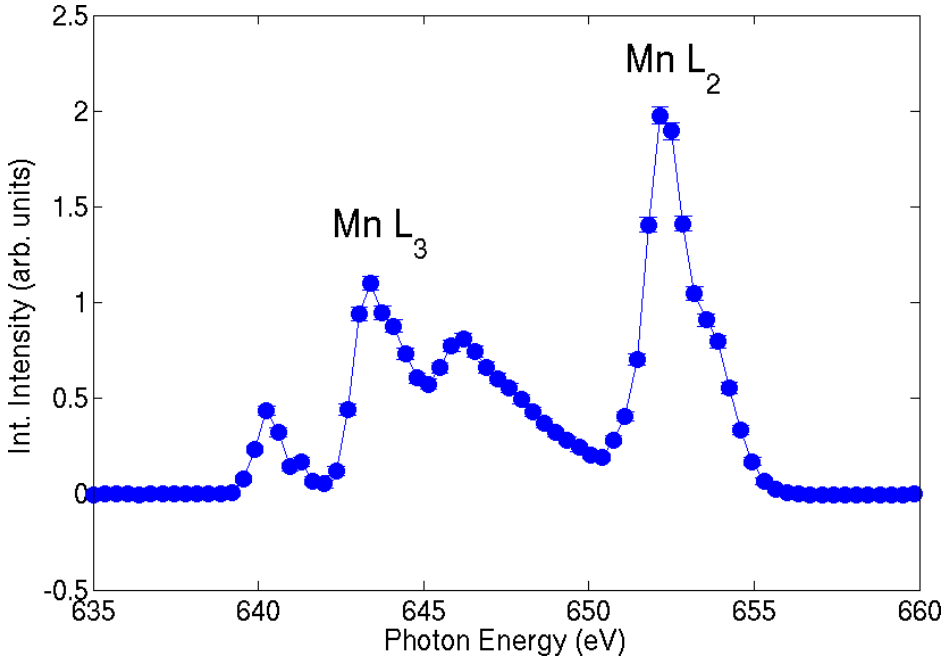

Figure 6.11: Energy dependence of the integrated intensity of the F type (0 τ 0) reflection from $Eu_{0.7}Y_{0.3}MnO_3$ across the Mn $L_{2,3}$ absorption edges.

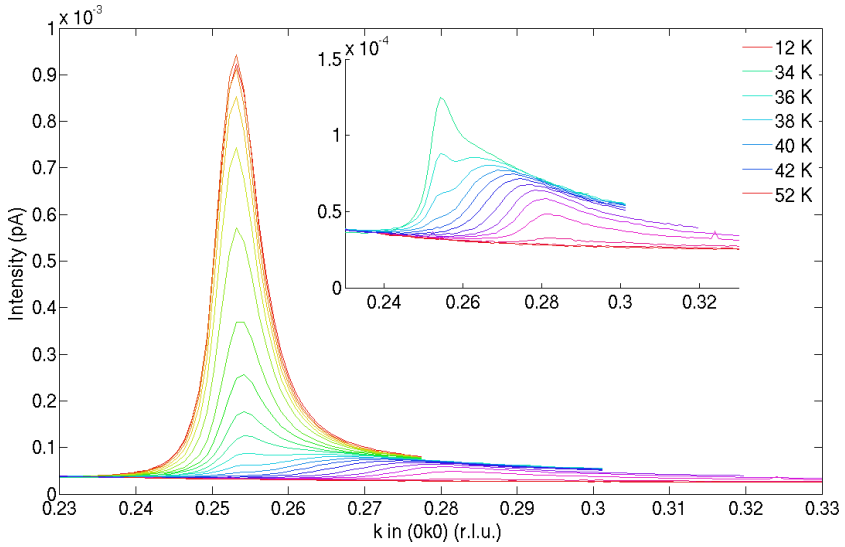

Figure 6.12: Temperature dependence of the F type (0 τ 0) reflection from $Eu_{0.7}Y_{0.3}MnO_3$ at the Mn L_2 absorption edge. The inset shows a blowup of the temperature range above 34 K.

Highly asymmetric peaks and large overlap between the broad reflections makes peak fitting difficult, but the behavior observed at the Mn K edge is nonetheless reaffirmed, with some notable differences. The LT commensurate structure is seen to follow an order parameter like behavior up to T_C, where the incommensurate structure takes over. However, both structures last until higher temperatures than observed at the Mn K edge. In the inset of figure 6.12 a remnant of the commensurate peak can be seen all the way up to 36 K. The wave vector of the incommensurate structure shows the same linear increase as at the Mn K edge, but persists up to 50 K. These differences from the hard x-ray data are likely due to surface effects more prominently seen in the soft x-ray range, since the short attenuation length of 0.2μm at the Mn L edges compared to $\sim 10\mu$m at the Mn K edge means that the surface layer contributes a relatively larger part to the total scattered signal.

The problem of overlapping and asymmetric peaks is even more pronounced in $Eu_{0.8}Y_{0.2}MnO_3$, where the peaks are overlapping even in the hard x-ray range. This can be seen in figure 6.13, where the HT ICM structure and the intermediate ICM structure are indistinguishable. The overlap causes the apparent shift of the LT CM structure towards lower k with increasing temperature, until the HT ICM structure shifts everything towards higher k again. The higher sensitivity to the surface region is again apparent, in that we again see a trace of the commensurate structure up to 42 K.

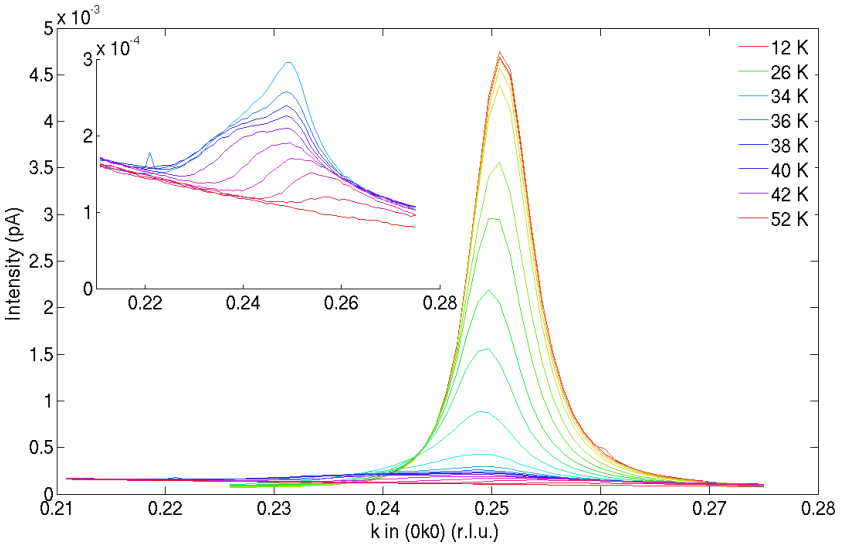

Figure 6.13: Temperature dependence of the F type (0 τ 0) reflection from $Eu_{0.8}Y_{0.2}MnO_3$ at the Mn L_2 absorption edge. The inset shows a blowup of the temperature range above 34 K.

In conclusion, the soft x-ray data supports our observations at the Mn K edge, apart from the difference noted above. The strong resonant signal gives confirmation that the weaker reflections observed at the Mn K edge are indeed of magnetic origin, and that their q-values can be trusted.

6.3 High field studies

The high field studies were performed using the 14 T cryomagnet in EH2 of beamline P09. The sample was mounted in horizontal scattering geometry with bc in the scattering plane, such that the vertical field direction was aligned along a, perpendicular to the scattering plane.

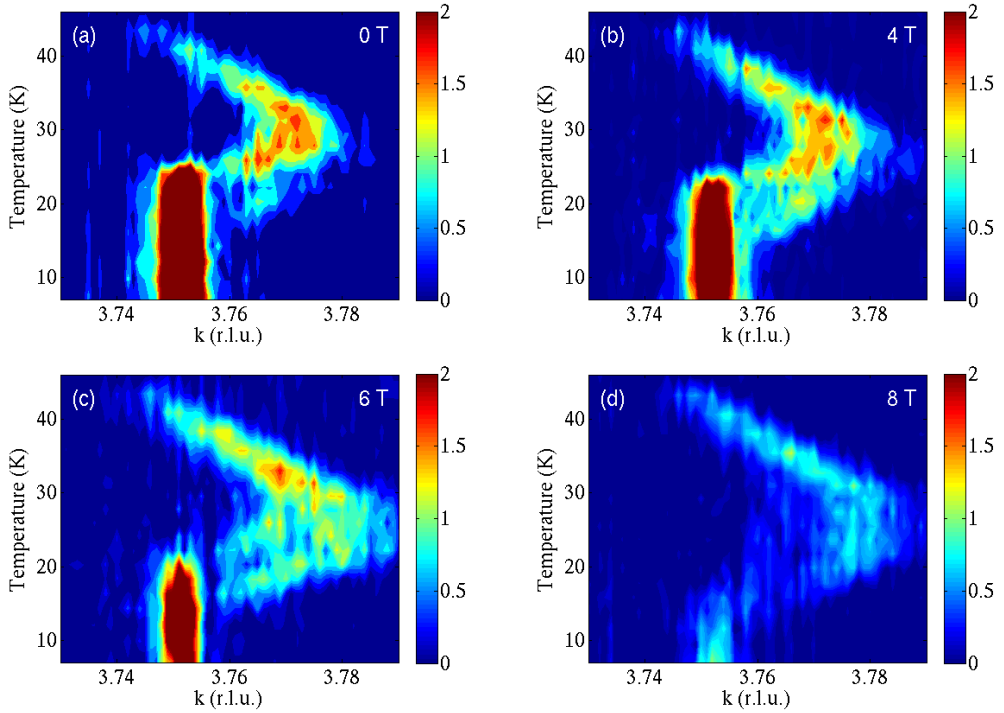

Figure 6.14: Temperature dependencies of the F type (0 4-τ 0) reflected intensities from $Eu_{0.8}Y_{0.2}MnO_3$ in π-σ' geometry measured in different magnetic fields applied along a: (a) 0 T (b) 4 T (c) 6 T (d) 8 T

Figure 6.14 shows temperature dependencies of the F type (0 4-τ 0) reflected intensities from $Eu_{0.8}Y_{0.2}MnO_3$ at different values of constant magnetic field along a. Similar measurements were made also of the A type magnetic structure, and the data look identical. For field values up to 4 T,

the behavior is unchanged. From 6 T and upwards, the low temperature commensurate structure is visibly suppressed, while the incommensurate structure above T_C is unchanged except for a minor intensity reduction under an applied magnetic field of 8 T. The suppression of the commensurate structure is clearly seen in the field dependence of the G type (0 3-τ 1) reflection at 4 K shown in figure 6.15.

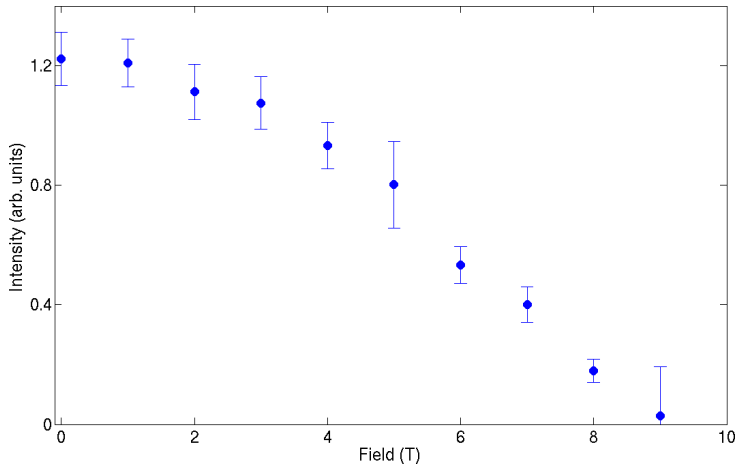

Figure 6.15: Magnetic field dependence of the G type (0 3-τ 1) reflected intensity from $Eu_{0.8}Y_{0.2}MnO_3$ at the Mn K absorption edge at 4 K, with magnetic field along a.

Figure 6.16 displays the integrated intensities and reciprocal space positions of the (0 4-τ 0) reflection as a function of temperature. Filled symbols represent the commensurate magnetic structure (CM), while open symbols represent the incommensurate magnetic structures (ICM). In the temperature region below T_C, one can see clearly the suppression of the CM structure with field, as well as what looks like a reduction of the transition temperature T_C. However, the 8 T data shows that the CM structure in fact persists up to T_C for all field values, but that it turns incommensurate at a field dependent transition temperature T^*, concomitantly with a sharp reduction in intensity. The ICM structure in the paraelectric phase above T_C is mostly unaffected by the magnetic field, apart from a slight intensity reduction at the highest field strength. This is also true for the intermediate ICM structure between T = 17 K and T_C from 0 to 6 T. With an applied field of 8 T however, a drastic change is seen. Just as the CM structure shifts towards higher q (lower τ) above T^*, the wave vector of the intermediate ICM structure also increases between T^* and T_C.

In order to see more clearly the difference between 0 and 8 T, we also

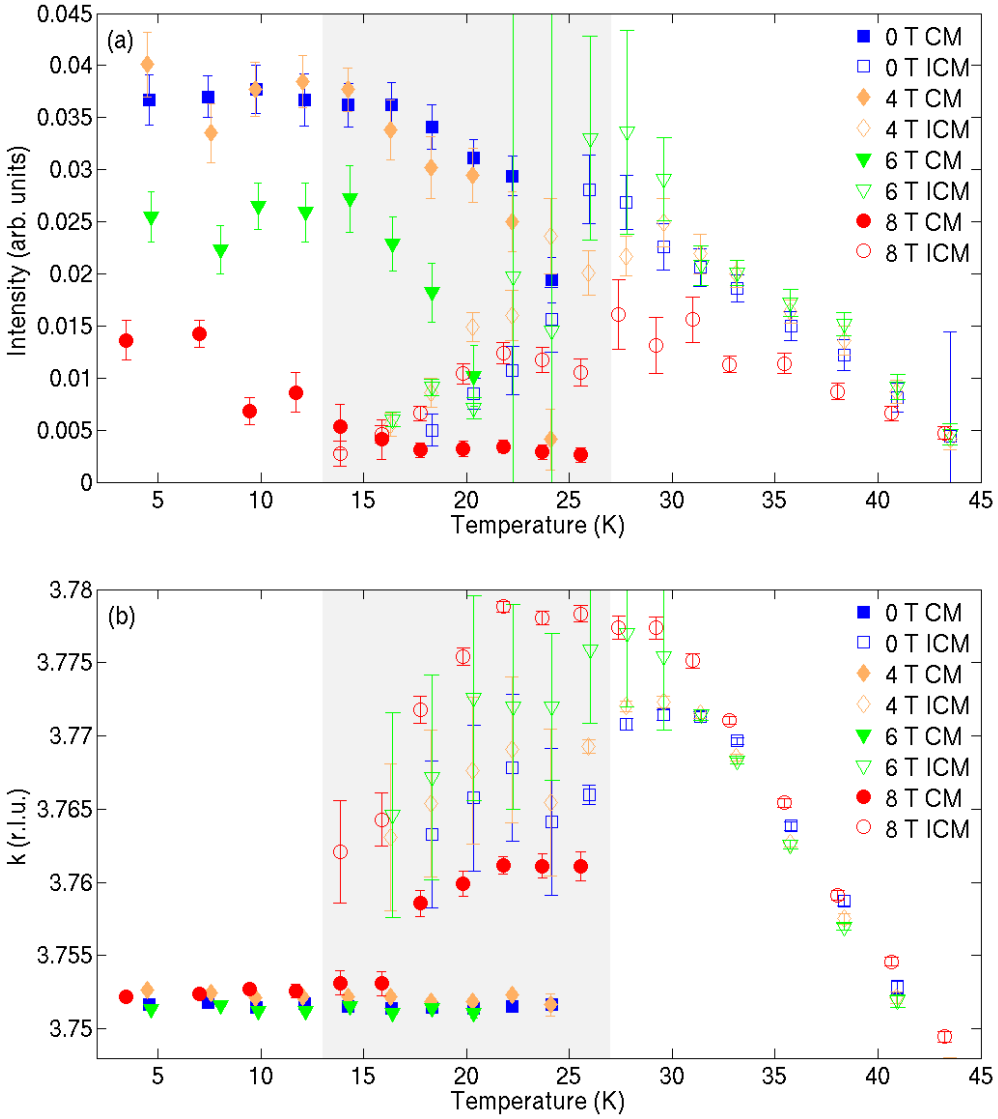

Figure 6.16: Temperature dependence of the integrated intensity (a) and position (b) of the F type (0 4-τ 0) magnetic reflection from $Eu_{0.8}Y_{0.2}MnO_3$ with different magnetic field strengths applied along a.

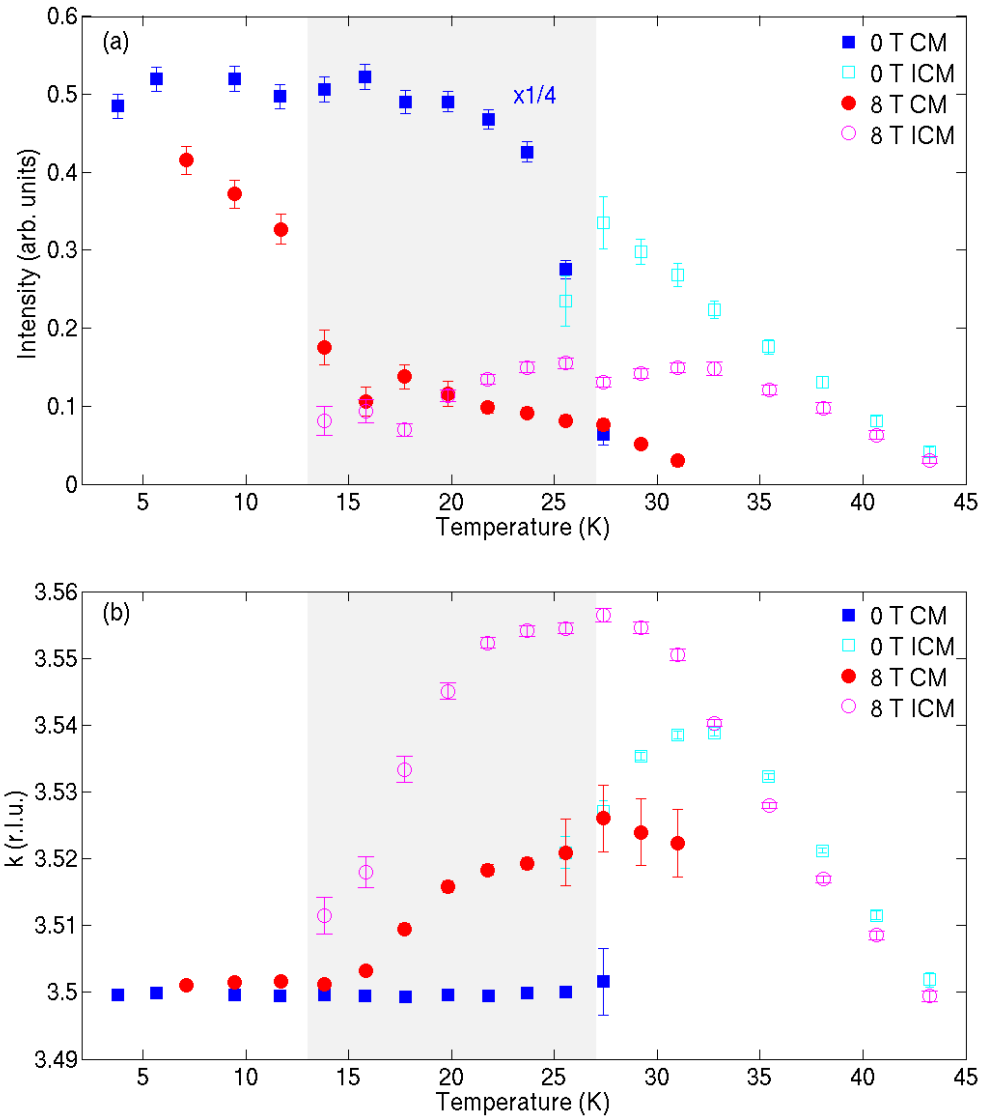

Figure 6.17: Temperature dependence of the integrated intensity (a) and position (b) of the (0 4-2τ 0) charge reflection from $Eu_{0.8}Y_{0.2}MnO_3$ with magnetic field along a. The intensity of the commensurate signal in zero field has been scaled by a factor 1/4.

measured the intensity and position of the magnetically induced (0 4-2τ 0) charge reflection, shown in figure 6.17. The same behavior of the structural intensities with field as observed at the magnetic reflection is confirmed here, with the addition that the sharp intensity reduction of the commensurate signal towards T^* under an applied field of 8 T is more clearly seen. The stronger signal also allows for the observation that T_C changes slightly towards higher temperatures with field.

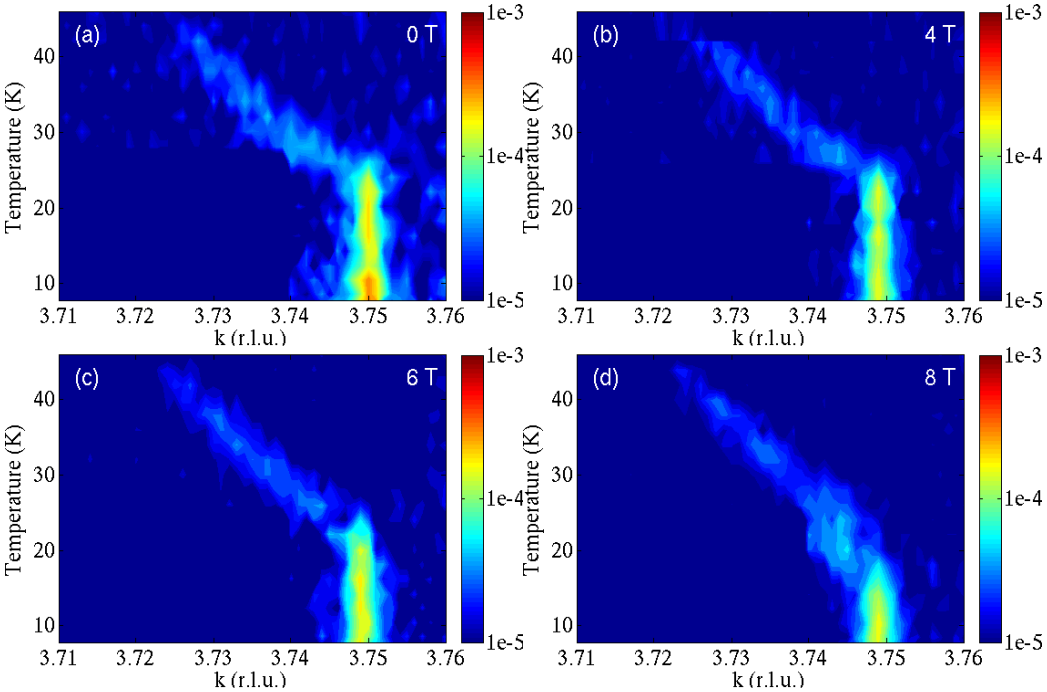

Figure 6.18: Temperature dependencies of the F type (0 4-τ 0) reflected intensities from $Eu_{0.7}Y_{0.3}MnO_3$ in π-σ' geometry measured in different magnetic fields applied along a: (a) 0 T (b) 4 T (c) 6 T (d) 8 T

$Eu_{0.7}Y_{0.3}MnO_3$ was also investigated under an applied magnetic field along a. Figures 6.18 and 6.19 show the temperature dependencies of the F type (0 4-τ 0) and the A type (0 4-τ 1) reflections, respectively. In this stoichiometry, at high fields, there is also an intermediate phase with an additional incommensurate phase as observed in $Eu_{0.8}Y_{0.2}MnO_3$. Figure 6.20 shows the integrated intensity and position of the A type (0 4-τ 1) as function of temperature and magnetic field. From these plots, it becomes apparent that the incommensurate wave vector associated with the paraelectric phase in high fields does not in fact lock into the commensurate value at T_C, but rather into the wave vector associated with the ICM structure appearing in parallel to the CM structure, like in $Eu_{0.8}Y_{0.2}MnO_3$. In contrast to

$Eu_{0.8}Y_{0.2}MnO_3$, this additional ICM structure appears at a higher value of τ compared to the commensurate position. Under a field of 10 T, the CM structure is fully suppressed down to 5 K, and is replaced by the ICM structure seen only in the intermediate phase at 8 T. This indicates that below a critical magnetic field strength of about 9 T, the CM and ICM orders coexist in the sample, possibly in different domains.

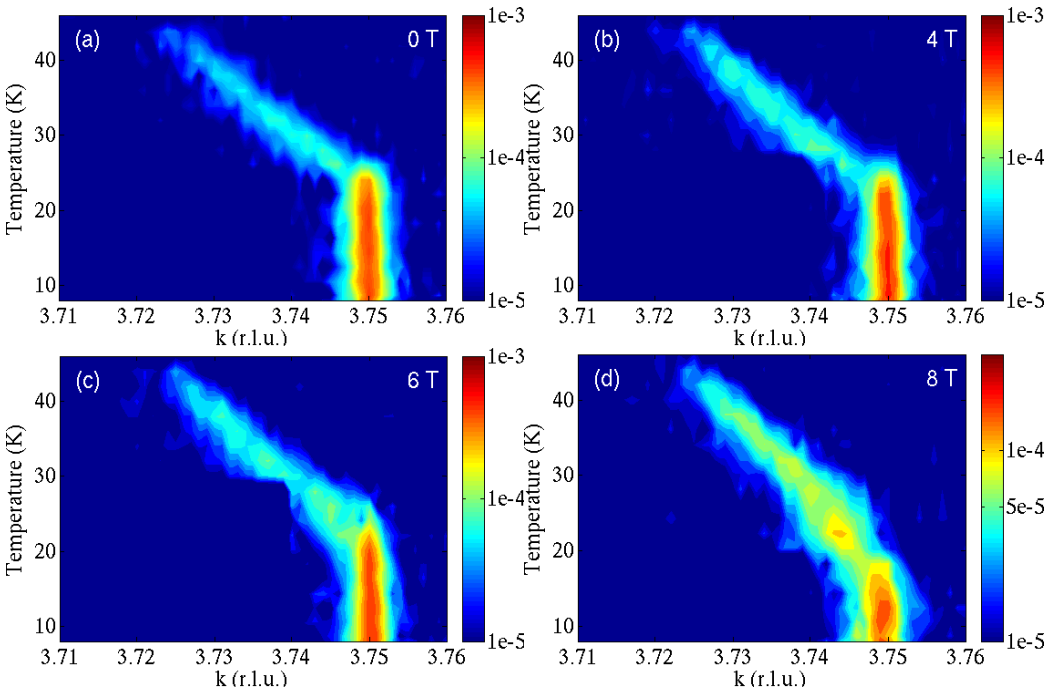

Figure 6.19: Temperature dependencies of the A type (0 4-τ 1) reflected intensities from $Eu_{0.7}Y_{0.3}MnO_3$ in π-σ' geometry measured in different magnetic fields applied along a: (a) 0 T (b) 4 T (c) 6 T (d) 8 T

6.4 Discussion

In both $Eu_{0.8}Y_{0.2}MnO_3$ and $Eu_{0.7}Y_{0.3}MnO_3$, we observe magnetic structures associated with the high temperature paraelectric (c sinusoidal) and the low temperature ferroelectric (ab cycloidal) phases previously observed for the compounds with $x > 0.2$. DM canting of the Mn magnetic moments in the FE phase has been confirmed by full polarization analysis. In addition, in the upper temperature range of the FE phase of $Eu_{0.8}Y_{0.2}MnO_3$, we clearly see a component of the weakly ferromagnetic phase normally associated with lower x. The presence of two competing wave vectors in the intermedi-

ate temperature region indicates that the sample forms a magnetoelectric glass state with coexisting WFM and FE phases as previously observed in $Eu_{3/4}Y_{1/4}MnO_3$ [50]. It should be noted that this coexistence was not found in other experiments on $Eu_{0.8}Y_{0.2}MnO_3$ [36, 102]. However, as we have seen in section 2.3, the phenomenology of the RMnO$_3$ system is extremely sensitive to the bond lengths and bond angles, so just a small change in doping level could have a large effect. The measurements allow us to construct an $H-T$ phase diagram, shown in figure 6.21. In contrast to $Eu_{3/4}Y_{1/4}MnO_3$, $Eu_{0.8}Y_{0.2}MnO_3$ displays the FE + WFM coexistence even in zero field.

In $Eu_{0.7}Y_{0.3}MnO_3$, the wave vector of the *ab* cycloid increases with increasing field. This can be understood in terms of the competition between nearest-neighbor J_1 and next-nearest-neighbor J_2 exchange interactions responsible for stabilizing the *ab* cycloidal structure. We saw in chapter 2 that a decrease of the RE ionic radii leads to an increase of J_2 compared to J_1, shifting the system out of the AFM(A) + WFM phase. A similar effect is achieved with the application of a magnetic field along a, within the spin rotation plane and perpendicular to the propagation vector. Increasing the field strength enhances the a components of the spin spiral at the expense of the b component. This in turn leads to an increase of J_2 compared to J_1, which is responsible for the polarization flop in $Eu_{0.6}Y_{0.4}MnO_3$ as the spin rotation angle increases above a critical value (cf. section 2.3). While we do not observe a spin flop transition in either of our compounds, the field-induced strengthening of J_2 is clearly seen in $Eu_{0.7}Y_{0.3}MnO_3$, where the spin rotation angle of the cycloid in the mixed phase is seen to increase at the highest field strength.

Remarkably, the opposite is true for $Eu_{0.8}Y_{0.2}MnO_3$ where the spin rotation angle of the commensurate cycloid *decreases* at the highest field strength in the mixed phase. In the same temperature and field region, also the wave vector of the magnetic structure associated with the WFM phase decreases. This suggests an important role of the mixed-in WFM phase for stabilizing the cycloid in this temperature region. It is supported by previous observations on $Eu_{0.8}Y_{0.2}MnO_3$ made by Danjoh *et al.* with an applied magnetic field along c, perpendicular to the spin rotation plane [49]. They observed an extinction of the ferroelectric phase at low temperatures as the cycloidal magnetic structure was destroyed under an applied magnetic field. However, in the intermediate temperature range $T^* < T < T_C$, a reduced ferroelectric polarization remained even after field cooling (see figure 6.1). This strongly points to a magnetoelectric interaction between the two subsystems.

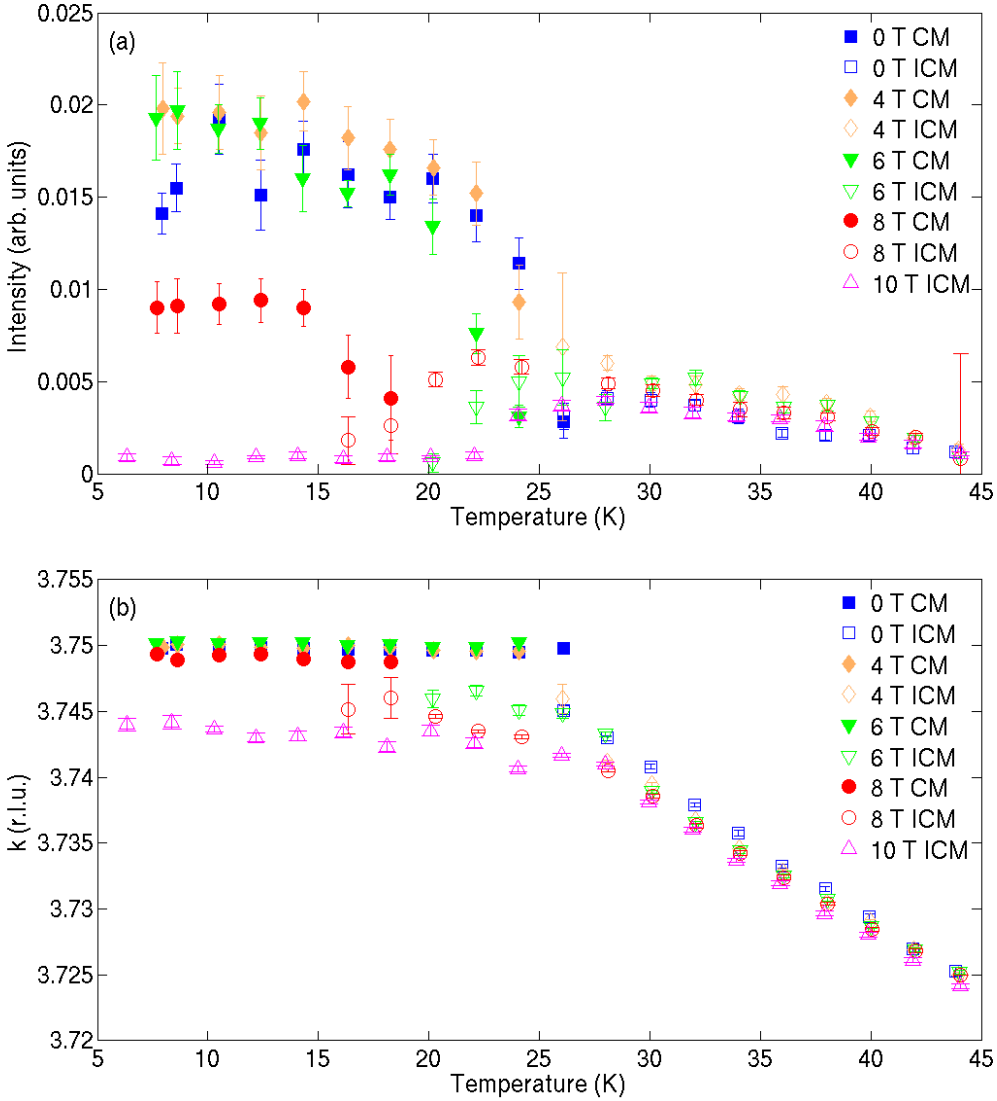

Figure 6.20: Temperature dependence of the integrated intensity (a) and position (b) of the (0 4-τ 1) magnetic reflection from $Eu_{0.7}Y_{0.3}MnO_3$ with magnetic field along a.

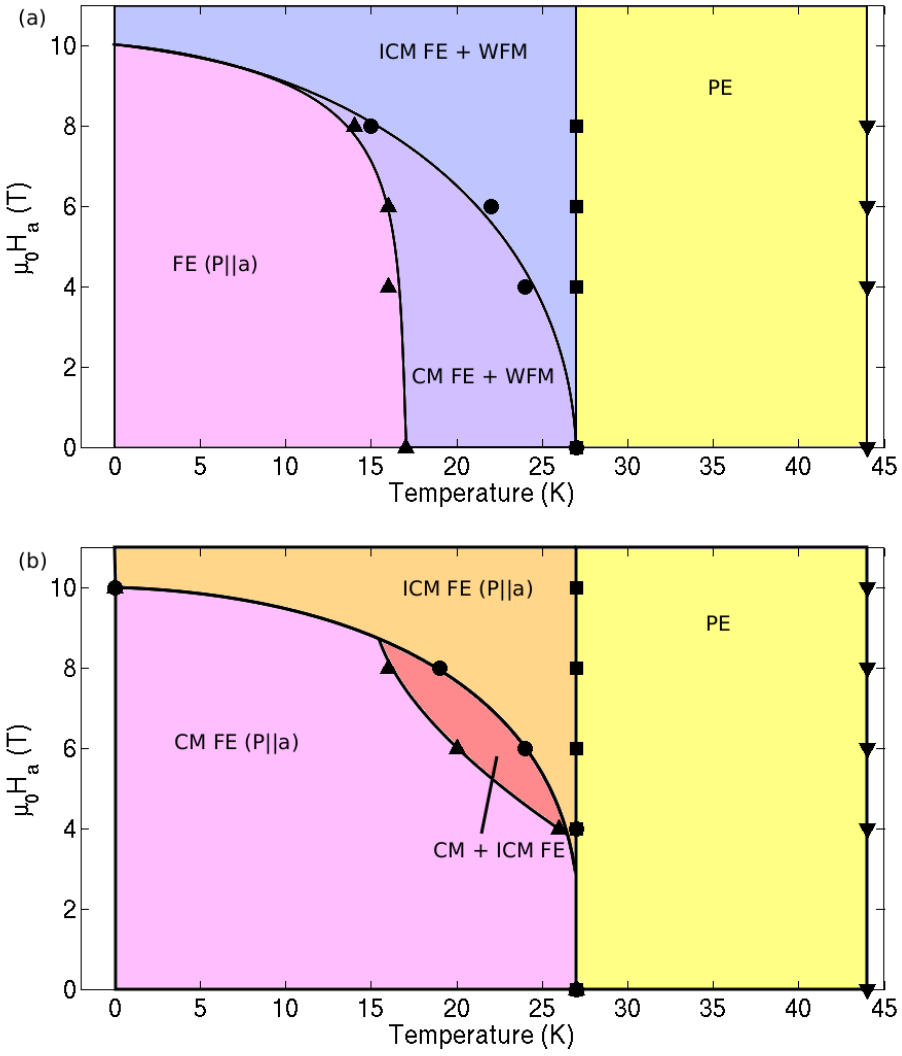

Figure 6.21: H-T phase diagrams of (a) $Eu_{0.8}Y_{0.2}MnO_3$ and (b) $Eu_{0.7}Y_{0.3}MnO_3$ as obtained from our REXS measurements. In $Eu_{0.8}Y_{0.2}MnO_3$, the WFM and FE phases coexist for $\sim T^* < T < T_C$. In this temperature range, there is a phase transition within the ferroelectric phase, where the magnetic structure changes from CM to ICM. Application of field reduces this transition temperature.

Chapter 7

Van Vleck antiferromagnetic order of Eu^{3+} in $Eu_{1-x}Y_xMnO_3$ without an externally applied magnetic field

7.1 Scientific case

The interplay between local spin and orbital magnetic moments is an important factor in a large variety of magnetic ordering phenomena exploited in present day applications. In special cases, even with magnetic moments present, a system can form a non-magnetic singlet ground state. Prominent examples are rare earth and transition metal ions with the f or d shell missing one electron for half filling. Here the orbital and spin moments can cancel out generating a $J = 0$ ground state. However, having only a small energy spacing between the ground state and the first magnetic triplet state, such systems can nevertheless be susceptible to magnetic stimulus. This is known as Van Vleck magnetism and offers fascinating possibilities for new applications, for example for a magnetic sensor that is itself non-magnetic. From a more fundamental point of view such systems are candidates for a variety of novel states of matter characterized by hidden order [3], Bose-Einstein condensation or quantum phase transitions [4, 5]. One example of a formally non-magnetic ion being susceptible to external magnetic fields is the Eu^{3+} ion with $S = 3$ and $L = 3$, having a $J = 0$ non-magnetic ground state.

Van Vleck magnetism has long been known to contribute to the paramagnetic moment of Eu^{3+} [105, 106, 107]. For this ion, the symmetry breaking by an external magnetic field mixes the $^7F_1$ state into the ground state, yielding

a finite magnetic moment. A more recent example of this mechanism is the observation of x-ray magnetic circular dichroism (XMCD) in EuN under an applied magnetic field of 5 T, which is explained by magnetic field induced admixture of $^7F_1$ into the $^7F_0$ ground state [108]. The possibility of spin ordering without external magnetic fields in the case of a vanishing total magnetic moment has been discussed theoretically, setting up the possibility of an unconventional phase transition in which the spin correlation length diverges but there is little or no change in the magnetic properties [109].

While these previous studies revealed the presence of Van Vleck magnetic moments, experimental proof of magnetic order connected with Van Vleck magnetism due to exchange coupling is missing. Rare earth (RE) manganites are well-suited candidates to show such a mechanism. As in $Eu_{1-x}Y_xMnO_3$, in many other perovskite-like $3d$ transition metal compounds such as manganites, nickelates and cuprates, Eu^{3+} ions are often used as a nonmagnetic RE substitute. In the previous section, we assumed no RE magnetism in the sample, as the $J = 0$ ground state of Eu^{3+} is non-magnetic and its spherical symmetry has no crystal field splitting. However, exchange coupling between Mn $3d$ and RE $4f$ states is an interaction between spins and does not involve the orbital moment L, and may hence induce a Van Vleck $J = 1$ magnetic moment in Eu^{3+}. As a consequence, Eu^{3+} might not be anticipated as a completely nonmagnetic reference ion in exchange coupled materials, but displays a perfect candidate for long range antiferromagnetic order originating from Van Vleck magnetism.

We have looked for Van Vleck type Eu^{3+} ordering in $Eu_{1-x}Y_xMnO_3$ using resonant elastic x-ray scattering (REXS) at the Eu $M_{4,5}$ and $L_{2,3}$ edges. REXS is particularly suited for this purpose by virtue of element specificity, high sensitivity to detect even weak antiferromagnetic ordering of Eu $4f$ moments, and spectroscopic information for identifying the J state involved in the ordering.

7.2 Experiment

The experimental setup for measuring the REXS signal at the Eu edges was the same as described in the previous section. The scattering experiments at both PETRA III and BESSY II were carried out in horizontal geometry from the b surface of the sample, at PETRA III with a perpendicular to the scattering plane, and at BESSY II with c perpendicular to the scattering plane, unless otherwise noted. In order to reduce the reflectivity background at low scattering angles, a vertical miscut of ca. 3° was introduced to the b surface of the samples. This deflects the reflectivity photons vertically out

of the scattering plane, away from the detector in the horizontal scattering plane.

$Eu_{0.8}Y_{0.2}MnO_3$ and $Eu_{0.7}Y_{0.3}MnO_3$ were investigated at low temperatures in the ferroelectric phase. As we saw in the previous section, magnetic reflections of A, F, G and C types were all observed at the Mn K edge. In contrast, at the Mn $L_{2,3}$ edges only the F type reflection is accessible within the limited size of the Ewald sphere at this photon energy. Remarkably, intense resonant F and C type reflections could be observed in both samples at the Eu $M_{4,5}$ edges as well, although the F type reflection occurs at a very low scattering angle and suffers from a substantial reflectivity background.

The resonant behavior of the magnetic reflection from $Eu_{0.8}Y_{0.2}MnO_3$ at the Eu^{3+} $M_{4,5}$ absorption edges is demonstrated in figure 1. The results from $Eu_{0.7}Y_{0.3}MnO_3$ look identical, and in the following we will concentrate on $Eu_{0.8}Y_{0.2}MnO_3$, unless otherwise noted. The inset of figure 7.1(a) shows a reciprocal space scan over the (0 1-τ 0) reflection at $T = 10$ K with π and σ incident polarization, respectively, and the photon energy tuned to 1127 eV, close to the Eu M_5 absorption edge. The absence of intensity for σ incident light indicates that this reflection is caused by magnetic scattering from the formally non-magnetic Eu^{3+} ions with the corresponding moments pointing along the c direction, i.e. moments parallel to the Mn moments as observed at the Mn K edge resonance. Resonant enhancement at formally non-magnetic anions has been observed in earlier studies and mainly been attributed to transferred moments in hybrid orbitals [111, 112, 113]. In contrast to these former observations however, the Van Vleck ion Eu^{3+} has the possibility to create a magnetic moment in the core-like $4f$ shell by populating the magnetic $^7F_1$ excited state.

The absorption corrected photon energy dependence of the C type magnetic reflected intensity is shown in figure 7.1(a) and can be readily explained by considering the resonant magneto-optical parameters connected with a $^7F_1$ state. One can calculate the expected $^7F_1$ REXS magnetic lineshape from the XMCD data of paramagnetic Eu^{3+} using the Kramers-Kronig relations [114]. The result of this calculation, based on the XMCD data taken from Ref. [108], is shown as red curve in figure 7.1(a) (see Appendix B) [110]. Comparison to the measured REXS lineshape (blue curve) yields a good match, apart from a relative difference in intensities between the M_4 and M_5 edges and a small offset in photon energy. This result shows that the peak observed at the Eu $M_{4,5}$ edges is indeed of magnetic origin caused by a populated $^7F_1$ state. To clarify the mechanism populating the $^7F_1$ state we performed x-ray absorption spectroscopy (XAS) at different temperatures by measuring the total electron yield (TEY) (figure 7.1(b)). We then compared the TEY data to single ion atomic multiplet calculations of the relevant electronic

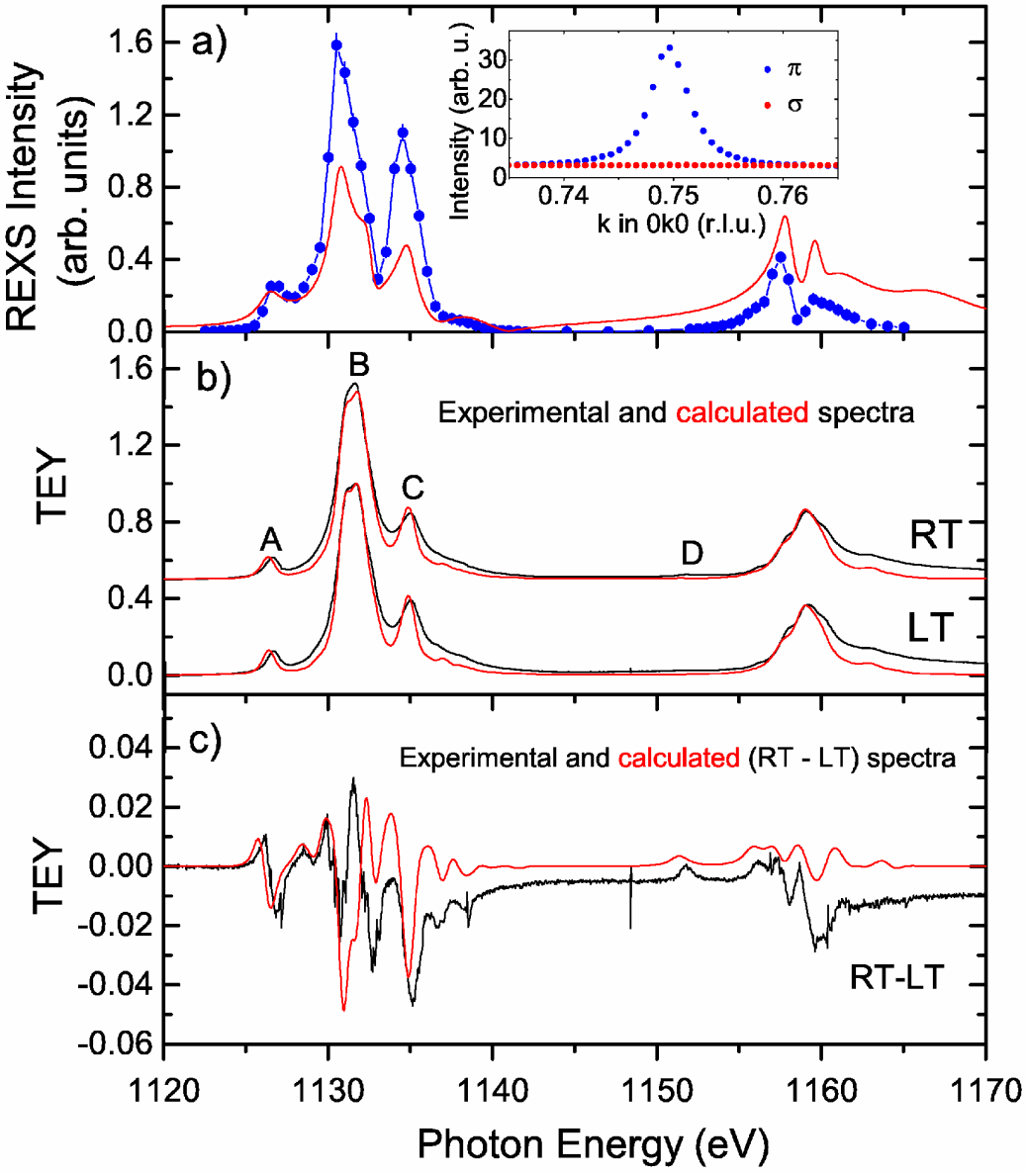

Figure 7.1: (a)Absorption corrected REXS spectrum (blue curve) of (0 1-τ 0) across the Eu M_5 and M_4 edges at $T = 10$ K, and lineshape calculation [110] (red curve) based on XMCD spectrum from [108]. The inset shows reciprocal space scans of the reflection for π and σ incident polarization. (b) Experimental TEY spectra and multiplet calculations at $T = 296$ K (RT) and $T = 120$ K (LT). (c) Measured and calculated difference between high and low temperature spectra.

J	E_J (meV)	T_J (K)
0	0	0
1	53.1	616
2	144.8	1680
3	261.1	3030
4	392.2	4551

Table 7.1: Relative energies of the J levels in Eu f^6 ^7F_J ion calculated using Cowan [115, 117]. The relative energy in meV is converted to Kelvin scale using $kT(300\text{K}) = 25.85\text{meV}$.

states [115, 116].

The relative energies of the different J levels can be calculated using Cowan's code [117]. The results are given in table 7.1 and are in reasonable agreement with experimental values by Gruber *et al.* [118], which are $\sim 20\%$ smaller. Assuming Boltzmann population of the different J levels, this yields the population distribution across the J levels at 120 K and 296 K shown in table 7.2. Thus the LT spectrum is expected to correspond to almost purely $^7F_0$, while the RT spectrum should contain a considerable amount of $^7F_1$. To obtain the temperature dependent x-ray absorption spectrum $I(T)$, the J levels are summed over the calculated spectra I_J weighted by their Boltzmann factor and divided by the partition function:

$$I(T) = \frac{\sum_J I_J(2J+1)\exp(-E_J/kT)}{\sum_J (2J+1)\exp(-E_J/kT)} \tag{7.1}$$

To find the spectra I_J, the electric dipole transitions $4f^6 \rightarrow 3d^9 4f^7$ were calculated using atomic multiplet theory. In the lanthanide series, the $4f$ wave function contracts gradually with increasing ionization, making these orbitals atomic-like, with negligible influence on the local environment. Multiplet calculations are well suited to describe transitions from core states into localized states such as the $4f$ [119]. In Eu, the $4f$ electrons are not directly

J	120 K (LT)	296 K (RT)
0	98.3%	71.9%
1	1.7%	26.9%
2	0	1.2%
3	0	0

Table 7.2: Population distribution of the different J levels in Eu f^6 ^7F_J using the relative energy levels in table 7.1

involved in the chemical bonding, implying that the Eu $M_{4,5}$ spectrum is essentially the same for the $Eu_{1-x}Y_xMnO_3$ oxide as for Eu metal. Also, the additional $4f$ electron in the final state is very efficiently screening the $3d$ hole, so that the chemical shift in the $M_{4,5}$ spectrum is small [115].

In the multiplet calculations, spin-orbit and electrostatic interactions, such as $3d-4f$ and $4f-4f$ Coulomb and exchange interactions, are treated on an equal footing [117, 116, 119]. The wave functions of the initial and final state were calculated using Cowan's atomic Hartree-Fock (HF) code with relativistic corrections [117]. To account for lifetime broadening and instrumental broadening, the line spectra were broadened by a Lorentzian of $\Gamma = 0.3(0.6)$ eV for the $M_5(M_4)$ peak and a Gaussian of $\sigma = 0.25$ eV, respectively. Saturation effects for total electron yield were taken into account using the approach described in Ref. [116], assuming an electron escape depth of 3 nm and normal incidence of the x-ray beam.

Figure 7.1(b) shows the x-ray absorption spectra across the Eu $M_{4,5}$ edges at two different temperatures, 296 K (RT) and 120 K (LT). The spectra are normalized such that the integrated intensity of the difference spectrum in figure 7.1(c) is perceived to be as small as possible. Due to the sample being ferroelectric and thus insulating at low temperatures, 120 K was the lowest temperature we were able to measure TEY spectra without encountering charge buildup on the surface.

These spectra are now compared to the multiplet calculations [115]. There are some significant differences between the RT and LT spectra seen in the experiment which are fully confirmed by the calculation:

- The first peak A (at 1126.5 eV) is slightly lower for RT.
- The low-energy shoulder of the main peak B (at 1131.5 eV) is lower for RT.
- The peak C (at 1135 eV) is much lower for RT.
- A small additional peak D (at 1151 eV) appears for RT.

There is a one-to-one relation for each peak between experiment and calculation. There are also some minor differences between the experiment and the calculation: Peak A and C are seen to be shifted to slightly different energies. The calculated peaks are convoluted with symmetric line shapes, whereas the experiment shows asymmetric peaks. In the experiment there is a small continuum background above each edge. These differences can be due to interactions and many-body effects that are not included in the atomic calculation.

Considering now the (RT-LT) difference spectra shown in figure 7.1(c), there is an excellent agreement between experiment and calculation, taking into account the aforementioned small peak shifts, asymmetric line shapes, and continuum background not included in the calculation. Furthermore, the magnitudes of the experimental and calculated differences are in good agreement with each other. The maximum difference is ~ 5 %. The magnitude of the difference spectrum scales with the percentage of higher J population. Thus thermal population of $J \neq 0$ states can not explain the resonant signal at 10 K. The TEY spectra show that the population of the $^7F_1$ state at RT

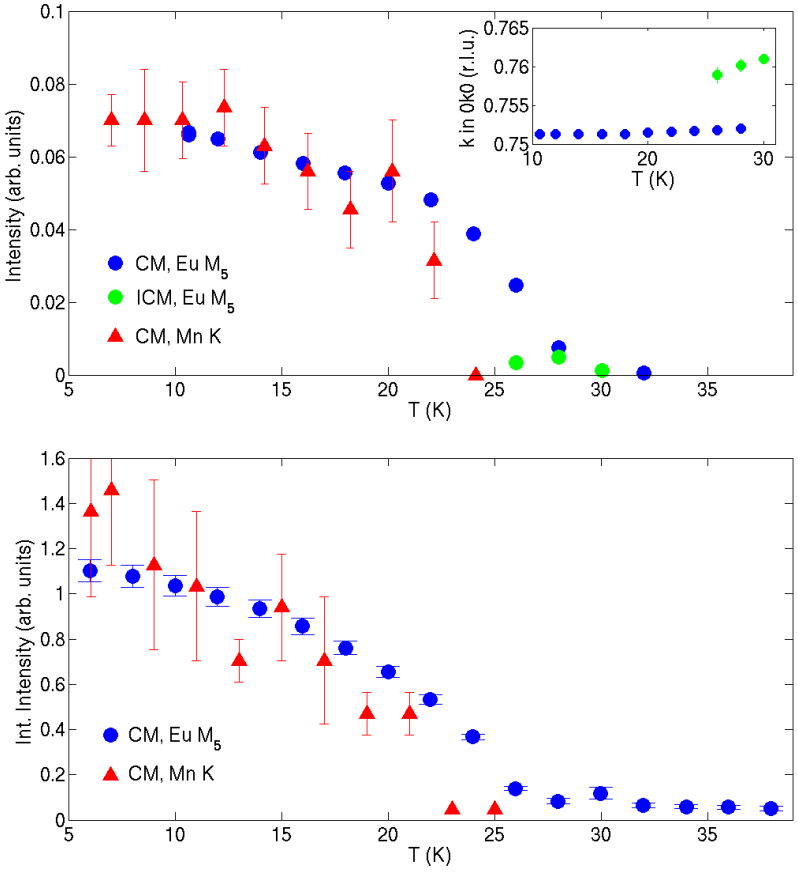

Figure 7.2: (a) Temperature dependence of the integrated intensity of the C type (0 1-τ 0) reflection from $Eu_{0.8}Y_{0.2}MnO_3$ at the Eu M_5 resonance (blue and green circles). The inset shows the peak positions in q-space over the same temperature range. Red triangles show the T dependence of the C type (0 3+τ 0) reflection at the Mn K edge. The data has been scaled to fit onto the same plot. (b) Same as (a), for $Eu_{0.7}Y_{0.3}MnO_3$.

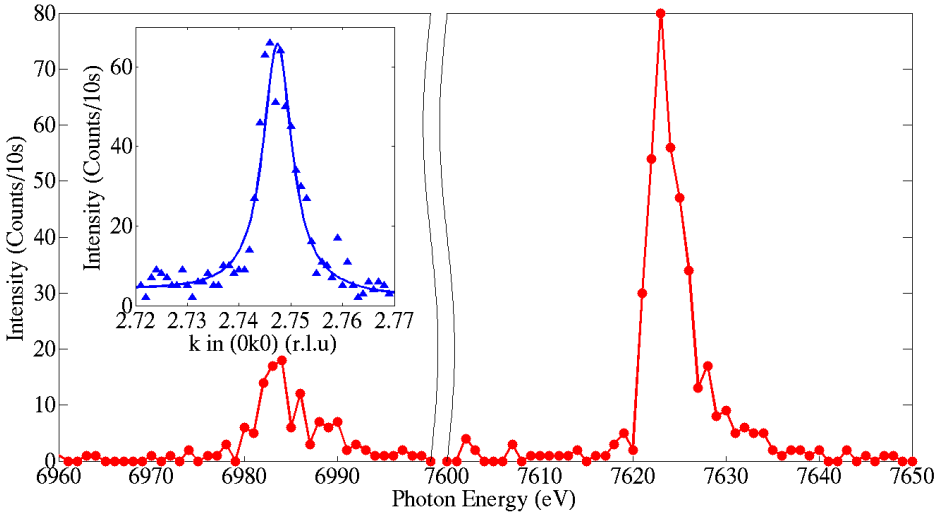

Figure 7.3: Energy dependence of the peak intensity of the C type reflection (0 3-τ 0) reflection across the Eu $L_{2,3}$ edges in the σ-π' channel. The inset shows a reciprocal space scan in the σ-π' channel along with a Lorentzian fit.

is not larger than expected from the Boltzmann distribution, so there is also no reason to expect hybridization or crystal fields to cause magnetic order.

The negligible influence of the temperature on the $^7F_1$ population is also reflected in the observed temperature dependent peak intensity. The temperature dependence of the C type reflection (0 1-τ 0) was measured both at the Mn K edge and at the Eu M_5 edge, and is shown in figure 7.2. Apart from smaller error bars for the much stronger signal at the Eu M_5 absorption edge, we observe a perfect match of the temperature dependent peak intensities, disappearing at the transition into the paraelectric phase. This behavior is in accordance with the proposed magnetic structure; the behavior of the Eu^{3+} ions, in particular, reflects that of the corresponding order parameter. This strongly points to a population of the $^7F_1$ state independent of temperature and strength of possible internal dipole fields, and indicates a strong coupling between the Mn and the Eu^{3+} magnetic order.

Using the stronger signal at the Eu M_5 resonance, we are also able to resolve an incommensurate structure in $Eu_{0.8}Y_{0.2}MnO_3$ existing in parallel to the the commensurate one close to the transition temperature. We can associate this with the intermediate incommensurate structure seen in the A, F and G type Mn magnetic structures. In addition, A, C, F and G type reflections were also observed at the Eu $L_{2,3}$ edges, with the A and G type reflections appearing only in the ferroelectric phase, this time in vertical scattering geometry with *bc* in the scattering plane. The energy dependence of

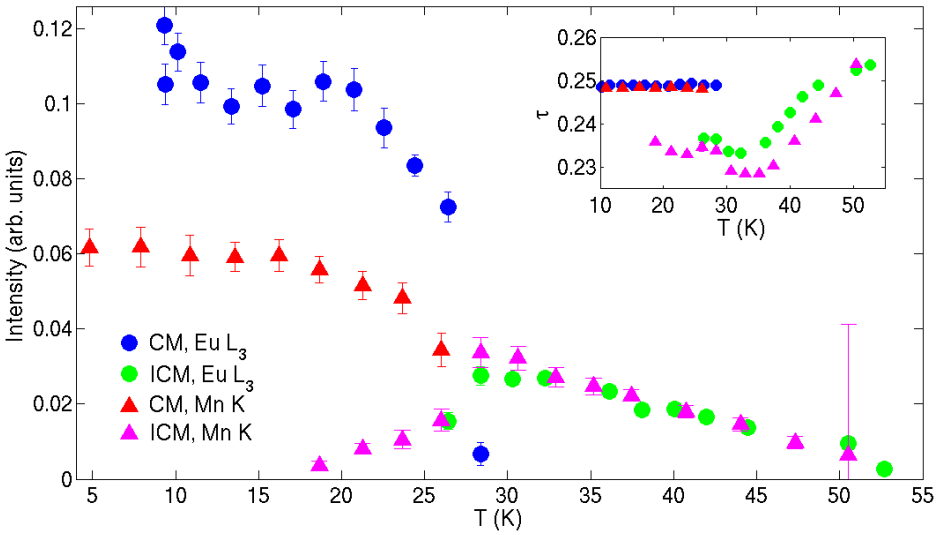

Figure 7.4: Temperature dependence of the integrated intensity of the F type (0 2-τ 0) reflection at the Eu L_3 absorption edge (blue and green circles). The inset shows the peak positions in q-space in the same temperature range. Red and magenta triangles show the temperature dependence of the F type (0 4-τ 0) reflection at the Mn K edge. The data has been scaled to fit onto the same plot.

the C type reflected intensity is shown in figure 7.3. The signal is only present in the σ-π' channel, confirming that the magnetic moments are constrained to the bc crystallographic plane. Since these resonances do not directly probe the induced $4f$ states, but rather the $5d$ electrons, we do not gain a noteworthy signal enhancement compared to the Mn K edge resonance. Nonetheless, it allows to compare all relevant reflections from Eu^{3+} with those observed at the Mn K edge. Figure 7.4 shows the temperature dependencies of the F type reflections (0 2-τ 0) and (0 4-τ 0) at the Eu L_3 and Mn K edge absorption edges, respectively. The commensurate and incommensurate phases are recognized in both temperature spectra, and match the phase transitions observed elsewhere [35, 36, 37]. At the Mn K edge, the intermediate ICM structure was slightly better resolved than at the Eu L_3 edge, allowing us to track the reflection down to $\sim$ 19 K. The only other major difference in the data is the relative difference in intensity between the CM and the ICM reflections, being slightly larger at the Eu L_3 edge.

We thus observe a common behavior of the magnetic reflections both at the Mn K edge and the Eu absorption edges when it comes to the intensity- and **q**-dependence with varying temperature and photon polarization along

with an order parameter-like behavior of the Eu magnetic order. Hence the Eu resonant reflections are caused by magnetic order of the Eu^{3+} moments which mirrors the magnetic structure of Mn moments.

7.3 Discussion

Our results clearly show that the magnetic moment at the Eu site is caused by a populated $^7F_1$ state, the same state which is responsible for the paramagnetic Van Vleck magnetism caused by external magnetic fields in other Eu^{3+} compounds. However, in contrast to all former studies we do not observe paramagnetic behavior in an external magnetic field, but long range antiferromagnetic order without external stimulus. Our XAS data show that thermal population of $J = 1$ is negligible at 10 K. Since the $4f$ shell in Eu^{3+} is essentially core-like, crystal field effects are expected to be weak but might slightly modify the magnetic behavior as observed for the paramagnetic response of Eu_2CuO_4 [120]. However, an internal exchange field set up by the Mn can not be neglected, since it exists in all other $R\mathrm{MnO}_3$ compounds, where ordering of the RE ions is induced by the Mn order [93, 52]. The exchange field of the Mn moments causes a local symmetry breaking that, similar to the symmetry breaking caused by an external magnetic field, results in a population of the $^7F_1$ state. Within this scenario, even details of the Eu^{3+} behavior resemble that of $R\mathrm{MnO}_3$ compounds with formally magnetic RE ions. For example, since the Eu in the *Pbnm* space group is located on the crystallographic mirror perpendicular to the *c*-axis, an exchange field from the Mn will be totally canceled out if the Mn magnetic structure is A type or G type. And indeed, in the paraelectric phase we only observe the F type ordering at the Eu absorption edges. At the onset of ferroelectricity however, spatial inversion symmetry is broken, which allows us to observe also the A and G type ordering (see figure 7.5). This behavior strongly supports the symmetry breaking mechanism by exchange coupling and hence a Van Vleck mechanism as the cause of the observed Eu^{3+} magnetic order.

Exchange coupling between Eu and Mn spin moments offers an explanation for the mirroring capability of the Eu spin order. In our experiment, we see clear evidence of exchange coupling between Eu and Mn moments. In contrast with the spin polarization observed in oxygen in similar multiferroics, which is caused by spin dependent hybridization [112, 113], the magnetic moment on Eu in our case is dependent on a broken symmetry by non-zero local exchange fields. As soon as the magnetic Eu state is induced, Eu-Mn and Eu-Eu exchange coupling as well as Eu magnetic anisotropy can contribute to the magnetic order of the entire system with the possibility

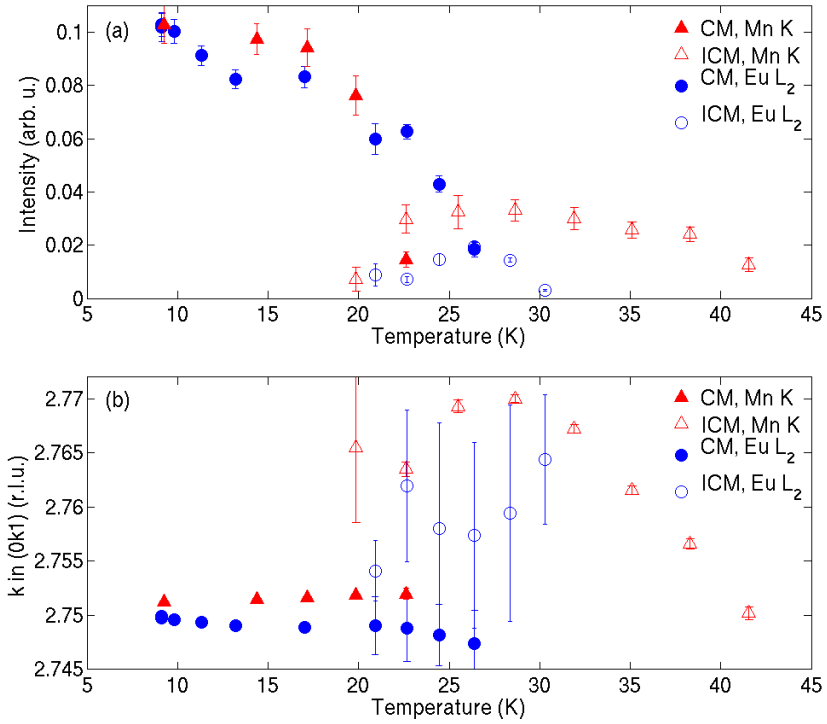

Figure 7.5: Temperature dependence of the integrated intensity (a) and the reciprocal space position (b) of the G type (0 3-τ 1) reflection at the Mn K and Eu L_2 absorption edges in σ-π' scattering geometry. Below T_C at the Eu L_2 edge, the magnetic structures associated with the FE and WFM phases are observed, but the sinusoidal structure observed at the Mn K edge in the PE phase is absent.

of an indirect impact on the field-dependent multiferroicity. Furthermore, as we saw in chapter 5, similar RE magnetic structures have been shown to contribute directly to ferroelectricity in $R\mathrm{MnO_3}$ (R = Tb, Dy, Gd) by symmetric exchange striction mechanisms [23, 22, 18, 93, 52, 53, 101].

Besides this possible impact on multiferroicity, the existence of a non-zero Eu magnetic moment in $\mathrm{Eu_{1-x}Y_xMnO_3}$ raises a couple of issues. Firstly, it puts into question the assumption of $\mathrm{Eu_{1-x}Y_xMnO_3}$ being a model system for multiferroic orthomanganites free from RE magnetism. Secondly, the discovery of a Eu magnetic moment without self-ordering opens up the possibility of using Eu as a magnetic probe. By measuring the magnetic order of Eu, we indirectly measure the magnetic order of Mn through hybridization. This is analogous to $\mathrm{TbMnO_3}$, where Tb moments are clamped to the Mn moments above the ordering temperature of Tb [93, 121]. As seen in figure 5.1, by mak-

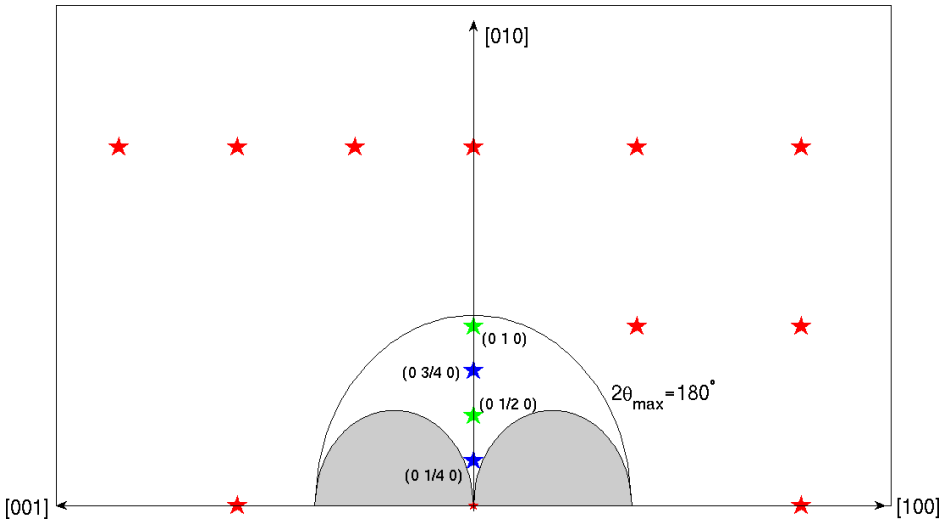

Figure 7.6: Reciprocal lattice of $Eu_{1-x}Y_xMnO_3$ with Ewald sphere at the Eu M_5 edge. Red stars denote structural Bragg reflections, blue stars magnetic reflections, and green stars selected forbidden reflections.

ing use of the strong resonant enhancement at the Eu $M_{4,5}$ edges we gain a drastically stronger signal from which we are able to extract intensities and q-values to much higher precision than what is possible at the Mn K edge. The onset of the ferroelectric phase below ~ 28 K is clearly seen. Measuring at the Eu M edges also has the added benefit of being able to explore a larger Ewald sphere compared to the Mn $L_{2,3}$ edges, where detailed studies of Mn magnetism are usually performed. Figure 7.6 shows the available reflections at the Eu M_5 edge. Comparing with figure 6.10, we see a big improvement going from the Mn K edge to the Eu M_5. In our experimental setup, only one F type magnetic reflection is reachable at the Mn L_2 edge, while at the Eu M_5 edge, both an F and a C type can be studied. In compounds with larger unit cells, the advantage would be even more pronounced.

Thirdly, our findings may have implications for magnetism in transition metals. Van Vleck effects are expected to appear in Eu, but not so much in $3d$ transition metals, where the orbital moment is usually quenched. There are however Van Vleck materials where exchange coupling plays a role and antiferromagnetic order in a field is associated with Bose-Einstein condensation of magnons [5]. More significantly, the increasing spin-orbit interaction in $4d$ and $5d$ transition metals renders Van Vleck effects more important in this class of materials that are increasingly attracting interest [122].

Chapter 8

Summary and outlook

The aim of this thesis was to shed light on the magnetic ordering responsible for ferroelectricity in multiferroic $R\mathrm{MnO_3}$, and to investigate the role of the rare earth magnetism by performing x-ray scattering experiments on compounds of $\mathrm{Eu_{1-x}Y_xMnO_3}$. These compounds have the same crystal structure as other multiferroic perovskites, and presumably no rare earth magnetism, since the ground states of $\mathrm{Eu^{3+}}$ and $\mathrm{Y^{3+}}$ both are non-magnetic.

In $\mathrm{TbMnO_3}$, the first direct measurement of a c component to the Tb moment direction below T_N^{Tb} was performed. Additional components to the Mn magnetic structure, predicted to occur due to magnetic moment canting induced by the Dzyaloshinskii-Moriya interaction, were confirmed in both $\mathrm{TbMnO_3}$ and $\mathrm{Eu_{1-x}Y_xMnO_3}$, in the latter case using the novel method of full polarization analysis. Canting of this type will have to be taken into account when describing multiferroicity in new compounds, since the additional moment components could in principle enable additional exchange interactions, both symmetric and anti-symmetric.

An example of how the symmetric exchange interaction is important to a complete understanding of ferroelectricity in $R\mathrm{MnO_3}$ compounds was observed in $\mathrm{GdMnO_3}$, where the Gd and Mn moments order with the same wave vector. Here, the symmetric exchange interaction between Gd and Mn moments was confirmed to strongly influence the ferroelectricity through a shift of the Gd ions when a b component to the Gd spin was induced by an applied magnetic field.

The importance of the competition between nearest-neighbor and next-nearest neighbor exchange interaction for stabilizing the cycloidal spin state was confirmed in $\mathrm{Eu_{0.8}Y_{0.2}MnO_3}$ and $\mathrm{Eu_{0.7}Y_{0.3}MnO_3}$. In $\mathrm{Eu_{0.8}Y_{0.2}MnO_3}$, which sits at the threshold between the ferroelectric and the weakly ferromagnetic ground states of the $\mathrm{Eu_{1-x}Y_xMnO_3}$ series, the coexistence of both phases was identified. Moreover, a magnetoelectric coupling between the two

subsystems was established. The possibility to fine-tune the exchange interactions in $Eu_{1-x}Y_xMnO_3$ by changing the Y concentration was instrumental in realizing this mixed state. When searching for new magnetoelectric materials for applications, such border cases seems to be a promising avenue to follow. Another way to fine-tune such a system could be to grow thin films of the material in question on different substrates, providing varying degrees of frustration to the crystal lattice. This method would also suit itself perfectly for constructing logical devices.

The assumption of Eu^{3+} being a non-magnetic substitute for other rare earths in $Eu_{1-x}Y_xMnO_3$ was put into question with the discovery of a Van Vleck type Eu magnetic moment induced by the symmetry-breaking presence of an exchange field set up by the Mn magnetic structure. The induced Eu moments were confirmed to order parallel to the Mn magnetic ordering. Since the induced Eu moments order with the same wave vector as the Mn moments, this could in principle influence the multiferroic properties of the compound through a symmetric exchange interaction between the Eu and Mn, as was observed in $GdMnO_3$. However, inverse Dzyaloshinskii-Moriya theory seems to already explain well the phenomenology of the $Eu_{1-x}Y_xMnO_3$ system, cf. section 2.3. A clarification of the possible impact of Eu magnetic order on the multiferroic properties of $Eu_{1-x}Y_xMnO_3$ would require careful studies using a combination of bulk measurements and scattering experiments investigating both the Mn and Eu magnetic structures.

Regardless of the outcome of such studies, the discovery of an induced Eu moment in $Eu_{1-x}Y_xMnO_3$ opens up the possibility of using Eu as a magnetic probe. This was done to great effect when measuring the C type magnetic structure, whose reflections are very weak at the Mn K edge resonance, and unavailable at the the Mn $L_{2,3}$ edges. Using the strong scattered signal at the Eu M_5 edge, the magnetic structure associated with the mixed-in WFM phase was confirmed to also have a C type component. The technique is easily transferable to other compounds readily doped with Eu^{3+}. Eu is already being used in multiferroics research as a non-magnetic substitute for other rare earth elements, and may as such already be put to use as a magnetic probe in this fashion.

Appendix A

Calculation of Stokes Parameters

The Jones matrix for resonant magnetic scattering at the first harmonic of the E1 transition from a magnetic structure with magnetic wave vector $\boldsymbol{\tau}$ is given by the second term of equation (3.24)

$$J = \begin{pmatrix} 0 & z_1 \cos\theta + z_3 \sin\theta \\ z_3 \sin\theta - z_1 \cos\theta & -z_2 \sin 2\theta \end{pmatrix} \tag{A.1}$$

where $z_{1,3}$ are the moment components in the scattering plane and z_2 is the moment component perpendicular to the scattering plane. In the σ, π basis, the incident polarization state of a beam with linear polarization angle η is described by the vector $(\cos\eta, \sin\eta)$. The polarization state of the scattered beam is found by operating on this vector with the Jones matrix:

$$\begin{bmatrix} f_{\sigma'} \\ f_{\pi'} \end{bmatrix} = \begin{pmatrix} 0 & z_1 \cos\theta + z_3 \sin\theta \\ z_3 \sin\theta - z_1 \cos\theta & -z_2 \sin 2\theta \end{pmatrix} \begin{bmatrix} \cos\eta \\ \sin\eta \end{bmatrix}. \tag{A.2}$$

During our measurements of the F type reflection (0 4-τ 0), the sample was mounted with bc in the scattering plane. That means we can identify the moment directions in the crystal basis as

$$\begin{aligned} z_1 &= z_c \\ z_2 &= z_a \\ z_3 &= z_b \end{aligned}$$

If the moment components are ordered collinearly along c, as expected for the F type magnetic order, the scattering amplitudes in the different

polarization channels as function of incident polarization angle η is then given by

$$\begin{aligned}\begin{bmatrix} f_{\sigma'} \\ f_{\pi'} \end{bmatrix} &= \begin{pmatrix} 0 & z_c \cos\theta \\ -z_c \cos\theta & 0 \end{pmatrix} \begin{bmatrix} \cos\eta \\ \sin\eta \end{bmatrix} \\ &= \begin{bmatrix} z_c \cos\theta \cos\eta \\ -z_c \cos\theta \sin\eta \end{bmatrix} \end{aligned} \tag{A.3}$$

The Stokes parameters for the scattered beam are then given by equations (3.7)-(3.9):

$$P_1'(\eta) = \frac{|f_{\sigma'}|^2 - |f_{\pi'}|^2}{|f_{\sigma'}|^2 + |f_{\pi'}|^2} = \frac{z_c^2 \cos^2\theta(\cos^2\eta - \sin^2\eta)}{z_c^2 \cos^2\theta(\cos^2\eta + \sin^2\eta)} = \cos 2\eta \tag{A.4}$$

and

$$\begin{aligned} P_2'(\eta) &= \frac{|f_{\sigma'} + f_{\pi'}|^2 - |f_{\sigma'} - f_{\pi'}|^2}{|f_{\sigma'} + f_{\pi'}|^2 + |f_{\sigma'} - f_{\pi'}|^2} \\ &= \frac{(\sin\eta + \cos\eta)^2 - (\sin\eta - \cos\eta)^2}{(\sin\eta + \cos\eta)^2 + (\sin\eta - \cos\eta)^2} = \sin 2\eta \end{aligned} \tag{A.5}$$

and

$$P_3'(\eta) = \frac{|f_{\sigma'} - if_{\pi'}|^2 - |f_{\sigma'} + if_{\pi'}|^2}{|f_{\sigma'} + f_{\pi'}|^2 + |f_{\sigma'} - f_{\pi'}|^2} \tag{A.6}$$

$$= \frac{z_c^2 \cos^2\theta(\cos\eta + \sin\eta)^2 - z_c^2 \cos^2\theta(\cos\eta + \sin\eta)^2}{|f_{\sigma'} + f_{\pi'}|^2 + |f_{\sigma'} - f_{\pi'}|^2} = 0. \tag{A.7}$$

While measuring the G type reflection (0 3-τ 1), the sample was mounted with ab in the scattering plane. We therefore have to redefine the moment directions as

$$\begin{aligned} z_1 &= z_b \\ z_2 &= z_c \\ z_3 &= z_a \end{aligned}$$

In addition, for this particular off-specular reflection the crystal had to be rotated with an angle χ to bring the c axis into the scattering plane. This mixes the moment components into each other. We find the new components $z'_{a,b,c}$ by application of the rotational matrix R_χ defining rotations by an angle

χ about the a direction of the crystal:

$$\begin{aligned}\begin{bmatrix} z'_a \\ z'_b \\ z'_c \end{bmatrix} &= R_\chi \begin{bmatrix} z_a \\ z_b \\ z_c \end{bmatrix} = \begin{pmatrix} 1 & 0 & 0 \\ 0 & \cos\chi & -\sin\chi \\ 0 & \sin\chi & \cos\chi \end{pmatrix} \begin{bmatrix} z_a \\ z_b \\ z_c \end{bmatrix} \\ &= \begin{bmatrix} z_a \\ z_b\cos\chi - z_c\sin\chi \\ z_b\sin\chi + z_c\cos\chi \end{bmatrix} \end{aligned} \tag{A.8}$$

The G type magnetic order is expected to form a circular cycloid in the ab plane, which means that $z_a = z_b = z$ and $z_c = 0$, or in laboratory coordinates:

$$\begin{aligned} z_1 &= z'_a = iz \\ z_2 &= z'_c = z\sin\chi \\ z_3 &= z'_b = z\cos\chi, \end{aligned}$$

where z'_a is set to be imaginary to preserve the phase information of the cycloid. This gives the polarization dependent scattering amplitudes

$$\begin{aligned}\begin{bmatrix} f_{\sigma'} \\ f_{\pi'} \end{bmatrix} &= \begin{pmatrix} 0 & iz\cos\theta + z\cos\chi\sin\theta \\ z\cos\chi\sin\theta - iz\cos\theta & -z\sin\chi\sin 2\theta \end{pmatrix} \begin{bmatrix} \cos\eta \\ \sin\eta \end{bmatrix} \\ &= \begin{bmatrix} z\sin\eta(i\cos\theta + \cos\chi\sin\theta) \\ z\cos\eta\cos\chi\sin\theta - z\sin\eta\sin\chi\sin 2\theta - iz\cos\eta\cos\theta \end{bmatrix}. \end{aligned} \tag{A.9}$$

Calculating the Stokes parameters for the scattered beam is again straightforward, if somewhat tedious:

$$
\begin{aligned}
P_1'(\eta) &= \frac{|f_{\sigma'}|^2 - |f_{\pi'}|^2}{|f_{\sigma'}|^2 + |f_{\pi'}|^2} \\
&= \frac{\begin{array}{r} z^2 \sin^2\eta(\cos^2\chi \sin^2\theta + \cos^2\theta) \\ - z^2\left((\cos\eta\cos\chi\sin\theta - \sin\eta\sin\chi\sin 2\theta)^2 + \cos^2\eta\cos^2\theta\right) \end{array}}{\begin{array}{r} z^2 \sin^2\eta(\cos^2\chi \sin^2\theta + \cos^2\theta) \\ + z^2\left((\cos\eta\cos\chi\sin\theta - \sin\eta\sin\chi\sin 2\theta)^2 + \cos^2\eta\cos^2\theta\right) \end{array}} \\
&= \frac{\begin{array}{r} -\cos^2\chi\sin^2\theta(\sin^2\eta - \cos^2\eta) + \cos^2\theta(\sin^2\eta - \cos^2\eta) \\ - \sin^2\eta\sin^2\chi\sin^2 2\theta + \sin\eta\cos\eta\sin\chi\cos\chi\sin\theta\sin 2\theta \end{array}}{\begin{array}{r} \cos^2\chi\sin^2\theta(\sin^2\eta + \cos^2\eta) + \cos^2\theta(\sin^2\eta + \cos^2\eta) \\ + \sin^2\eta\sin^2\chi\sin^2 2\theta - \sin\eta\cos\eta\sin\chi\cos\chi\sin\theta\sin 2\theta \end{array}} \\
&= \frac{\begin{array}{r} -(\cos^2\chi\sin^2\theta + \cos^2\theta)\cos 2\eta - \sin^2\eta\sin^2\chi\sin^2 2\theta \\ + \frac{1}{4}\sin 2\eta\sin 2\chi\sin\theta\sin 2\theta \end{array}}{\begin{array}{r} \cos^2\chi\sin^2\theta + \cos^2\theta + \sin^2\eta\sin^2\chi\sin^2 2\theta \\ - \frac{1}{4}\sin 2\eta\sin 2\chi\sin\theta\sin 2\theta \end{array}}
\end{aligned}
\tag{A.10}
$$

and

$$
\begin{aligned}
P_2'(\eta) &= \frac{|f_{\sigma'} + f_{\pi'}|^2 - |f_{\sigma'} - f_{\pi'}|^2}{|f_{\sigma'} + f_{\pi'}|^2 + |f_{\sigma'} - f_{\pi'}|^2} \\
&= \frac{\begin{array}{r} z^2(\sin\eta\cos\chi\sin\theta + \cos\eta\cos\chi\sin\theta - \sin\eta\sin\chi\sin 2\theta)^2 \\ + z^2\cos^2\theta(\sin\eta - \cos\eta)^2 \\ -z^2(\sin\eta\cos\chi\sin\theta - \cos\eta\cos\chi\sin\theta + \sin\eta\sin\chi\sin 2\theta)^2 \\ - z^2\cos^2\theta(\sin\eta + \cos\eta)^2 \end{array}}{\begin{array}{r} z^2(\sin\eta\cos\chi\sin\theta + \cos\eta\cos\chi\sin\theta - \sin\eta\sin\chi\sin 2\theta)^2 \\ + z^2\cos^2\theta(\sin\eta - \cos\eta)^2 \\ +z^2(\sin\eta\cos\chi\sin\theta - \cos\eta\cos\chi\sin\theta + \sin\eta\sin\chi\sin 2\theta)^2 \\ + z^2\cos^2\theta(\sin\eta + \cos\eta)^2 \end{array}} \\
&= \frac{\begin{array}{r} 4\sin\eta\cos\eta\cos^2\chi\sin^2\theta - 4\sin^2\eta\sin\chi\cos\chi\sin\theta\sin 2\theta \\ - 4\sin\eta\cos\eta\cos^2\theta \end{array}}{\begin{array}{r} 2\sin^2\eta\cos^2\chi\sin^2\theta + 2\sin^2\eta\sin^2\chi\sin^2 2\theta + 2\cos^2\eta\cos^2\chi\sin^2\theta \\ - 4\sin\eta\cos\eta\sin\chi\cos\chi\sin\theta\sin 2\theta + 2(\sin^2\eta + \cos^2\eta)\cos^2\theta \end{array}} \\
&= \frac{-(\cos^2\chi\sin^2\theta - \cos^2\theta)\sin 2\eta + \sin^2\eta\sin 2\chi\sin\theta\sin 2\theta}{\cos^2\chi\sin^2\theta + \sin^2\eta\sin^2\chi\sin^2 2\theta + \cos^2\theta - \frac{1}{2}\sin 2\eta\sin 2\chi\sin\theta\sin 2\theta}
\end{aligned}
\tag{A.11}
$$

and

$$P_3'(\eta) = \frac{|f_{\sigma'} - if_{\pi'}|^2 - |f_{\sigma'} + if_{\pi'}|^2}{|f_{\sigma'} + f_{\pi'}|^2 + |f_{\sigma'} - f_{\pi'}|^2}$$

$$\begin{aligned}
&= \frac{\begin{array}{r} z^2(\sin\eta\cos\chi\sin\theta - \cos\eta\cos\theta)^2 \\ + z^2(\sin\eta\cos\theta + \cos\eta\cos\chi\sin\theta - \sin\eta\sin\chi\sin 2\theta)^2 \\ -z^2(\sin\eta\cos\chi\sin\theta + \cos\eta\cos\theta)^2 \\ - z^2(\sin\cos\theta + \cos\eta\cos\chi\sin\theta - \sin\eta\sin\chi\sin 2\theta)^2 \end{array}}{\begin{array}{r} z^2(\sin\eta\cos\chi\sin\theta + \cos\eta\cos\chi\sin\theta - \sin\eta\sin\chi\sin 2\theta)^2 \\ + z^2\cos^2\theta(\sin\eta - \cos\eta)^2 \\ +z^2(\sin\eta\cos\chi\sin\theta - \cos\eta\cos\chi\sin\theta + \sin\eta\sin\chi\sin 2\theta)^2 \\ + z^2\cos^2\theta(\sin\eta + \cos\eta)^2 \end{array}} \\
&= \frac{\begin{array}{r} -4\sin\eta\cos\eta\cos\chi\sin\theta\cos\theta + 4\sin^2\eta\sin\chi\cos\theta\sin 2\theta \\ - 4\sin\eta\cos\eta\cos\chi\sin\theta\cos\theta \end{array}}{\begin{array}{r} 2\sin^2\eta\cos^2\chi\sin^2\theta + 2\sin^2\eta\sin^2\chi\sin^2 2\theta + 2\cos^2\eta\cos^2\chi\sin^2\theta \\ - 4\sin\eta\cos\eta\sin\chi\cos\chi\sin\theta\sin 2\theta + 2(\sin^2\eta + \cos^2\eta)\cos^2\theta \end{array}} \\
&= \frac{2\sin^2\eta\sin\chi\cos\theta\sin 2\theta - \sin 2\eta\cos\chi\sin 2\theta}{\cos^2\chi\sin^2\theta + \sin^2\eta\sin^2\chi\sin^2 2\theta + \cos^2\theta - \frac{1}{2}\sin 2\eta\sin 2\chi\sin\theta\sin 2\theta}.
\end{aligned} \tag{A.12}$$

Appendix B

Calculating REXS lineshape from XMCD data in an antiferromagnet

For resonant scattering from an antiferromagnet, the photon-energy-dependent scattered intensity is proportional to the absolute square of the magnetic form factor F, which in the simplest case of an antiferromagnet has contributions from both spin up ($F_\uparrow$) and spin down ($F_\downarrow$) moments:

$$I(E) \propto |F_\uparrow - F_\downarrow|^2 \tag{B.1}$$

The magnetic form factor is complex, $F = \mathrm{Re}(F) + i\mathrm{Im}(F)$, where the imaginary part describes the x-ray absorption. The real and imaginary components can be transformed into each other using the Kramers-Kronig transform (KKT), i.e. $\mathrm{Re}(F) = \mathrm{KKT}(\mathrm{Im}(F))$. The REXS intensity may therefore be written

$$\begin{aligned} I(E) &\propto |\mathrm{Re}(F_\uparrow) + i\mathrm{Im}(F_\uparrow) - (\mathrm{Re}(F_\downarrow) + i\mathrm{Im}(F_\downarrow))|^2 && \text{(B.2)} \\ &= |\mathrm{KKT}(\mathrm{Im}(F_\uparrow)) + i\mathrm{Im}(F_\uparrow) - \mathrm{KKT}(\mathrm{Im}(F_\downarrow)) - i\mathrm{Im}(F_\downarrow)|^2 && \text{(B.3)} \\ &= |\mathrm{KKT}(\mathrm{Im}(F_\uparrow) - \mathrm{Im}(F_\downarrow)) + i(\mathrm{Im}(F_\uparrow) - \mathrm{Im}(F_\downarrow))|^2 && \text{(B.4)} \\ &= |\mathrm{KKT}(\Delta) + i\Delta|^2 && \text{(B.5)} \end{aligned}$$

where we have defined $\Delta = \mathrm{Im}(F_\uparrow) - \mathrm{Im}(F_\downarrow)$.

X-ray circular magnetic dichroism (XMCD) probes the difference in absorption between spin directions parallel and antiparallel to the photon helicity. In other words, using circularly polarized light, the energy dependent XMCD signal (XMCD(E)) is proportional to the difference in absorption between spin up and spin down, i.e. $\Delta \propto \mathrm{XMCD}(E)$. We can therefore express

the REXS intensity in terms of a Kramers-Kronig transform of the XMCD signal:

$$I(E) \propto \mathrm{KKT}(\mathrm{XMCD}(E))^2 + \mathrm{XMCD}(E)^2 \tag{B.6}$$

Bibliography

[1] K. F. Wang, J.-M. Liu, and Z. F. Ren, "Multiferroicity: the coupling between magnetic and polarization orders," *Advances in Physics*, vol. 58, pp. 321–448, July-August 2009.

[2] D. Khomskii, "Classifying multiferroics: Mechanisms and effects," *Physics*, vol. 2, p. 20, Mar 2009.

[3] H. Adachi and H. Ino, "A ferromagnet having no net magnetic moment," *Nature*, vol. 401, p. 148, Sep 1999.

[4] C. Ruegg, N. Cavadini, A. Furrer, H.-U. Gudel, K. Kramer, H. Mutka, A. Wildes, K. Habicht, and P. Vorderwisch, "Bose-einstein condensation of the triplet states in the magnetic insulator $TlCuCl_3$," *Nature*, vol. 423, pp. 62–65, May 2003.

[5] V. S. Zapf, D. Zocco, B. R. Hansen, M. Jaime, N. Harrison, C. D. Batista, M. Kenzelmann, C. Niedermayer, A. Lacerda, and A. Paduan-Filho, "Bose-einstein condensation of $S = 1$ nickel spin degrees of freedom in $NiCl_2$-$4SC(NH_2)_2$," *Phys. Rev. Lett.*, vol. 96, p. 077204, Feb 2006.

[6] E. Schierle, V. Soltwisch, D. Schmitz, R. Feyerherm, A. Maljuk, F. Yokaichiya, D. N. Argyriou, and E. Weschke, "Cycloidal order of $4f$ moments as a probe of chiral domains in $DyMnO_3$," *Phys. Rev. Lett.*, vol. 105, p. 167207, Oct 2010.

[7] M. E. Lines and A. Glass, *Principle and Application of Ferroelectric and Related Materials*. Oxford University Press, 2001.

[8] N. A. Spaldin and M. Fiebig, "The renaissance of magnetoelectric multiferroics," *Science*, vol. 309, no. 5733, pp. 391–392, 2005.

[9] M. Fiebig, "Revival of the magnetoelectric effect," *J. Phys. D*, vol. 38, no. 8, p. R123, 2005.

[10] C.-W. Nan, M. I. Bichurin, S. Dong, D. Viehland, and G. Srinivasan, "Multiferroic magnetoelectric composites: Historical perspective, status, and future directions," *Journal of Applied Physics*, vol. 103, no. 3, pp. –, 2008.

[11] A. G. Gavriliuk, S. A. Kharlamova, I. S. Lyubutin, I. A. Troyan, S. G. Ovchinnikov, A. M. Potseluiko, M. I. Eremets, and R. Boehler, "Structural and electronic transitions in gadolinium iron borate $GdFe_3(BO_3)_4$ at high pressures," *JETP Letters*, vol. 80, pp. 426 – 432, 2004.

[12] H. Mo, C. S. Nelson, L. N. Bezmaternykh, and V. T. Temerov, "Magnetic structure of the field-induced multiferroic $GdFe_3(BO_3)_4$," *Phys. Rev. B*, vol. 78, p. 214407, Dec 2008.

[13] L. Yan, J. Li, and D. Viehland, "Deposition conditions and electrical properties of relaxor ferroelectric $Pb(Fe_{1/2}Nb_{1/2})O_3$ thin films prepared by pulsed laser deposition," *Journal of Applied Physics*, vol. 101, no. 10, 2007.

[14] Y. Yang, J.-M. Liu, H. B. Huang, W. Q. Zou, P. Bao, and Z. G. Liu, "Magnetoelectric coupling in ferroelectromagnet $Pb(Fe_{1/2}Nb_{1/2})O_3$ single crystals," *Phys. Rev. B*, vol. 70, p. 132101, Oct 2004.

[15] T. Lottermoser, T. Lonkai, U. Amann, D. Hohlwein, J. Ihringer, and M. Fiebig, "Magnetic phase control by an electric field," *Nature*, vol. 430, p. 541, July 2004.

[16] T. Kimura, T. Goto, H. Shintani, K. Ishizaka, T. Arima, and Y. Tokura, "Magnetic control of ferroelectric polarization," *Nature*, vol. 426, p. 55, 2003.

[17] N. Hur, S. Park, P. A. Sharma, J. S. Ahn, S. Guha, and S.-W. Cheong, "Electric polarization reversal and memory in a multiferroic material induced by magnetic fields," *Nature*, vol. 429, pp. 392–395, May 2004.

[18] M. Mostovoy, "Ferroelectricity in spiral magnets," *Phys. Rev. Lett.*, vol. 96, p. 067601, 2006.

[19] I. E. Dzyaloshinskii, "On the magneto-electrical effect in antiferromagnets," *Sov.Phys. JETP*, vol. 96, p. 628, 1960.

[20] J. J. Betouras, G. Giovannetti, and J. van den Brink, "Multiferroicity induced by dislocated spin-density waves," *Phys. Rev. Lett.*, vol. 98, p. 257602, Jun 2007.

[21] R. Bursill, G. A. Gehring, D. J. J. Farnell, J. B. Parkinson, T. Xiang, and C. Zeng, "Numerical and approximate analytical results for the frustrated spin- 1/2 quantum spin chain," *Journal of Physics: Condensed Matter*, vol. 7, no. 45, p. 8605, 1995.

[22] I. A. Sergienko and E. Dagotto, "Role of the dzyaloshinskii-moriya interaction in multiferroic perovskites," *Phys. Rev. B*, vol. 73, p. 094434, Mar 2006.

[23] H. Katsura, N. Nagaosa, and A. V. Balatsky, "Spin current and magnetoelectric effect in noncollinear magnets," *Phys. Rev. Lett.*, vol. 95, p. 057205, 2005.

[24] J. Hu, "Microscopic origin of magnetoelectric coupling in noncollinear multiferroics," *Phys. Rev. Lett.*, vol. 100, p. 077202, Feb 2008.

[25] T. Moriya, "Anisotropic superexchange interaction and weak ferromagnetism," *Phys. Rev.*, vol. 120, pp. 91–98, Oct 1960.

[26] S.-W. Cheong and M. Mostovoy, "Multiferroics: a magnetic twist for ferroelectricity," *Nat. Mater.*, vol. 6, pp. 13–20, Jan 2007.

[27] M. Mochizuki and N. Furukawa, "Microscopic model and phase diagrams of the multiferroic perovskite manganites," *Phys. Rev. B*, vol. 80, p. 134416, Oct 2009.

[28] T. Kimura, S. Ishihara, H. Shintani, T. Arima, K. T. Takahashi, K. Ishizaka, and Y. Tokura, "Distorted perovskite with e_g^1 configuration as a frustrated spin system," *Phys. Rev. B*, vol. 68, p. 060403, Aug 2003.

[29] J.-S. Zhou and J. B. Goodenough, "Unusual evolution of the magnetic interactions versus structural distortions in $R\mathrm{MnO}_3$ perovskites," *Phys. Rev. Lett.*, vol. 96, p. 247202, Jun 2006.

[30] S. Quezel, F. Tcheou, J. Rossat-Mignod, G. Quezel, and E. Roudaut, "Magnetic structure of the perovskite-like compound TbMnO_3," *Physica B+C*, vol. 86-88, Part 2, no. 0, pp. 916 – 918, 1977.

[31] R. Kajimoto, H. Yoshizawa, H. Shintani, T. Kimura, and Y. Tokura, "Magnetic structure of TbMnO_3 by neutron diffraction," *Phys. Rev. B*, vol. 70, p. 012401, Jul 2004.

[32] M. Kenzelmann, A. B. Harris, S. Jonas, C. Broholm, J. Schefer, S. B. Kim, C. L. Zhang, S.-W. Cheong, O. P. Vajk, and J. W. Lynn, "Magnetic inversion symmetry breaking and ferroelectricity in $TbMnO_3$," *Phys. Rev. Lett.*, vol. 95, p. 087206, Aug 2005.

[33] R. Feyerherm, E. Dudzik, N. Aliouane, and D. N. Argyriou, "Commensurate dy magnetic ordering associated with incommensurate lattice distortion in multiferroic $DyMnO_3$," *Phys. Rev. B*, vol. 73, p. 180401, May 2006.

[34] T. Goto, Y. Yamasaki, H. Watanabe, T. Kimura, and Y. Tokura, "Anticorrelation between ferromagnetism and ferroelectricity in perovskite manganites," *Phys. Rev. B*, vol. 72, p. 220403, Dec 2005.

[35] J. Hemberger, F. Schrettle, A. Pimenov, P. Lunkenheimer, V. Y. Ivanov, A. A. Mukhin, A. M. Balbashov, and A. Loidl, "Multiferroic phases of $Eu_{1-x}Y_xMnO_3$," *Phys. Rev. B*, vol. 75, p. 035118, Jan 2007.

[36] Y. Yamasaki, S. Miyasaka, T. Goto, H. Sagayama, T. Arima, and Y. Tokura, "Ferroelectric phase transitions of $3d$-spin origin in $Eu_{1-x}Y_xMnO_3$," *Phys. Rev. B*, vol. 76, p. 184418, Nov 2007.

[37] V. Y. Ivanov, A. A. Mukhin, V. D. Travkin, A. S. Prokhorov, Y. F. Popov, A. M. Kadomtseva, G. P. Vorob, K. I. Kamilov, and A. M. Balbashov, "New orthorhombic multiferroics $R_{1-x}Y_xMnO_3$ (R = Eu, Gd)," *Phys. Stat. Sol.*, vol. 243, pp. 107–111, Jan 2006.

[38] A. Yoshimori, "A new type of antiferromagnetic structure in the rutile type crystal," *Journal of the Physical Society of Japan*, vol. 14, no. 6, pp. 807–821, 1959.

[39] T. A. Kaplan, "Classical spin-configuration stability in the presence of competing exchange forces," *Phys. Rev.*, vol. 116, pp. 888–889, Nov 1959.

[40] J. Villain, "La structure des substances magnetiques," *Journal of Physics and Chemistry of Solids*, vol. 11, no. 3-4, pp. 303 – 309, 1959.

[41] I. Dzyaloshinsky, "A thermodynamic theory of "weak" ferromagnetism of antiferromagnetics," *Journal of Physics and Chemistry of Solids*, vol. 4, no. 4, pp. 241 – 255, 1958.

[42] Skumryev, V., Ott, F., Coey, J. M.D., Anane, A., Renard, J.-P., Pinsard-Gaudart, L., and Revcolevschi, A., "Weak ferromagnetism in lamno3," *Eur. Phys. J. B*, vol. 11, no. 3, pp. 401–406, 1999.

[43] S.-W. Cheong, J. Thompson, and Z. Fisk, "Metamagnetism in la_2cuo_4," *Phys. Rev. B*, vol. 39, pp. 4395–4398, Mar 1989.

[44] H. Jang, J.-S. Lee, K.-T. Ko, W.-S. Noh, T. Y. Koo, J.-Y. Kim, K.-B. Lee, J.-H. Park, C. L. Zhang, S. B. Kim, and S.-W. Cheong, "Coupled magnetic cycloids in multiferroic $TbMnO_3$ and $Eu_{3/4}Y_{1/4}MnO_3$," *Phys. Rev. Lett.*, vol. 106, p. 047203, Jan 2011.

[45] H. Jang. Personal Communication, 2014.

[46] H. Jang. Personal Communication, 2012.

[47] H. W. Brinks, J. Rodríguez-Carvajal, H. Fjellvåg, A. Kjekshus, and B. C. Hauback, "Crystal and magnetic structure of orthorhombic $HoMnO_3$," *Phys. Rev. B*, vol. 63, p. 094411, Feb 2001.

[48] J. Strempfer, B. Bohnenbuck, M. Mostovoy, N. Aliouane, D. N. Argyriou, F. Schrettle, J. Hemberger, A. Krimmel, and M. v. Zimmermann, "Absence of commensurate ordering at the polarization flop transition in multiferroic $DyMnO_3$," *Phys. Rev. B*, vol. 75, p. 212402, Jun 2007.

[49] S. Danjoh, J.-S. Jung, H. Nakamura, Y. Wakabayashi, and T. Kimura, "Anomalous induction of ferroelectric polarization by magnetization reversal in the phase-separated multiferroic manganite $Eu_{0.8}Y_{0.2}MnO_3$," *Phys. Rev. B*, vol. 80, p. 180408, Nov 2009.

[50] Y. J. Choi, C. L. Zhang, N. Lee, and S.-W. Cheong, "Cross-control of magnetization and polarization by electric and magnetic fields with competing multiferroic and weak-ferromagnetic phases," *Phys. Rev. Lett.*, vol. 105, p. 097201, Aug 2010.

[51] O. Prokhnenko, R. Feyerherm, E. Dudzik, S. Landsgesell, N. Aliouane, L. C. Chapon, and D. N. Argyriou, "Enhanced ferroelectric polarization by induced Dy spin order in multiferroic $DyMnO_3$," *Phys. Rev. Lett.*, vol. 98, p. 057206, Feb 2007.

[52] R. Feyerherm, E. Dudzik, A. U. B. Wolter, S. Valencia, O. Prokhnenko, A. Maljuk, S. Landsgesell, N. Aliouane, L. Bouchenoire, S. Brown, and D. N. Argyriou, "Magnetic-field induced effects on the electric polarization in $RMnO_3$ (R=Dy,Gd)," *Phys. Rev. B*, vol. 79, p. 134426, Apr 2009.

[53] R. Feyerherm, E. Dudzik, O. Prokhnenko, and D. N. Argyriou, "Rare earth magnetism and ferroelectricity in $RMnO_3$," *Journal of Physics: Conference Series*, vol. 200, p. 012032, 2010.

[54] W. C. Röntgen, "Über eine neue art von strahlen," *Sitzungsberichte der Physik.-mediz. Gesellschaft zu Würzburg*, vol. 132, 1895.

[55] W. Friedrich, P. Knipping, and M. Laue, "Interferenzerscheinungen bei Röntgenstrahlen," *Sitzungsberichte der Bayerische Akademie der Wissenshaften*, vol. 302, 1912.

[56] W. Friedrich, P. Knipping, and M. Laue, "Interferenzerscheinungen bei Röntgenstrahlen," *Annalen der Physik*, vol. 346, pp. 971–988, 1913.

[57] T. Udem. `bmo.physik.uni-muenchen.de/lehre/WS12/E3/vorlesung.html`.

[58] `http://www.psi.ch/swissfel/why-swissfel`.

[59] `http://www.hep.ucl.ac.uk/xfel/`.

[60] K. Wille, *Physik der Teilchenbeschleuniger und Synchrotronstrahlungsquellen*. Teubner Studienbücher, 1992.

[61] C. Detlefs, M. Sanchez del Rio, and C. Mazzoli, "X-ray polarization: General formalism and polarization analysis," *The European Physical Journal Special Topics*, vol. 208, no. 1, pp. 359–371, 2012.

[62] D. H. Goldstein, *Polarized Light*. CRC Press, 3rd edn. ed., 2011.

[63] M. Blume and D. Gibbs, "Polarization dependence of magnetic x-ray scattering," *Phys. Rev. B*, vol. 37, pp. 1779–1789, Feb 1988.

[64] J. P. Hill and D. F. McMorrow, "X-ray resonant exchange scattering: Polarization dependence and correlation functions," *Acta Crystallogr. A*, vol. 52, p. 236, 1996.

[65] S. D. Matteo, "Dipole-quadrupole spherical tensors in resonant x-ray diffraction," *Journal of Physics: Conference Series*, vol. 211, no. 1, p. 012008, 2010.

[66] S. Nandi, *Lecture Notes of the 43rd IFF Spring School "Scattering Methods for Condensed Matter Research: Towards Novel Applications at Future Sources*, ch. C7. Forschungszentrum Jülich, 2012.

[67] M. Blume, "Magnetic scattering of x rays (invited)," *Journal of Applied Physics*, vol. 57, no. 8, pp. 3615–3618, 1985.

[68] J. P. Hannon, G. T. Trammell, M. Blume, and D. Gibbs, "X-ray resonance exchange scattering," *Phys. Rev. Lett.*, vol. 61, pp. 1245–1248, Sep 1988.

[69] J. W. Kim, Y. Lee, D. Wermeille, B. Sieve, L. Tan, S. L. Bud'ko, S. Law, P. C. Canfield, B. N. Harmon, and A. I. Goldman, "Systematics of x-ray resonant scattering amplitudes in $r\mathrm{ni}_2\mathrm{ge}_2$ (r = Gd,tb,dy,ho,er,tm): The origin of the branching ratio at the l edges of the heavy rare earths," *Phys. Rev. B*, vol. 72, p. 064403, Aug 2005.

[70] V. B. Berestetskii, E. M. Lifshitz, and L. P. Pitaevskii, *Relativistic Quantum Theory*. New York: Pergamon Press, 1971.

[71] M. Hamrick, "Theory of elastic x-ray resonant exchange scattering in lanthanides and actinides," Master's thesis, Rice University, 1990.

[72] M. Hamrick, *Magnetic and chemical effects in x-ray resonant exchange scattering in rare earths and transition metal compounds*. PhD thesis, Rice University, USA, 1994.

[73] J. Strempfer, U. Rütt, and W. Jauch, "Absolute spin magnetic moment of fef_2 from high energy photon diffraction," *Phys. Rev. Lett.*, vol. 86, pp. 3152–3155, Apr 2001.

[74] I. Solovyev and K. Terakura, "Spin canting in three-dimensional perovskite manganites," *Phys. Rev. B*, vol. 63, p. 174425, Apr 2001.

[75] J. Strempfer, T. Brückel, U. Rütt, J. R. Schneider, K.-D. Liss, and T. Tschentscher, "The non-resonant magnetic x-ray scattering cross section of mnf_2. 2. high-energy x-ray diffraction at 80kev," *Acta Crystallographica Section A*, vol. 52, no. 3, pp. 438–449, 1996.

[76] J. Strempfer, T. Brückel, D. Hupfeld, J. R. Schneider, K.-D. Liss, and T. Tschentscher, "The non-resonant magnetic x-ray scattering cross-section for photon energies up to 500 kev," *EPL (Europhysics Letters)*, vol. 40, no. 5, p. 569, 1997.

[77] S. W. Lovesey and S. P. Collins, *X-Ray Scattering and Absorption by Magnetic Materials*. Oxford University Press, 1996.

[78] E. Arnold, M. I. Aroyo, A. Authier, C. P. Brock, G. Chapuis, C. J. Gilmore, T. Hahn, S. R. Hall, D. M. Himmel, J. A. Kaduk, V. Kopský, D. B. Litvin, B. McMahon, U. Müller, E. Prince, M. G. Rossmann, H. Schenk, U. Shmueli, T. R. Welberry, and H. Wondratschek, eds., *International Tables for Crystallography*. International Union of Crystallography, 2006.

[79] J. Strempfer, S. Francoual, D. Reuther, D. K. Shukla, A. Skaugen, H. Schulte-Schrepping, T. Kracht, and H. Franz, "Resonant scattering and diffraction beamline P09 at PETRA III," *Journal of Synchrotron Radiation*, vol. 20, pp. 541–549, Jul 2013.

[80] R. Brandelik, W. Braunschweig, K. Gather, V. Kadansky, K. Lübelsmeyer, P. Mättig, H.-U. Martyn, G. Peise, J. Rimkus, H. Sander, D. Schmitz, A. S. von Dratzig, D. Trines, W. Wallraff, H. Boerner, H. Fischer, H. Hartmann, E. Hilger, W. Hillen, G. Knop, W. Korbach, P. Leu, B. Löhr, F. Roth, W. Rühmer, R. Wedemeyer, N. Wermes, M. Wollstadt, R. Bühring, R. Fohrmann, D. Heyland, H. Hultschig, P. Joos, W. Koch, U. Kötz, H. Kowalski, A. Ladage, D. Lüke, H. Lynch, G. Mikenberg, D. Notz, J. Pyrlik, R. Riethmüller, M. Schliwa, P. Söding, B. Wiik, G. Wolf, M. Holder, G. Poelz, J. Ringel, O. Römer, R. Rüsch, P. Schmüser, D. Binnie, P. Dornan, N. Downie, D. Garbutt, W. Jones, S. Lloyd, D. Pandoulas, A. Pevsner, J. Sedgebeer, S. Yarker, C. Youngman, R. Barlow, R. Cashmore, J. Illingworth, M. Ogg, G. Salmon, K. Bell, W. Chinowsky, B. Foster, J. Hart, J. Proudfoot, D. Quarrie, D. Saxon, P. Woodworth, Y. Eisenberg, U. Karshon, E. Kogan, D. Revel, E. Ronat, A. Shapira, J. Freeman, P. Lecomte, T. Meyer, L. W. Sau, and G. Zobernig, "Evidence for planar events in e^+e^- annihilation at high energies," *Physics Letters B*, vol. 86, no. 2, pp. 243 – 249, 1979.

[81] W. Bartel, T. Canzler, D. Cords, P. Dittmann, R. Eichler, R. Felst, D. Haidt, S. Kawabata, H. Krehbiel, B. Naroska, L. O'Neill, J. Olsson, P. Steffen, W. Yen, E. Elsen, M. Helm, A. Petersen, P. Warming, G. Weber, H. Drumm, J. Heintze, G. Heinzelmann, R. Heuer, J. von Krogh, P. Lennert, H. Matsumura, T. Nozaki, H. Rieseberg, A. Wagner, D. Darvill, F. Foster, G. Hughes, H. Wriedt, J. Allison, J. Armitage, I. Duerdoth, J. Hassard, F. Loebinger, B. King, A. Macbeth, H. Mills, P. Murphy, H. Prosper, K. Stephens, D. Clarke, M. Goddard, R. Hedgecock, R. Marshall, G. Pearce, M. Imori, T. Kobayashi, S. Komamiya, M. Koshiba, M. Minowa, S. Orito, A. Sato, T. Suda, H. Takeda, Y. Totsuka, Y. Watanabe, S. Yamada, and C. Yanagisawa,

"Observation of planar three-jet events in e^+e^- annihilation and evidence for gluon bremsstrahlung," *Physics Letters B*, vol. 91, no. 1, pp. 142 – 147, 1980.

[82] O. H. Seeck, C. Deiter, K. Pflaum, F. Bertam, A. Beerlink, H. Franz, J. Horbach, H. Schulte-Schrepping, B. M. Murphy, M. Greve, and O. Magnussen, "The high-resolution diffraction beamline P08 at PETRA III," *Journal of Synchrotron Radiation*, vol. 19, pp. 30–38, Jan 2012.

[83] C. Giles, C. Malgrange, J. Goulon, F. de Bergevin, C. Vettier, A. Fontaine, E. Dartyge, and S. Pizzini, "Energy and polarization-tunable x-ray quarter-wave plates for energy dispersive absorption spectrometer," *Nuclear Instruments and Methods in Physics Research Section A: Accelerators, Spectrometers, Detectors and Associated Equipment*, vol. 349, no. 2 - 3, pp. 622 – 625, 1994.

[84] S. Francoual, J. Strempfer, D. Reuther, D. K. Shukla, and A. Skaugen, "Double phase-retarder set-up at beamline p09 at petra iii," *Journal of Physics: Conference Series*, vol. 425, no. 13, p. 132010, 2013.

[85] V. Scagnoli, C. Mazzoli, C. Detlefs, P. Bernard, A. Fondacaro, L. Paolasini, F. Fabrizi, and F. de Bergevin, "Linear polarization scans for resonant X-ray diffraction with a double-phase-plate configuration," *Journal of Synchrotron Radiation*, vol. 16, pp. 778–787, Nov 2009.

[86] W. R. Busing and H. A. Levy, "Angle calculations for 3- and 4-circle X-ray and neutron diffractometers," *Acta Crystallographica*, vol. 22, pp. 457–464, Apr 1967.

[87] `http://groups.physics.umn.edu/zudovlab/manuals/cryogenics/`.

[88] U. Englisch, H. Rossner, H. Maletta, J. Bahrdt, S. Sasaki, F. Senf, K. Sawhney, and W. Gudat, "The elliptical undulator {UE46} and its monochromator beam-line for structural research on nanomagnets at bessy-ii," *Nuclear Instruments and Methods in Physics Research Section A*, vol. 467-468, no. 0, pp. 541 – 544, 2001.

[89] J. Fink, E. Schierle, E. Weschke, and J. Geck, "Resonant elastic soft x-ray scattering," *Reports on Progress in Physics*, vol. 76, no. 5, p. 056502, 2013.

[90] http://www.helmholtz-berlin.de/pubbin/igama_output?modus=einzel&sprache=en&gid=1641&typoid=50740.

[91] F. Fabrizi, H. Walker, L. Paolasini, F. de Bergevin, A. Boothroyd, D. Prabhakaran, and D. McMorrow, "Circularly polarized x rays as a probe of noncollinear magnetic order in multiferroic $tbmno_3$," *Phys. Rev. Lett.*, vol. 102, p. 237205, Jun 2009.

[92] J. Strempfer, B. Bohnenbuck, I. Zegkinoglou, N. Aliouane, S. Landsgesell, M. Zimmermann, and D. Argyriou, "Magnetic-field-induced transitions in multiferroic $tbmno_3$ probed by resonant and nonresonant x-ray diffraction," *Phys. Rev. B*, vol. 78, p. 024429, Jul 2008.

[93] N. Aliouane, O. Prokhnenko, R. Feyerherm, M. Mostovoy, J. Strempfer, K. Habicht, K. C. Rule, E. Dudzik, A. U. B. Wolter, A. Maljuk, and D. N. Argyriou, "Magnetic order and ferroelectricity in $RMnO_3$ multiferroic manganites: coupling between R- and Mn-spins," *J. Phys. Cond. Mat.*, vol. 20, p. 434215, Oct 2008.

[94] E. Bertaut, "On group theoretical techniques in magnetic structure analysis," *Journal of Magnetism and Magnetic Materials*, vol. 24, no. 3, pp. 267 – 278, 1981.

[95] N. Schell, A. King, F. Beckmann, H.-U. Ruhnau, R. Kirchhof, R. Kiehn, M. Müller, and A. Schreyera, "The high energy materials science beamline (hems) at petra iii," in *Materials Science Forum*, vol. 772, pp. 57–61, 2014.

[96] T. Goto, T. Kimura, G. Lawes, A. P. Ramirez, and Y. Tokura, "Ferroelectricity and giant magnetocapacitance in perovskite rare-earth manganites," *Phys. Rev. Lett.*, vol. 92, p. 257201, 2004.

[97] T. Kimura, G. Lawes, T. Goto, Y. Tokura, and A. P. Ramirez, "Magnetoelectric phase diagrams of orthorhombic $R\mathrm{MnO_3}$ (R=Gd, Tb, and Dy)," *Phys. Rev. B*, vol. 71, p. 224425, 2005.

[98] T. Arima, T. Goto, Y. Yamasaki, S. Miyasaka, K. Ishii, M. Tsubota, T. Inami, Y. Murakami, and Y. Tokura, "Magnetic-field-induced transition in the lattice modulation of colossal magnetoelectric $GdMnO_3$ and $TbMnO_3$ compounds," *Phys. Rev. B*, vol. 72, p. 100102, Sep 2005.

[99] T. Arima, Y. Yamasaki, T. Goto, S. Iguchi, K. Ohgushi, S. Miyasaka, and Y. Tokura, "Spin-lattice coupling in ferroelectric spiral magnets:

Comparison between the cases of (Tb,Dy)MnO_3 and $CoCr_2O_4$," *J. Phys. Soc. Jpn.*, vol. 76, p. 023602, February 2007.

[100] T. Arima, "Ferroelectricity induced by proper-screw type magnetic order," *J. Phys. Soc. Jpn.*, vol. 76, p. 073702, July 2007.

[101] A. Skaugen, D. K. Shukla, R. Feyerherm, E. Dudzik, Z. Islam, and J. Strempfer, "Magnetic order in $GdMnO_3$ in magnetic fields," *Journal of Physics: Conference Series*, vol. 519, no. 1, p. 012007, 2014.

[102] J. A. Moreira, A. Almeida, W. S. Ferreira, M. R. Chaves, S. M. F. Vilela, and P. B. Tavares, "Re-analysing the phase sequence in $Eu_{0.8}Y_{0.2}MnO_3$." Unpublished.

[103] C. Mazzoli, S. B. Wilkins, S. Di Matteo, B. Detlefs, C. Detlefs, V. Scagnoli, L. Paolasini, and P. Ghigna, "Disentangling multipole resonances through a full x-ray polarization analysis," *Phys. Rev. B*, vol. 76, p. 195118, Nov 2007.

[104] T. R. Forrest, S. R. Bland, S. B. Wilkins, H. C. Walker, T. A. W. Beale, P. D. Hatton, D. Prabhakaran, A. T. Boothroyd, D. Mannix, F. Yakhou, and D. F. McMorrow, "Ordering of localized electronic states in multiferroic $tbmno_3$: a soft x-ray resonant scattering study," *Journal of Physics: Condensed Matter*, vol. 20, no. 42, p. 422205, 2008.

[105] A. Frank, "Temperature variation of the magnetic susceptibility, gyromagnetic ratio, and heat capacity in Sm^{+++} and Eu^{+++}," *Phys. Rev.*, vol. 39, pp. 119–129, Jan 1932.

[106] J. H. Van Vleck, "Magnetic case history of the Eu^3+ ion," *Journal of Applied Physics*, vol. 39, no. 2, pp. 365–372, 1968.

[107] Y. Takikawa, S. Ebisu, and S. Nagata, "Van vleck paramagnetism of the trivalent eu ions," *Journal of Physics and Chemistry of Solids*, vol. 71, no. 11, pp. 1592 – 1598, 2010.

[108] B. J. Ruck, H. J. Trodahl, J. H. Richter, J. C. Cezar, F. Wilhelm, A. Rogalev, V. N. Antonov, B. D. Le, and C. Meyer, "Magnetic state of eun: X-ray magnetic circular dichroism at the Eu $M_{4,5}$ and $L_{2,3}$ absorption edges," *Phys. Rev. B*, vol. 83, p. 174404, May 2011.

[109] M. D. Johannes and W. E. Pickett, "Magnetic coupling between nonmagnetic ions: Eu^{3+} in EuN and EuP," *Phys. Rev. B*, vol. 72, p. 195116, Nov 2005.

[110] E. Schierle. Personal Communication, 2014.

[111] D. Mannix, A. Stunault, N. Bernhoeft, L. Paolasini, G. H. Lander, C. Vettier, F. de Bergevin, D. Kaczorowski, and A. Czopnik, "Resonant enhancements at nonmagnetic ions: New possibilities for magnetic x-ray scattering," *Phys. Rev. Lett.*, vol. 86, pp. 4128–4131, Apr 2001.

[112] T. A. W. Beale, S. B. Wilkins, R. D. Johnson, S. R. Bland, Y. Joly, T. R. Forrest, D. F. McMorrow, F. Yakhou, D. Prabhakaran, A. T. Boothroyd, and P. D. Hatton, "Antiferromagnetically spin polarized oxygen observed in magnetoelectric $\mathrm{tbmn_2o_5}$," *Phys. Rev. Lett.*, vol. 105, p. 087203, Aug 2010.

[113] S. Partzsch, S. B. Wilkins, J. P. Hill, E. Schierle, E. Weschke, D. Souptel, B. Büchner, and J. Geck, "Observation of electronic ferroelectric polarization in multiferroic $\mathrm{ymn_2o_5}$," *Phys. Rev. Lett.*, vol. 107, p. 057201, Jul 2011.

[114] M. W. Haverkort, C. Schüßler-Langeheine, C. F. Chang, M. Buchholz, H.-H. Wu, H. Ott, E. Schierle, D. Schmitz, A. Tanaka, and L. H. Tjeng, "Atomic multiplet calculation of $3d_{5/2} \rightarrow 4f$ resonant x-ray diffraction from Ho metal." Unpublished, May 2008.

[115] G. van der Laan. Personal Communication, 2014.

[116] B. T. Thole, G. van der Laan, J. C. Fuggle, G. A. Sawatzky, R. C. Karnatak, and J.-M. Esteva, "$3d$ x-ray-absorption lines and the $3d^9 4f^{n+1}$ multiplets of the lanthanides," *Phys. Rev. B*, vol. 32, pp. 5107–5118, Oct 1985.

[117] R. D. Cowan, *The Theory of Atomic Structure and Spectra*. University of California Press, 1981.

[118] J. B. Gruber, U. Vetter, T. Taniguchi, G. W. Burdick, H. Hofsäss, S. Chandra, and D. K. Sardar, "Spectroscopic analysis of Eu^3+ in single-crystal hexagonal phase aln," *Journal of Applied Physics*, vol. 110, no. 2, p. 023104, 2011.

[119] G. van der Laan, "Hitchhiker's guide to multiplet calculations," in *Magnetism: A Synchrotron Radiation Approach* (E. Beaurepaire, H. Bulou, F. Scheurer, and J.-P. Kappler, eds.), vol. 697 of *Lecture Notes in Physics*, pp. 143–199, Springer Berlin Heidelberg, 2006.

[120] M. Tovar, D. Rao, J. Barnett, S. B. Oseroff, J. D. Thompson, S.-W. Cheong, Z. Fisk, D. C. Vier, and S. Schultz, "eu_2CuO_4 : *Ananisotropicvanvleckparamagnet*," *Phys. Rev. B*, vol. 39, pp. 2661–2663, Feb 1989.

[121] J. Voigt, J. Persson, J. W. Kim, G. Bihlmayer, and T. Brückel, "Strong coupling between the spin polarization of mn and tb in multiferroic $TbMnO_3$ determined by x-ray resonance exchange scattering," *Phys. Rev. B*, vol. 76, p. 104431, Sep 2007.

[122] G. Khaliullin, "Excitonic magnetism in van vleck-type d^4 mott insulators," *Phys. Rev. Lett.*, vol. 111, p. 197201, Nov 2013.

List of publications

- *Magnetic order in $GdMnO_3$ in magnetic fields*
  A. Skaugen, D. K. Shukla, R. Feyerherm, E. Dudzik, Z. Islam, and J. Strempfer. *Journal of Physics: Conference Series*, **519** (1), 012007 (2014)

- *Long range antiferromagnetic order of Van Vleck type ions observed in multiferroic $Eu_{1-x}Y_xMnO_3$*
  A. Skaugen, E. Shierle, G. van der Laan, D. K. Shukla, H. C. Walker, E. Weschke, and J. Strempfer. *Submitted 2014*

- *Resonant scattering and diffraction beamline P09 at PETRA III*
  J. Strempfer, S. Francoual, D. Reuther, D. K. Shukla, **A. Skaugen**, H. Schulte-Schrepping, T. Kracht, and H. Franz. *Journal of Synchrotron Radiation*, **20**, 541 (2013)

- *Double phase-retarder set-up at beamline P09 at PETRA III*
  S. Francoual, J. Strempfer, D. Reuther, D. K. Shukla, and **A. Skaugen**. *Journal of Physics: Conference Series*, **425**, 132010 (2013)

- *Single-Crystal X-ray diffraction and resonant X-ray magnetic scattering at Helium-3 temperatures in high magnetic fields at beamline P09 at PETRA III*
  S. Francoual, J. Strempfer, J. Warren, Y. Liu, **A. Skaugen**, S. Poli, J. Blume, F. Wolff-Fabris, P. C. Canfield, and A. Lograsso. *Submitted 2015*

Acknowledgment

First and foremost I want to thank my supervisor Dr. Jörg Strempfer for coming up with an interesting research project and for giving me the opportunity to work on my dissertation as part of the P09 beamline staff. It has been a great privilege to learn the ins and outs of resonant elastic x-ray scattering at such an advanced and modern beamline as P09. Jörg also deserves thanks for all the valuable time he has freely donated to answering questions, participating in beamtime, and otherwise helping me along the road to a finished dissertation.

P09 would not be the great beamline it is without its people. Heartfelt thanks go to my co-workers at P09; Dr. Dinesh K. Shukla, Dr. Sonia Francoual, Dr. Helen C. Walker, David Reuther, and Dr. Claudio Mazzoli; for useful discussions, beamtime participation and help with experiment preparation and data analysis.

I could not have obtained the results I have without help from my collaborators. Many thanks go to Prof. Dr. Gerrit van der Laan for illuminating discussions and for performing the multiplet calculations presented in chapter 7. Dr. Enrico Schierle and Dr. Eugen Weschke have been invaluable for their help in performing the soft x-ray experiments, interpreting the results on magnetic Eu^{3+}, and creating a manuscript for publication. I cannot thank them enough. The experimental results on $GdMnO_3$ would not have come to be without the help and support from Dr. Ralf Feyerherm, Dr. Esther Dudzik and Dr. Zahirul Islam. I thank them all.

I thank Dr. Hoyoung Jang for interesting discussions. Thank you also to Dr. Uta Rütt, Olof Gutowski and Dr. Martin von Zimmermann for help with the high energy x-ray experiments at P07.

Also deserving of thanks are all the staff that have been working with me at Sector 6 in the PETRA III hall and provided help with experiments and a positive working environment, namely Dr. Oliver Seeck, Dr. Carsten Deiter, Kathrin Pflaum, Rainer Döring, Dr. André Beerlink, Julia Wernecke, Dr. Milena Lippmann, Dr. Karthick Perumal and Dr. Florian Bertram. This extends to all the other co-workers at DESY I have come to know

throughout my time here. Thank you all. A special thanks goes to Prof. Dr. Ralf Röhlsberger for supporting my work throughout. No less thanks go to the head of PETRA III during my time here, Dr. Hermann Franz, and the head of the Photon Science Division, Dr. Edgar Weckert, for giving me the opportunity to work at DESY and for providing a seamless working environment.

Music has always been important to me. I have been lucky to be a member of the excellent chamber choir Ensemble Vocal since shortly after arriving in Hamburg. We have had many memorable musical experiences together in that time, providing a necessary contrast to the daily life of science. I give thanks to all the other singers for this. Likewise, it has been a most enjoyable experience to play regularly with my fellow band members in Skyliner Big Band. Thank you.

Thank you also to my parents and brothers for all they have done for me for over 30 years now, and for instilling in me a love for science.

Lastly, I thank my beloved Rieke Marxen for her love and support through it all. You and our son Magnus Anton Skaugen have given me inspiration like no one else. This is for you both.

Eidesstattliche Versicherung

Declaration on oath

Hiermit erkläre ich an Eides statt, dass ich die vorliegende Dissertationsschrift selbst verfasst und keine anderen als die angegebenen Quellen und Hilfsmittel benutzt habe.
I hereby declare, on oath, that I have written the present dissertation by my own and have not used other than the acknowledged resources and aids.

Hamburg, den *city and date* Unterschrift *signature*